DETERMINING HEATING RATES IN RECONNECTION FORMED FLARE LOOPS

by

Wenjuan Liu

A dissertation submitted in partial fulfillment
of the requirements for the degree

of

Doctor of Philosophy

in

Physics

MONTANA STATE UNIVERSITY
Bozeman, Montana

July, 2014

UMI 3637100

Published by ProQuest LLC (2014). Copyright in the Dissertation held by the Author.

ProQuest LLC.
789 East Eisenhower Parkway
P.O. Box 1346
Ann Arbor, MI 48106 - 1346

DEDICATION

In memory of my friend, Peijun Li 1982–2007

ACKNOWLEDGEMENTS

I would like to wholeheartedly thank my advisor, Dr. Jiong Qiu, whose knowledge, scientific rigor and enthusiasm are a constant inspiration; I greatly appreciate for her patience and dedication in mentoring me these years, and helping improve my writing and presentation skills. I sincerely thank my collaborators Dr. D. Longcope and Dr. A. Caspi for their valuable insights and helpful conversations, and my committee members Dr. D. Longcope, Dr. C. Kankelborg, Dr. D. McKenzie, and Dr. J. Neumeier for their helpful advice; I would like to thank the MSU Solar Physics group for the cheerful and warm atmosphere; the MSU Physics Department and its dedicated staff, especially Margaret and Sarah, for making the studies and researches easier without worrying about paperwork, and for making Bozeman home; and my classmates, especially Kathryn and Gary, for helping me through my first year abroad; my beloved friends, especially Becky, Kiona and Kate, for their words of encouragement and helping improve my English speaking. I would also like to thank the NJU Solar Physics faculty and the NJU Astronomy Department for their advice, training and support, and for showing me the beauty of Solar Physics.

Finally, I would like to express much appreciation to my family who always encourages and supports me. I am forever thankful for my husband, Xudong, who followed me to the United States and has been supporting and helping me in every possible way.

TABLE OF CONTENTS

TABLE OF CONTENTS – CONTINUED

LIST OF TABLES

Table Page

LIST OF FIGURES

LIST OF FIGURES – CONTINUED

ABSTRACT

In this work, we determine heating rates in reconnection formed flare loops with analysis of observations and models. We utilize the spatially resolved ultraviolet (UV) light curves and the thick-target hard X-ray (HXR) emission to construct heating rates of a few thousand flare loops anchored at the UV footpoints. These loops are formed and heated by magnetic reconnection taking place successively. These heating rates are then used as an energy input in the zero-dimensional Enthalpy-Based Thermal Evolution of Loops (EBTEL) model to calculate the evolution of plasmas in these loops and compute synthetic spectra and light curves in Soft X-ray (SXR) and extreme ultraviolet (EUV), which compare favorably with those observed by the *Geostationary Operational Environmental Satellite (GOES)*, *Reuven Ramaty High Energy Solar Spectroscopic Imager (RHESSI)*, and *Solar Dynamics Observatory (SDO)*. With a steady-state assumption, we also compute the transition-region differential emission measure (DEM) at the base of each flare loop during its decay phase, and compare the predicted UV and EUV emissions at the footpoints with AIA observations. This study presents a method to constrain heating of reconnection-formed flare loops using all available observations, and provides insight into the physics of energy release and plasma heating during the flare. Furthermore, using *RHESSI* HXR observations, we could also infer the fraction of non-thermal beam heating in the total heating rate of flare loops. For an M8.0 flare on 2005 May 13, the lower limit of the total energy used to heat the flare loops is estimated to be 1.22×10^{31} ergs, out of which, less than 20% is carried by beam-driven upflows during the impulsive phase. The method is also applied to analyzing an eruptive M3.7 flare on 2011 March 7 and a compact C3.9 flare on 2012 June 17. Both flares are observed in EUV wavelengths by the Atmospheric Imaging Assembly (AIA) and Extreme Ultraviolet Variability Experiment (EVE) onboard the *SDO*, which allow us to investigate the flare evolution from the heating to cooling phase. The results show that the model-computed synthetic EUV emissions agree very well with those observed in AIA bands or EVE lines, indicating that the method successfully captures heating events and appropriately describes mean properties of flare plasma shortly after the heating phase.

1. INTRODUCTION

1.1 Overview of Solar Flares

A solar flare is a localized, sudden, rapid brightening observed over the Sun's surface or the solar limb. The first observation of a solar flare was reported by Carrington (1859) and Hodgson (1859) independently. They both noticed the appearance of a short-lived, brilliant brightening in the white light when observing a group of sunspots on September 1, 1859. The Carrington flare was discovered to be followed by a strong geomagnetic storm which occurred within 24 hours (Stewart, 1861). With the help of modern telescopes, radiation signatures of solar flares are observed across the entire electromagnetic spectrum at all wavelengths: radio, microwave, infrared, optical, ultraviolet (UV), extreme ultraviolet (EUV), X-rays and gamma rays.

From the time history of the total radiation, the so called light curves, from the sun or from the active region where the flare occurs, a flare is detected as an impulsive rise on the time scale of a few minutes to tens of minutes followed by a gradual decay. According to the peak intensity (in units of W cm^{-2}) at 1 AU of soft X-ray (SXR) radiation in the wavelength range of 1–8 Å measured by the X-ray Sensor (XRS) on the *Geostationary Operational Environmental Satellite* (*GOES*), a flare is classified to be in one of the five classes: A, B, C, M, X (see Table 1.1 for details of flare classification). The Carrington flare is estimated to be an X45 (± 5) class flare by comparing records of magnetic crochet caused by the Carrington flare with

Table 1.1: Flare classification based on peak intensity in 1–8 Å observed by *GOES*.

GOES class	Peak flux of flare (W cm^{-2})
A	$F < 10^{-7}$
B	$10^{-7} \leq F < 10^{-6}$
C	$10^{-6} \leq F < 10^{-5}$
M	$10^{-5} \leq F < 10^{-4}$
X	$F \geq 10^{-4}$

that produced by the Halloween flare on November 4, 2003 (Boteler, 2006; Cliver & Dietrich, 2013).

The morphology of solar flares is different when flares are observed in different ranges of wavelengths, depending on where the emission comes from and the mechanisms of the emission. Images of flares at various wavelengths are shown in Figure 1.1. As seen in Figure 1.1, SXR and EUV emissions are usually generated in the corona and appear to come from fine structure called flare loops. It is commonly accepted that coronal loops are clusters of magnetic field lines with plasmas frozen in. The heated plasmas inside flare loops emit in SXR and EUV wavelengths. Emissions in UV, hard X-ray (HXR), and optical bands are considered to be emitted by the heated plasmas in the chromosphere and transition region, which appear to outline the feet of coronal loops or arcades. Table 1.2 summarizes morphology of flares observed in different wavelengths by space or ground-based telescopes and their emission mechanisms. (See reviews by Benz (2008) and Fletcher et al. (2011) for more details on flare observations.)

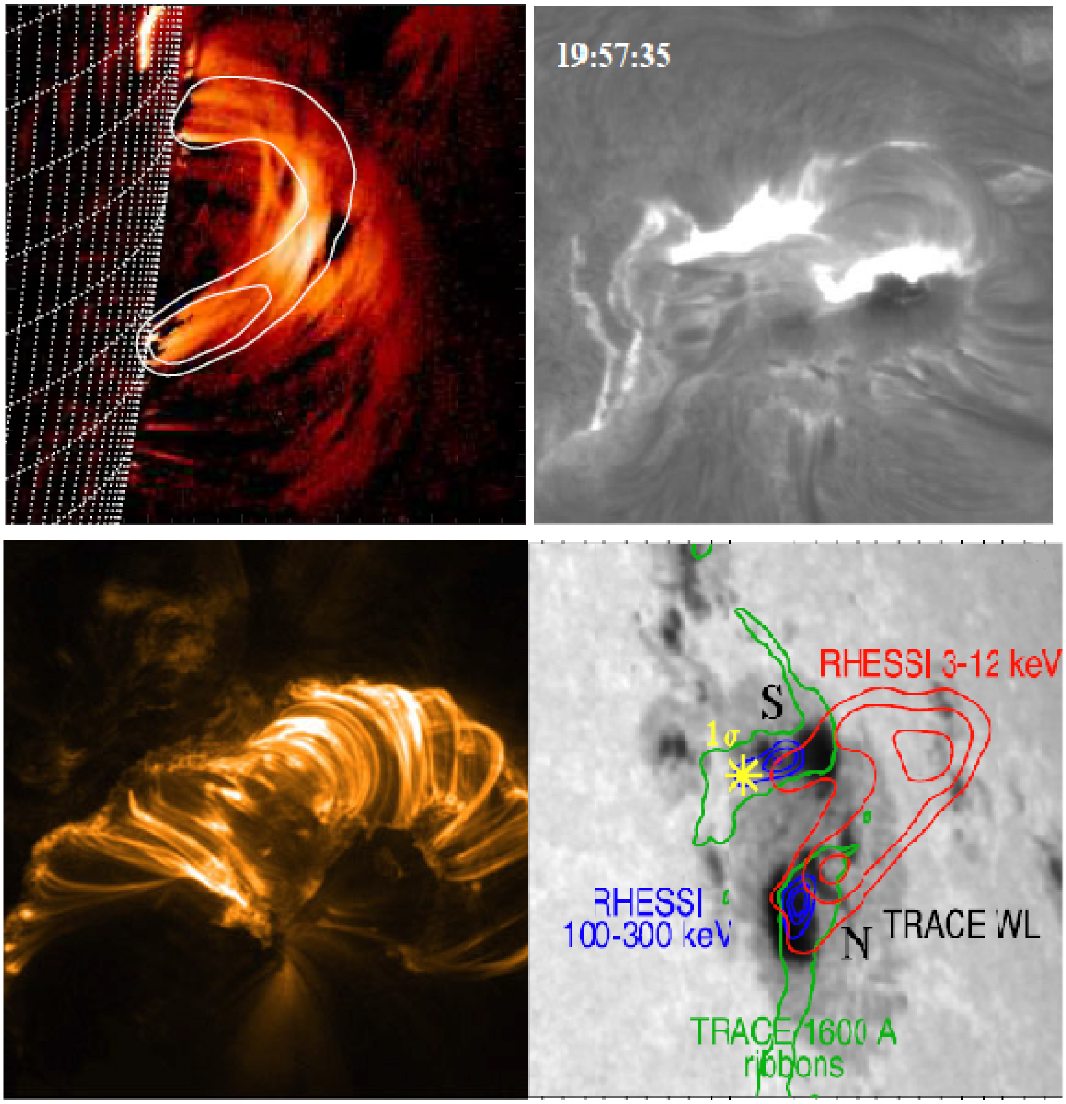

Figure 1.1: Images of flare emission at various energy bands: [top left] contours of Nobeyama 34 GHz emissions (white) overlaid on differential *TRACE* 195 Å images (color) by subtracting of the earlier images from the later one for 2002 August 24 flare (from Reznikova et al. (2009)); [top right] H_α images observed from BBSO on 1998 November 5 (from Wang et al. (2000)); [bottom left] *TRACE* 171 Å image of flare on 2010 April 01 (from Fletcher et al. (2011)); [bottom right] contours of *RHESSI* HXR (blue), SXR (red), gamma ray images (yellow star), and contours of ribbon in *TRACE* 1600 Å band overlaying the *TRACE* white light image for 2005 January 20 flare (from Grechnev et al. (2008)).

Table 1.2: Observation signatures of solar flares at various wavelengths.

Wavelength	Morphology	Location	Mechanism
Radio	footpoints, loops	corona, lower atmosphere	depends on the wavelength observed and local conditions in the flaring source, e.g., thermal free-free emission and absorption, incoherent gyrosynchrotron emission
optical continuum and lines	ribbons, kernels	photosphere, chromosphere	bound-free and bound-bound emission and absorption
UV continuum and lines	ribbons, kernels	transition region and upper chromosphere	thermal bound-free and bound-bound emission
EUV lines	loops	corona	thermal bound-bound emission
SXR	loops, looptop source	corona	thermal bound-bound and bound-free emission
HXR	footpoints	lower atmosphere	thick-target bremsstrahlung of nonthermal electrons
	looptop source	corona	thin-target bremsstrahlung of thermal electrons
Gamma ray	footpoints	lower atmosphere	collision of high energy protons with ions in ambient plasma

Parker (1957) and Sweet (1958) proposed that flares are generated by magnetic reconnection in the corona and powered by magnetic energy released from the reconnection. Since then, a lot of flare models based on magnetic reconnection have been put forward to explain the observed signatures of flares. One of the most accepted flare models is the standard two-dimensional (2D) flare model first proposed by Carmichael (1964); Sturrock (1966); Hirayama (1974); Kopp & Pneuman (1976). Therefore the standard flare model is also named as the CSHKP model to memorize the scientists who contribute to the initial model.

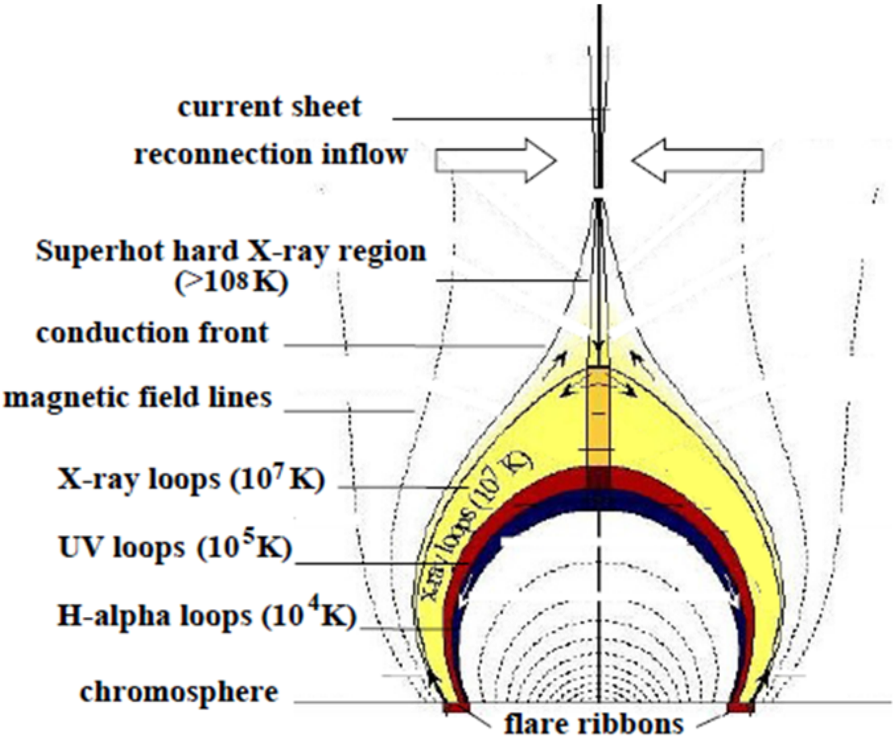

(adapted from Forbes & Acton, 1996)

Figure 1.2: A schematic drawing of the standard flare scenario, adapting from Forbes & Acton (1996).

A sketch of the standard flare scenario is shown in Figure 1.2. As seen in the figure, magnetic reconnection occurs in the corona usually at a null point (where the magnetic field vanishes) or quasi-separatrix layer (where field lines display strong gradients of magnetic connectivity). Through reconnection, the magnetic field changes configuration to a lower energy state, and magnetic free energy is effectively converted into plasma kinetic and thermal energy. At the same time, particles are accelerated by a strong electric field around a current sheet generated in reconnection (e.g., Holman, 1985; Benka & Holman, 1994), by shocks or first-order Fermi acceleration (e.g., Tsuneta & Naito, 1998; Nishizuka & Shibata, 2013), or by turbulence or plasma waves (stochastic acceleration) (e.g., Hamilton & Petrosian, 1992; Miller et al., 1996). (Please refer to the review papers by Aschwanden (2002) and Zharkova et al. (2011) and references therein for details of electron acceleration processes in solar flares.) The energy released from reconnection is then transported along reconnection-formed flare loops to the lower atmosphere (the chromosphere and transition region), by conductive flux or non-thermal particles, where the feet of flare loops are observed in optical and UV wavelengths by bound-bound and bound-free emissions and absorptions, or in HXR by thick target bremsstrahlung of nonthermal electrons. As the chromosphere is impulsively heated, hot chromospheric plasmas are pushed upward and fill in the flare loops by an excess in local pressure to the ambient chromospheric pressure. This process, known as chromospheric evaporation, is observed as blueshift in the profile of spectral lines formed in the transition region and chromosphere (e.g., Doschek et al., 1980; Feldman et al., 1980; Doschek et al., 2013). (See paper by Antonucci (1989) for a summary on spectral diagnosis of solar flares.) Observable signatures in various wavelengths in the impulsive phase of a flare are studied in detail by Dennis & Schwartz (1989). Figure 1.3 shows signatures of a simple flare with one loop, together with physical processes in the impulsive phase and origins of different emissions in the solar atmosphere.

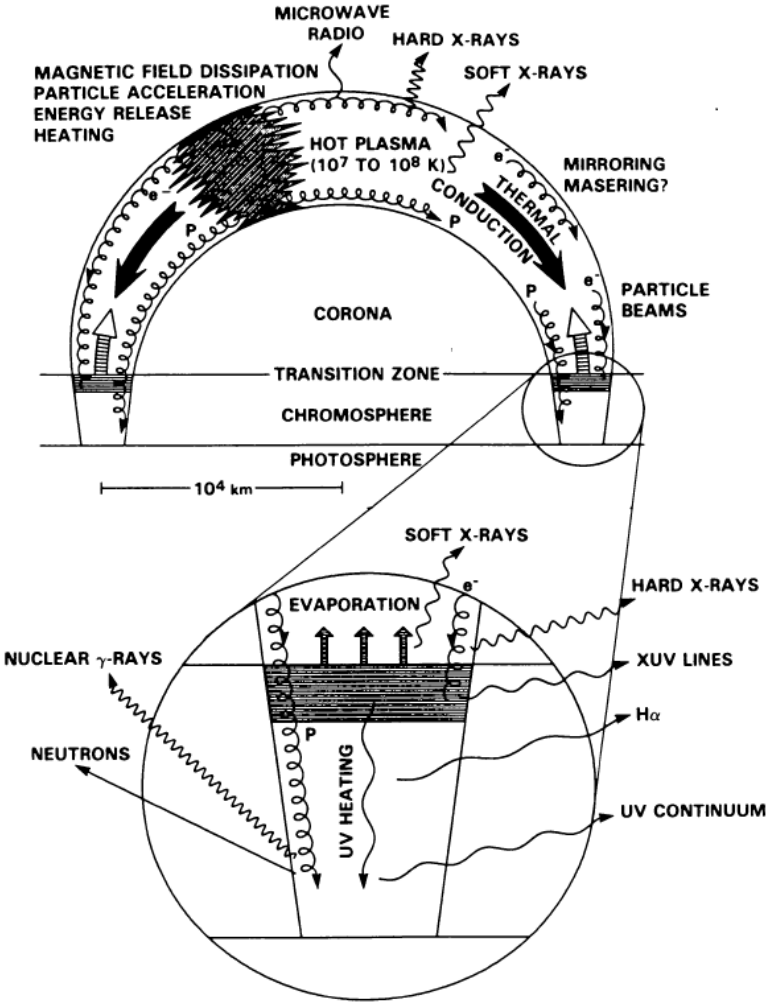

Figure 1.3: Schematic diagram of a simple flare with one loop showing some of the physical processes involved in flare model and origins of different emissions in the solar atmosphere (from Dennis & Schwartz (1989)).

During the decay phase of a flare, the evolution of a flare loop is dominated by cooling of hot plasmas filled in flare loops by chromospheric evaporation when there is no further energy deposited into the loop. The flare loops are first observed in SXRs via thermal bremsstrahlung at temperatures of up to a few tens of million Kelvin (MK). When they cool down to a few MK by radiation, as well as downward conduction, they begin to be visible in EUV channels. To study the effect of radiation and conduction on the cooling of flare plasma in the corona and chromosphere, theoretical models and numerical simulations are examined and performed (e.g., Wu et al., 1981; Antiochos, 1980; Doschek et al., 1982; Cargill et al., 1995; Reeves & Warren, 2002).

Numerical simulations are useful tools to test the models and help understand the nature of a flare. Magnetohydrodynamics (MHD) simulations are widely used to understand the process of energy build-up and onset of flares, and to model the energy release process. (See reviews by Priest & Forbes (2002) and Shibata & Magara (2011) for details of MHD processes in solar flares.) On the other hand, the response of the solar atmosphere to impulsive heating during flares and evolution of flare loops is studied by one-dimensional (1D) hydrodynamic simulations mostly with the assumption that plasmas are frozen in bundles of magnetic flux concentration (flare loops), which do not change their shape or magnetic property during the hydrodynamic evolution of loop plasmas (e.g., Nagai, 1980; Somov et al., 1981; Peres et al., 1982; Hawley & Fisher, 1994; Abbett & Hawley, 1999; Allred et al., 2005). The 1D assumption is typically justified on the a posteriori basis that the magnetic pressure of the surrounding field is greater than the gas pressure in the loop (Nagai & Emslie, 1984). With plasma properties calculated from hydrodynamic models, radiation from these flaring plasmas can be computed and compared with observable signatures of solar flares. Efforts have also been made to study evolution of loops in 2D. For example, in the recent work of Guarrasi et al. (2014), a 2D MHD model was applied to study the response of an active region loop with expansion of cross-section area through the transition region to heating at the center of the loop. For a flare loop with strong magnetic field and plasma frozen to the magnetic field, the change of magnetic field configuration during hydrodynamic evolution and the conductive flux across the field may be neglected (Oster & Sofia, 1966), therefore, 1D hydrodynamic models are widely used to study evolution of flare loops. The hydrodynamic loop model and its application to flare loops are reviewed in detail in the next section.

1.2 Overview of Hydrodynamic Loop Models

In 1D hydrodynamic loop models, the behavior of plasma in the loop is assumed to be governed by 1D hydrodynamic equations along the loop. The basic equations include the equations of mass, momentum and energy conservation, and equations describing the conductive flux and radiative energy losses of the loop in the corona and through the lower atmosphere.

The mass equation, which describes the transport of mass along the loop, is written as follows,

$$\frac{\partial \rho}{\partial t} + \frac{\partial (\rho v)}{\partial s} = 0, \tag{1.1}$$

where ρ is the total mass density, v is the fluid velocity, and s is the coordinate along the loop.

The momentum equation, which describes the bulk motion of the fluid governed by the net force along the loop due to the gas pressure gradient, gravity and viscosity, is presented by

$$\rho \frac{dv}{dt} = -\frac{\partial P}{\partial s} + \rho g + \frac{\partial}{\partial s}\left(\mu \frac{\partial v}{\partial s}\right), \tag{1.2}$$

where P is the total gas pressure from electrons and ions, g is the component of gravitational acceleration along the loop, μ is the viscosity coefficient of the plasma.

The energy equation depends on the treatment of the plasma as a one-fluid gas with the same bulk velocity and temperature for electrons, protons and hydrogen atoms (e.g., Nagai, 1980; Nagai & Emslie, 1984; Emslie & Nagai, 1985), or two-fluid with different temperatures for electrons and ions but the same speed of bulk motion (e.g., Somov et al., 1981, 1982; Cheng et al., 1983). However, the basic physical processes that are taken into account in the energy equation are all the same, which include the effects of conductive flux, radiative loss, viscous dissipation, and heating from a flare. For example, in the model of Nagai (1980), the energy equation is expressed as

$$\frac{de}{dt} + w\frac{\partial v}{\partial s} = \frac{\partial}{\partial s}\left(\kappa \frac{\partial T}{\partial s}\right) - R + \mu \left(\frac{\partial v}{\partial s}\right)^2 + Q_q(s) + H(t, s) \tag{1.3}$$

where e is the internal energy per unit volume, w is the enthalpy per unit volume, κ is the thermal conductivity coefficient, R is the radiative loss, $Q_q(s)$ is the quiet sun heating term to maintain pre-flare equilibrium, $H(t, x)$ is the input flare heating rate. Once the spatial and temporal profile of heating rate is defined, the hydrodynamic evolution of plasma inside a flare loop will be calculated by numerically solving these 1D hydrodynamic equations.

To save computation time, Klimchuk et al. (2008) developed a zero-dimensional (0D) model named the Enthalpy-Based Thermal Evolution of Loops (EBTEL) which could be used to efficiently calculate the coronal temperature, density and pressure averaged along the loop by solving the integral equations of momentum and energy conservation and using the ideal gas law. It has been shown that the mean properties of plasma from the EBTEL model reasonably agree with mean values from simulations using a 1D hydrodynamic code (see Klimchuk et al., 2008, for details of the EBTEL model).

There is not a general form for the radiative loss rate R in the entire solar atmosphere. In the optically thin corona with a high temperature and low density, the radiative cooling is dominated by collisional excitation rather than radiative excitation (Cox & Tucker, 1969; Tucker & Koren, 1971; Raymond et al., 1976) and can be written empirically as a function of electron density and temperature. In the optically thick chromosphere with a high density, the radiative loss is more sophisticated and must be calculated by solving non-local thermodynamic equilibrium (non-LTE) radiative transfer equations.

In practice, most hydrodynamic simulations are simplified in two different ways. Some use empirical functions for optically thin radiation by plasmas from the corona and transition region and ignore radiation at temperatures below 9500 K in the chromosphere or treat the chromosphere as an energy sink and mass source to study evolution of flare heated loops in the corona (e.g., Nagai, 1980; Somov et al., 1981; Peres et al., 1982; Cheng et al., 1983; Nagai & Emslie, 1984), while others use full non-LTE formulation of radiation transfer to investigate the spectroscopic signatures of flare heated chromosphere (e.g., Ricchiazzi & Canfield, 1983; Fisher et al., 1985a; Hawley & Fisher, 1994; Abbett & Hawley, 1999; Allred et al., 2005). The radiative hydrodynamic simulations have succeeded in reproducing optically thick emissions in solar flares; however, the corona in these simulations could only reach a few MK, which is much less than observed temperatures of tens of MK. On the other hand, the hydrodynamic models with optically thin emissions, though unable to address emissions from the chromosphere, work better at reproducing high coronal temperatures and densities, and enhancements of UV emissions from the transition region.

The flare heating rate H is a crucial input in the energy equation when investigating solar atmospheric response during a flare and formation of the radiation signature of a flare in various wavelengths. The form of flare heating rates is an expression describing how much energy released from reconnection is used to heat the flare, how long heating lasts, and in which form the energy is deposited into a loop. We still know very little about the details of the flare heating rate. In many hydrodynamic simulations, an arbitrary assumed time profile of the heating rate, mostly a triangular function, has been used (e.g., Nagai, 1980; Somov et al., 1981; Cheng et al., 1983; Sterling et al., 1993). The spatial distribution of the heating rate is believed to be related to the heating mechanism. In many simulations when assuming energy is transported to the lower atmosphere only by conductive flux, an unspecified ad hoc heating with a spatial Gaussian function centered on a specified location is used (e.g., Nagai, 1980; Somov et al., 1982; Cheng et al., 1983; Mariska, 1987; Sterling et al., 1993).

In some other studies, the source of energy and/or mechanism of heating is specified. For example, when studying the effect of non-thermal beams, energy is carried by non-thermal particles and the loop is heated by Coulomb collisions of electrons with ambient plasmas, either in the corona (thin target) or at the lower atmosphere (thick target), and an analytic expression of electron energy derived by Emslie (1978) or Brown (1973) is widely accepted (e.g., Somov et al., 1981; Nagai & Emslie, 1984; Mariska et al., 1989; Emslie et al., 1992; Winter et al., 2011; Reeves et al., 2012). Test particle simulations were also used by Kašparová et al. (2009) to calculate the flare heating in the chromosphere due to Coulomb collisions of the hydrogen atoms with an electron beam that has a power-law spectrum. Reeves et al. (2007) and Reeves & Moats (2010) used Poynting flux derived from numerical solutions of the loss-of-equilibrium flare model (Lin & Forbes, 2000; Lin, 2004) as the energy input in the loop heating model, and could relate the resultant plasma radiation time profile with the kinematic evolution of the flux rope ejection. Longcope et al. (2010) modeled and analyzed a flare observed by the *Transition Region and Coronal Explorer* (*TRACE*; Handy et al., 1999), using the reconnection-released energy calculated from a patchy reconnection model as the heating rate. How the looptop plasma is heated by slow magnetosonic shocks in patchy reconnection was studied in detail by Longcope & Guidoni (2011).

Another critical piece of knowledge about heating rates is based on the fact that during a flare, closed magnetic field lines (loops) are continually formed by reconnection. In the 2D flare model newly formed loops pile on top of earlier formed loops and therefore these loops are heated subsequently. The sequentially formed flare loops were revealed by high resolution EUV and UV images obtained by *TRACE* which show that the post-flare arcade and ribbon constitutes fine structure with characteristic size scale of $1''$ or less (e.g., Aschwanden & Alexander, 2001; Fletcher et al., 2004).

The observed signatures of flares also exhibit changes along the third direction. Qiu et al. (2010) found that the HXR sources and UV brightenings exhibit an organized parallel motion along the magnetic polarity inversion line (PIL) before the perpendicular expansion of UV ribbons. The apparent parallel motions of footpoints are also observed in other solar flares (e.g., Cheng et al., 2012; Inglis & Gilbert, 2013). The observed apparent motion of footpoints provides evidence that flare loops are formed and heated sequentially.

With the approximation that flare plasmas are confined along magnetic field lines, hydrodynamic evolution of these discrete flare loops should be independent of one another and should respond only to the energy release in individual loops. Based on this idea, Hori et al. (1997) first developed the multi-thread loop model with a few threads heated progressively from the innermost thread to the outermost and calculated their evolution separately with a 1D hydrodynamic code. The results of the multi-1D model successfully explain several flare features observed by the Soft X-Ray Telescope (SXT) onboard *Yohkoh*, e.g., the decrease in brightness of footpoints during the impulsive phase, the apparent outward expansion and upward motion of the loop, and the nearly constant width observed along the loop. The multi-1D model was further used to study X-ray and EUV observations of flares (e.g., Hori et al., 1998; Reeves & Warren, 2002; Warren & Doschek, 2005; Warren, 2006; Reeves et al., 2007; Reeves & Moats, 2010). To constrain the energy input used in multi-1D hydrodynamic simulations, Warren & Doschek (2005) and Warren (2006) empirically derived the heating rate in each new thread as the amount of energy required to minimize the difference between the SXR flux observed by *GOES* and the calculated SXR flux emitted by earlier heated threads. Their model could reproduce the Ca XIX and S XV line profiles observed with the Bragg Crystal Spectrometer (BCS) onboard *Yohkoh* during the earliest stages of a flare as well as temporal evolution of high temperature thermal flaring plasma for the Masuda flare on 1992 January 13 observed by *GOES* and *Yohkoh*. In their model, the time profile of all heating events is assumed to be the same triangular function with a fixed duration (60 s in Warren & Doschek 2005, and 400 s in Warren 2006) with magnitude and timing of heating events during the flare adjusted to match the observed SXR flux.

The reproduction of observed signatures of solar flares by these multi-1D hydrodynamic simulations marks successful application of the idea that multiple flare loops are formed and heated independently and successively, leading to enhanced flare emission even during the decay phase. However, in these studies, the number of loops is not directly inferred from observations and the heating rates in individual loops are only constrained *post facto* from synthetic coronal emissions. Furthermore, loops are assumed to be formed and heated consecutively with a constant rate in previous multi-1D simulations (for example, new loops are created every 20 s in Reeves et al. 2007 and Reeves & Moats 2010, every 30 s in Warren 2006), which is not consistent with observed apparent movement of footpoints with different velocities at different phases of flares. To determine the formation and heating of flare loops with more constraints from observations, in this thesis, we use the observation of footpoint emission at 1600 Å to identify loops anchored at these footpoints. We also use the UV emission light curves from the footpoints to infer heating rates in individual loops, i.e., when each loop is heated, how long the heating lasts, and how much energy is put into each loop. With these heating rates, we use the 0D EBTEL model to compute the evolution of plasmas in thousands of flaring loops and calculate flare emissions in SXR, EUV and UV.

1.3 Aim and Outline of the Thesis

The goal of this thesis is to determine heating rates in flare loops continuously formed by magnetic reconnection in the corona by using constraints from observations at the footpoints where these loops anchor. In the thesis, we also investigate the effect of non-thermal beams in carrying energy flux to the chromosphere and the UV emissions (mostly in C IV line) from the transition region during the decay phase. With this approach, we can connect heating rates in flare loops with the rates of magnetic reconnection that formed these loops and released energy to heat them.

In order to determine the time profile of the heating rates in individual flare loops from observations, Qiu et al. (2012) have proposed that the impulsive rise of UV emission at the feet of these loops could be used to infer the heating rate. They use the impulsive rise of spatially resolved UV light curves to indicate, and therefore constrain when, for how long, and by how much a flare loop anchored at the UV foot is heated. With this method, Qiu et al. (2012) constructed the heating rates in 1600 flare loops of constant cross-sectional area of $1''$ by $1''$ anchored at impulsively brightened UV pixels for a C3.2 flare observed by the Atmospheric Imaging Assembly (AIA; Lemen et al., 2012) onboard the *Solar Dynamics Observatory* (*SDO*; Pesnell et al., 2012). Applying these heating rates as flare energy inputs to the EBTEL model they computed plasma evolution in these 1600 flare loops and the synthetic coronal radiation in SXR and EUV passbands. The comparison of synthetic radiation with observations are then used to adjust a few free parameters used in constructing the heating rate. This is an efficient and successful method to study the heating in a flare with thousands of loops formed successively by magnetic reconnection of coronal magnetic field using all available observations. In the thesis work, we improved the method of Qiu et al. (2012) to study flares with significant thick-target non-thermal HXR signatures, and also to analyze thermal bremsstrahlung SXR spectrum observed by *RHESSI* and EUV spectral lines by Extreme Ultraviolet Variability Experiment (EVE; Woods et al., 2012). The method is applied to three flares of different morphologies and spectral signatures; each of them is modeled as consisting of thousands of flare loops.

In Chapter Two, we studied an M8.0 flare on 2005 May 13 observed by *RHESSI*, *GOES* and *TRACE* satellites. The M8.0 flare was observed with significant thick-target HXR emission in the impulsive phase, which indicate that non-thermal beams play an important role in transporting energy and momentum to the lower atmosphere in the flare. Therefore, both UV and HXR emissions are used to infer the thermal heating and energy carried by non-thermal beams. In this chapter, we also studied the effect of beam-driven flux on evolution of plasmas in flare loop using the EBTEL model with the same impulsive heating rate and varying partition of the input energy carried by non-thermal beam-driven flux. For the M8.0 flare, we compute the synthetic light curves and spectra in SXR, using the plasma properties in all the flaring loops calculated from the EBTEL model with the inferred heating rates, and compare with that observed by*GOES* and *RHESSI*. For most of the impulsive phase, the synthetic light curves and spectra agree very well with the observed ones. We also compute the C IV emission, which is believed to dominate broadband UV emission at 1600 Å during the cooling phase of each flare loop by using the transition region differential emission measure (DEM) calculated from the pressure gauge assumption (Fisher, 1987; Hawley & Fisher, 1992) and the CHIANTI atomic data (Dere et al., 1997, 2009). Comparison between the synthetic and observed C IV light curves during the decay phase at the footpoints of flare loops shows that calculated decay time scale is the same as observed. The material in this chapter has been published in the Astrophysical Journal 770, 111, 2013 June.

In Chapter Three, an M1.9 flare observed by *GOES* and *SDO* is studied. With high-cadence high-resolution EUV images acquired by AIA and spectroscopic observations by EVE on *SDO*, we are able to study plasmas in flare loops from 2–10 MK and examine contributions of EUV emissions by warm plasmas in the loop or cooler plasmas at the footpoints. In this chapter, we study the M1.9 flare using observations in a few AIA bandpasses (AIA 131, 94, 335, and 211 band) and EVE in several spectral lines (Fe XXI, Fe XVIII, Fe XVI, Fe XIV). Our analysis shows that these four iron lines contribute 60%, 100%, 70%, and 30% to the total emission in these AIA channels, respectively. Study of the M1.9 flare also shows that the synthetic light curves taking into account emissions by both coronal plasmas in flare loops and transition region plasmas at the footpoints are in reasonable agreement with broadband AIA observations in the four EUV channels as well as the UV 1600 Å channel. The material in this chapter has been submitted to the Astrophysical Journal.

In the last Chapter, using the same method, we show the study of a compact C3.9 flare observed by *RHESSI*, AIA, and EVE which observe flare plasmas with temperature range from 2 MK to a few tens of MK. For the third flare, the synthetic light curves in the decay phase agree well with those observed by EVE and AIA. We also compare this flare with the two flares studied in the previous chapters. Based on our studies of these three flares using various instruments, summaries and conclusions, and direction for future research are also presented in this chapter.

2. DETERMINING HEATING RATES IN RECONNECTION FORMED FLARE LOOPS OF THE M8.0 FLARE ON 2005 MAY 13

Contribution of Authors and Co-Authors

Manuscript in Chapter 2

Author: Wen-Juan Liu

Contributions: All work except for the ones mentioned below.

Co-Author: Jiong Qiu

Contributions: Helped with study design. Provided scientific advice. Edited drafts of the manuscript.

Co-Author: Dana W. Longcope

Contributions: Provided code of EBTEL model. Provided feedback of analysis. Edited drafts of the manuscript.

Co-Author: Amir Caspi

Contributions: Prepared the observed dataset in Hard X-ray. Helped to calculate synthetic light curves and spectra in Hard X-ray. Edited drafts of the manuscript.

Manuscript Information Page

Wen-Juan Liu, Jiong Qiu, Dana W. Longcope, Amir Caspi
The Astrophysical Journal
Status of Manuscript:
___Prepared for submission to a peer-reviewed journal
___Officially submitted to a peer-reviewed journal
___Accepted by a peer-reviewed journal
_x_Published in a peer-reviewed journal

Published June, 2013, ApJ 770, 111

ABSTRACT

We analyze and model an M8.0 flare on 2005 May 13 observed by the *Transition Region and Coronal Explorer* (*TRACE*) and *Reuven Ramaty High Energy Solar Spectroscopic Imager* (*RHESSI*) to determine the energy release rate from magnetic reconnection that forms and heats numerous flare loops. The flare exhibits two ribbons in UV 1600 Å emission. Analysis shows that the UV light curve at each flaring pixel rises impulsively within a few minutes, and decays slowly with a timescale longer than 10 minutes. Since the lower atmosphere (the transition region and chromosphere) responds to energy deposit nearly instantaneously, the rapid UV brightening is thought to reflect the energy release process in the newly formed flare loop rooted at the foot point. In this chapter, we utilize the spatially resolved (down to 1″) UV light curves and the thick-target hard X-ray emission to construct heating functions of a few thousand flare loops anchored at the UV foot points, and compute plasma evolution in these loops using the Enthalpy-Based Thermal Evolution of Loops (EBTEL) model. The modeled coronal temperatures and densities of these flare loops are then used to calculate coronal radiation. The computed soft X-ray spectra and light curves compare favorably with those observed by *RHESSI* and by the *Geostationary Operational Environmental Satellite* (*GOES*) X-ray Sensor (XRS). The time-dependent transition region differential emission measure (DEM) for each loop during its decay phase is also computed with a simplified model and used to calculate the optically-thin C IV line emission, which dominates the UV 1600 Å bandpass during the flare. The computed C IV line emission decays at the same rate as observed. This study presents a method to constrain heating of reconnection-formed flare loops using all available observables independently, and provides insight into the physics of energy release and plasma heating during the flare. With this method, the lower limit of the total energy used to heat the flare loops in this event is estimated to be 1.22×10^{31} ergs, of which only 1.9×10^{30} ergs is carried by beam-driven upflows during the impulsive phase, suggesting that the coronal plasmas are predominantly heated *in situ*.

2.1 Introduction

Solar flares are generally believed to be a result of magnetic reconnection in the corona. After reconnection, the connectivity of the magnetic field changes and the field relaxes to a lower energy state. The energy released during reconnection is transported along reconnection-formed flare loops to the lower atmosphere, by conductive flux or non-thermal particles, giving rise to enhanced emissions in optical and ultraviolet (UV) wavelengths. As the chromosphere is impulsively heated, a pressure front is formed that pushes plasmas both upward (chromospheric evaporation) and downward (chromospheric condensation). The upflow fills flare loops, where energy is radiated away in soft X-rays (SXRs) via thermal bremsstrahlung at temperatures of up to a few tens of million Kelvin (MK). When these loops cool down to a few MK, they begin to be visible in extreme ultraviolet (EUV). (See the comprehensive review by Fletcher et al. 2011.)

In this qualitative picture, several fundamental questions remain unanswered in terms of the quantity of energy. First, we do not know how much energy is released by reconnection, and how much energy in total is radiated by flare plasmas (and carried away by coronal mass ejections, if any); in principle, the former should equal the latter. Second, we do not fully understand how, and by how much, flare plasmas are heated and particles are accelerated by reconnection-released energy, generating observed radiation signatures across the full spectral range.

A variety of hydrodynamic simulations have been performed to understand energy transport in flare loops and the atmospheric response to energy deposition at the feet of these loops in the transition region and chromosphere (e.g., Nagai, 1980; Somov et al., 1981; Peres et al., 1982; Cheng et al., 1983; Nagai & Emslie, 1984; Fisher et al., 1985a; Emslie & Nagai, 1985; Mariska et al., 1989; Hawley & Fisher, 1994; Abbett & Hawley, 1999; Allred et al., 2005). Since plasmas are frozen in magnetic loops, most of these simulations use one-dimensional (1D) models. Some of these hydrodynamic simulations concentrate on the lower atmosphere by using full non-LTE formulation of radiation transfer (i.e., Fisher et al., 1985a; Hawley & Fisher, 1994; Abbett & Hawley, 1999; Allred et al., 2005), while others focus on the upper atmosphere dominated by optically thin emissions and treat the lower atmosphere as boundary conditions (i.e., Nagai, 1980; Somov et al., 1981; Peres et al., 1982; Cheng et al., 1983; Nagai & Emslie, 1984). The radiative hydrodynamic simulations have succeeded in reproducing optically thick emissions in solar flares; however, the corona could only reach a few MK, which is much less than observed temperatures of tens of MK. On the other hand, the hydrodynamic models with optically thin emissions, though unable to address emissions from the chromosphere, work better at reproducing high coronal temperatures and densities, and enhancements of UV emissions from the transition region.

With high resolution EUV images obtained by the *Transition Region and Coronal Explorer* (*TRACE*; Handy et al., 1999), it is found that the flare arcade is composed of at least a few hundred flaring loops formed successively (e.g., Aschwanden & Alexander, 2001). It is further confirmed by Fletcher et al. (2004) that the flare UV ribbons are made of small kernels outlining the feet of flare loops. To simulate sequentially formed loops in solar flares, Hori et al. (1997) developed a “pseudo-two-dimensional” model with multiple 1D loops heated progressively from the innermost loop to the outermost. The multi-1D model was further used to reproduce X-ray and

EUV observations of flares (e.g., Hori et al., 1998; Reeves & Warren, 2002; Warren & Doschek, 2005; Warren, 2006; Reeves et al., 2007; Reeves & Moats, 2010).

The hydrodynamic evolution of plasma inside the flare loop appears to be governed by how the loop is heated. Specifically, we need to know when, for how long, by how much, and by what physical mechanism a flare loop is heated. Among existing models, many start with an unspecified *ad hoc* heating source in the corona, and the energy is transported through conductive flux (e.g., Somov et al., 1982; Nagai, 1980; Cheng et al., 1983; Mariska, 1987; Sterling et al., 1993). Some other models specify the source of the energy and/or mechanism of heating. For example, Somov et al. (1981), Nagai & Emslie (1984), Mariska et al. (1989), Emslie et al. (1992), and Reeves et al. (2012) assumed that energy is carried by non-thermal particles and the loop is heated by Coulomb collisions of electrons with ambient plasmas, either in the corona (thin target) or at the lower atmosphere (thick target), using an analytic expression of electron energy derived by Emslie (1978) or Brown (1973). Reeves et al. (2007) and Reeves & Moats (2010) used Poynting flux derived from numerical solutions of the loss-of-equilibrium flare model (Lin & Forbes, 2000; Lin, 2004) as the energy input in the loop heating model, and could relate the resultant plasma radiation time profile with the kinematic evolution of the flux rope ejection.

Effort has also been made to constrain the energy input with observations. Warren & Doschek (2005) and Warren (2006) derived the heating rate empirically by matching the loop heating model results with the SXR fluxes observed by the X-ray Sensor

(XRS) on the *Geostationary Operational Environmental Satellite* (*GOES*). In their model, the heating events are assumed to have a triangular time profile with a fixed duration (60 s in Warren & Doschek 2005, and 400 s in Warren 2006) and their magnitudes and distributions during the flare are adjusted to match the observed SXR flux. Longcope et al. (2010) modeled and analyzed a flare observed by *TRACE*, using as the heating rates the reconnection-released energy, which is calculated from a patchy reconnection model. The model takes the observed photospheric magnetic field as the boundary, and uses the observationally measured reconnection rate and time distribution of reconnection-formed flare loops counted in EUV images obtained by *TRACE*. The modeled coronal radiation compares favorably with SXR observations from *GOES* XRS and the *Reuven Ramaty High Energy Solar Spectroscopic Imager* (*RHESSI*; Lin et al., 2002).

Along this avenue, recently, Qiu et al. (2012) have proposed that the heating rates in individual flare loops could be directly inferred from the time profiles of UV emission at the feet of flare loops. The spatially resolved UV light curves exhibit an impulsive rise, which indicates, and therefore constrains, when, for how long, and by how much a flare loop is heated. Accordingly, Qiu et al. (2012) constructed from these light curves the heating rates of 1600 loops, *each* with cross-sectional area of $1''$ by $1''$, anchored at impulsively brightened UV pixels in a C3.2 flare observed by the Atmospheric Imaging Assembly (AIA; Lemen et al., 2012) onboard the *Solar Dynamics Observatory* (*SDO*; Pesnell et al., 2012). Applying these heating rates to a zero-dimensional loop heating model, the Enthalpy-Based Thermal Evolution of Loops (EBTEL; Klimchuk et al., 2008; Cargill et al., 2012a,b) model, they computed plasma evolution in these 1600 flare loops and the synthetic coronal radiation in SXR and EUV passbands, which are compared with observations by *GOES* and AIA to verify the empirically determined heating rates. This method uses all available observations to constrain the heating rates from the input (the impulsive UV emission from the foot points) to the output (the X-ray and EUV emission from the coronal loops). The flare studied in their paper is primarily a thermal flare with little hard X-ray (HXR) emission, and *ad hoc* volumetric heating rates are used in the model.

In this chapter, we will improve the method of Qiu et al. (2012) and apply the analysis to an M8.0 flare on 2005 May 13 observed by *TRACE*, *GOES*, and *RHESSI*. The flare exhibits significant thick-target non-thermal HXR emission observed by *RHESSI*, suggestive of strong direct heating of the lower atmosphere that would result in chromospheric evaporation that sends energy back to the corona. We also include in the loop heating model this energy flux of non-thermal origin, using observed UV and thick-target HXR emissions as constraints. As the output of the model, we calculate the time-dependent 3–20 keV SXR spectrum and compare this with the observations by *RHESSI*. Finally, whereas the impulsive rise of the UV foot-point emission is considered to directly relate to the energy release process, the observed gradual decay of the UV emission from the same foot-point is governed by evolution of the overlying coronal plasma in the loop, which therefore provides diagnostics of the loop cooling. In this chapter, we use a simplified model to compute the UV emission during the decay of flare loops to further compare with observations. These new steps help improve determination of the heating rates, and enhance our understanding of flare energy release, partition, and plasma heating and evolution. In the following text, we present in Section 2.2 observations of the flare, especially the UV and HXR observations, which will be used to construct the heating functions, and apply them to model coronal plasma evolution in Section 2.3. In Section 2.4, we compute time-dependent SXR and UV fluxes from the model output and compare them with observations. Conclusions and discussions are given in Section 2.5.

2.2 Observations and Analysis

2.2.1 Overview of Observations

In this chapter, we study a *GOES*-class M8.0 flare that occurred on 2005 May 13 in NOAA Active Region 10759 located at N12E05 at the time of the flare. Figure 2.1 summarizes observations of the flare in a few wavelengths. High cadence (3 s) UV images obtained by *TRACE*, given in the bottom panel, reveal that the M8.0 flare is a typical two ribbon flare. The flare UV ribbons expand away from the magnetic polarity inversion line for half an hour, indicating that magnetic reconnection continues to form new loops and release energy in them, as depicted by the standard flare model (the CSHKP model; Carmichael, 1964; Sturrock, 1966; Hirayama, 1974; Kopp & Pneuman, 1976). Significant X-ray emissions are observed in this flare by *RHESSI*.

Previous morphology studies of this same flare show that, during the impulsive phase, the sources of non-thermal HXR emissions of $\geq$25 keV are located within the UV flare ribbons (see Fig. 2 and Fig. 3 of Liu et al., 2007, for images of HXR kernels in 25–50 keV and 50–100 keV energy bands overlaid on the UV contours). These observations confirm that UV and HXR emissions are both produced by heating of the lower atmosphere (the transition region and chromosphere) by energetic particles precipitating at the feet of flare loops during the impulsive phase (see, e.g., Cheng et al., 1981, 1988; Warren & Warshall, 2001; Coyner & Alexander, 2009; Cheng et al., 2012).

The top panel in Figure 2.1 shows normalized and background-subtracted X-ray and UV light curves observed by *GOES*, *RHESSI*, and *TRACE*, respectively. The UV light curve is the total count rate (in units of DN s^{-1}) derived from the semi-calibrated UV images (see Qiu et al., 2010, Section 3.1 for calibration techniques), with pre-flare counts subtracted. It follows closely the $\geq$25 keV HXR light curve during the rise of the flare and the impulsive phase, but continues to rise after the HXR peak at 16:42 UT, and reaches maximum five minutes later. Also plotted is the time derivative of the *GOES* 1–8 Å SXR light curve, and it is seen that the UV light curve peaks at the same time (16:47 UT) as the time derivative of the SXR flux. The temporal correlation between HXR and SXR time derivative has been known as the Neupert effect (Neupert, 1968; Dennis & Zarro, 1993), with the basic idea that non-thermal electrons precipitate at the chromosphere, losing their energy

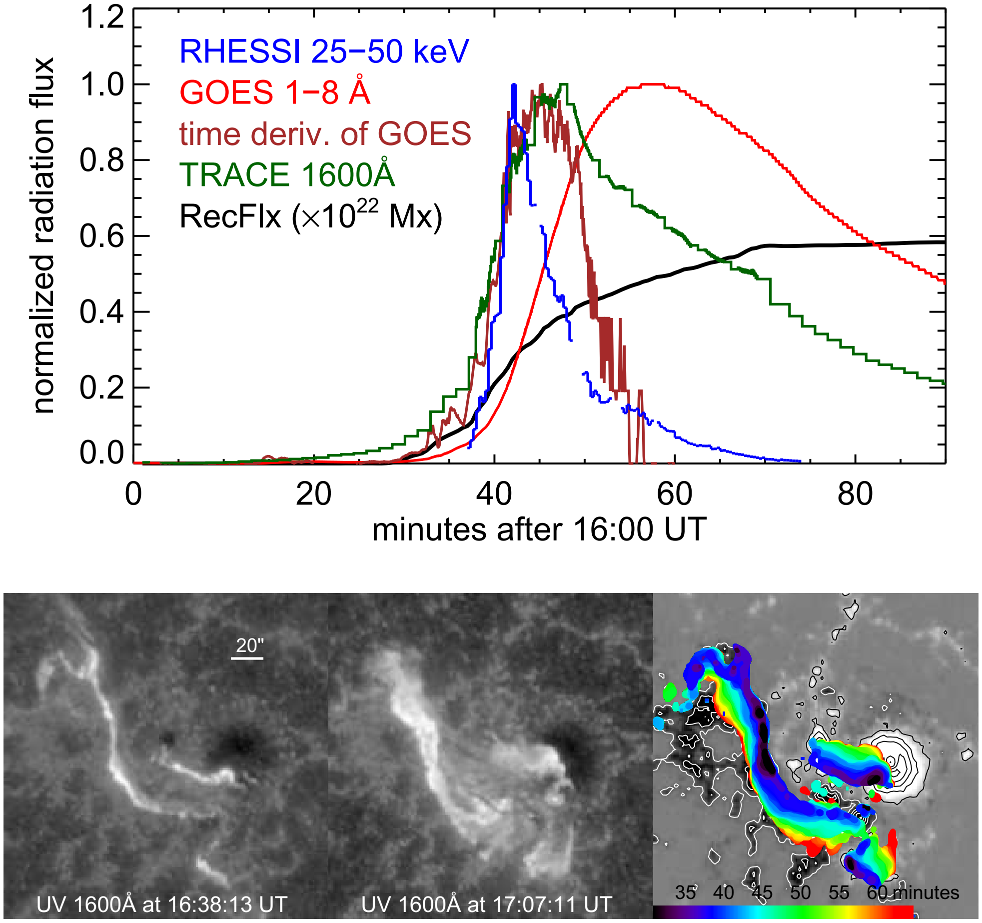

Figure 2.1: Light curves and images of the M8.0 flare observed on 2005 May 13. The upper panel shows background-subtracted and normalized light curves in HXRs (25–50 keV) observed by *RHESSI* detector 4 (blue), SXRs (1–8 Å) by *GOES* XRS (red), and UV (1600 Å band) by *TRACE* (dark green). Also plotted are the time derivatives of the 1–8 Å SXR flux (brown), and magnetic reconnection flux (black) measured by using UV 1600 Å observations and the longitudinal magnetogram from *SOHO*/MDI. The left and middle images in the lower panel are snapshots of UV images during the impulsive and decay phases of the flare observed by *TRACE*, while the lower right panel shows evolution of the UV brightening on top of the MDI longitudinal magnetogram taken at 16:03:02 UT with the color bar indicating the start times of UV brightening at different locations.

by Coulomb collision to give rise to HXR emission, and at the same time, driving chromospheric evaporation to fill flare loops that are subsequently observed in SXRs.

This flare, however, exhibits a similar Neupert effect between the SXR derivative and UV, instead of HXR, light curves. This is evidence of continuous energy deposition in the lower atmosphere, most likely by thermal conduction, after the impulsive phase when thick-target HXR emission is no longer significant.

The time sequence of UV images further shows that the continuous rise of the UV emission after the HXRs is produced by newly brightened UV ribbons (bottom panel in Figure 2.1). The spread of the flare UV ribbons across the longitudinal magnetic field (lower right panel) provides a measurement of magnetic reconnection flux (Qiu et al., 2002; Longcope et al., 2007), plotted in the top panel. The reconnection flux starts to grow at 16:30 UT at the beginning of both UV and X-ray light curves. The continuous increase of reconnection flux and dramatic decay of non-thermal emission after 16:50 UT (the post-impulsive phase) confirm that reconnection continues to form new loops and release energy in them, and the thermal process is dominant in this late phase of the flare. The post-impulsive reconnection flux amounts to 2×10^{21} Mx, about one third of the total reconnection flux measured for this flare.

Comparison of the UV and X-ray observations of the flare suggests that imaging UV observations provide information of energy release, which is then transported to the lower atmosphere by either non-thermal electrons or thermal conduction, in newly formed flare loops anchored at newly brightened UV ribbons. Based on this idea, we have analyzed spatially resolved UV light curves, using them to construct heating rates of flare loops in a C3.2 flare (Qiu et al., 2012). The analysis is applied to this flare, as well, in the following Sections.

2.2.2 Characteristics of UV Light Curves

Examples of the UV light curve in a flaring pixel ($1''$ by $1''$), shown in the top panel of Figure 2.2, typically exhibits a rapid rise, peaks within several minutes, and then decays slowly with a characteristic "cooling" time of more than 10 minutes. Such characteristics have been found in UV observations of other flares as well (Qiu et al., 2010; Cheng et al., 2012; Qiu et al., 2012). Since the lower atmosphere (the transition region and chromosphere) responds to energy deposition on very short timescales, the rise time of UV emission reflects the timescale of energy release in the flare loop anchored at this pixel. The gradual decay, on the other hand, is coupled with subsequent cooling processes in the overlying corona.

To characterize the rapid rise of the spatially resolved UV light curves, we fit the rise of the UV count rate light curve (in units of DN s^{-1}) to a half Gaussian,

$$I(t) = I_0 \exp\left[\frac{-(t-t_0)^2}{2\tau^2}\right], (t \leqslant t_0) \tag{2.1}$$

where I_0 is the background-subtracted peak count rate, t_0 is the peak time, and τ is the characteristic rise time. For this flare, 5127 flaring pixels (each of size $1''$ by $1''$) are identified from UV images with 3 s cadence. The light curve of each pixel is smoothed to 10 s and its rise phase is fitted to a half Gaussian. Examples of the fit to the observed light curve are plotted on the top panel of Figure 2.2. Histograms of the

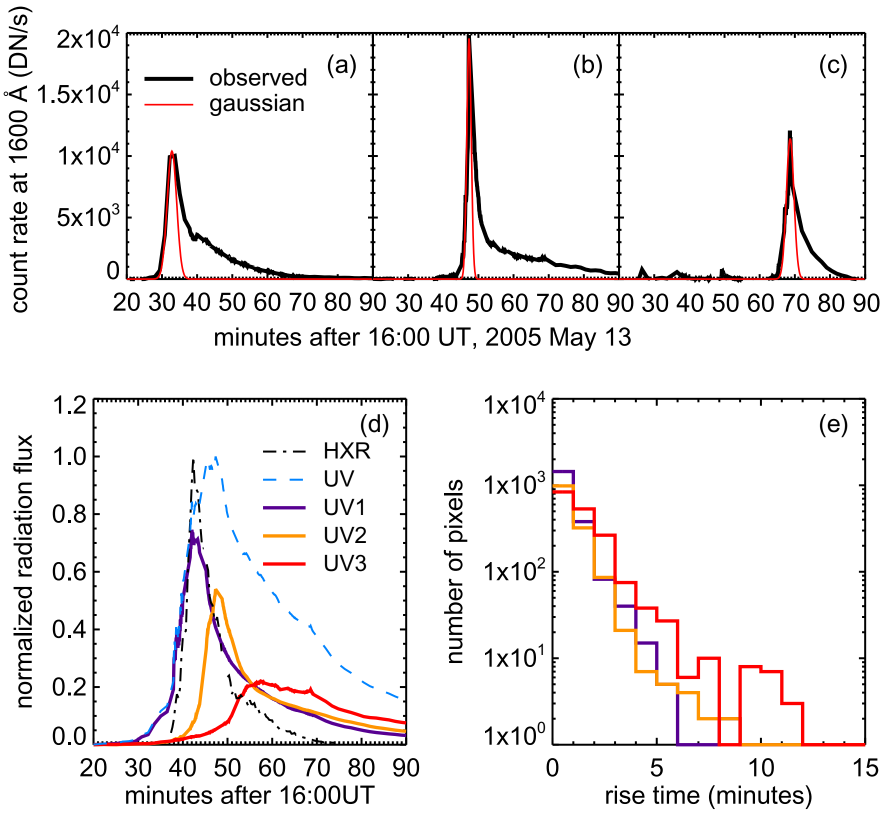

Figure 2.2: Upper: observed UV 1600 Å light curves (thick black line) of three different flaring pixels, superimposed with the Gaussian function (thin red line) which fits the impulsive rise of each individual light curve. Bottom left: normalized background-subtracted UV light curve of all flaring pixels, and UV light curve of pixels peaking at three different stages (see text), compared with the HXR 25–50 keV light curve. The UV light curves are normalized to the maximum of the total UV light curve. Bottom right: histograms of the rise times of UV light curves for pixels brightened at three different stages as shown in the bottom left panel.

rise times from fits to all the flaring pixels are given in the bottom panel of Figure 2.2, showing that most flaring pixels rise over timescales from a few tens of seconds to a few minutes. These rise times are systematically shorter than those derived by Qiu et al. (2012) in another C3.2 flare. This may be due to the higher cadence (3 s) of the observations in this flare compared with the 30 s cadence of the other data, or more likely, the more impulsive nature of this flare that has significant non-thermal emission.

Observations also show that UV pixels peaking after 16:52 UT, when the HXR emission has been reduced significantly, tend to evolve more slowly than those peaking earlier. This suggests different evolutionary timescales in both the heating and cooling phases when energy is transported through flare loops by different mechanisms, by non-thermal electrons or by thermal conduction. To examine the distinction, we compare UV light curves of pixels peaking in three stages relative to the HXR evolution. Pixels in the first stage (UV1) peak before 16:45 UT when HXR emission is significant. These pixels are marked in dark black to light blue colors in Figure 2.1, and the sum of their light curves (purple curve in Figure 2.2d) has a very good temporal correlation with the HXR light curve. UV pixels categorized in the second stage (UV2) peak during the HXR decay from 16:45 UT to 16:52 UT. The sum of their light curves (orange in Figure 2.2d) contributes mostly to the peak of the total UV light curve. UV pixels in the third stage (UV3; red in Figure 2.2d) peak after 16:52 UT, when $\geq$25 keV HXR emission has nearly ended. Compared with UV1 and UV2, the UV3 light curves evidently rise more slowly and also decay more gradually. In Figure 2.2e, we plot the histograms of the rise times for pixels at the three stages, which shows that UV3 pixels rise more slowly on average. The differences of the UV light curves in the three stages indicates the different effects of beam heating and conductive heating on UV emissions, and in turn, the UV evolution could give us a clue to the nature of energy release, thermal or non-thermal.

Hydrodynamic and radiative transfer models of the lower atmosphere during flares have shown that the lower atmosphere responds within a few seconds to the onset of impulsive energy injection (Emslie & Nagai, 1985; Fisher et al., 1985a; Canfield & Gayley, 1987). Therefore, the rapid rise of UV emission from the upper atmosphere or transition region may be considered to scale with the impulsive energy release in reconnection-formed flare loops. With this idea, we have implemented a method to construct heating functions and used them to compute plasma evolution in flare loops for a C3.2 flare, which is primarily a thermal flare (Qiu et al., 2012). In this study, we apply the same method, using the rising UV emission at the foot-point as an indicator of energy injection into the newly formed flare loop (or flux tube) rooted at the foot point. We take the start-time of the UV brightening as the onset of the reconnection event forming the new flux tube. The rise time of the UV brightness gives the duration of the impulsive energy release in the newly formed tube, and the maximum brightness of the pixel reflects the magnitude of the energy release (or heating rate) in the flux tube; this simply assumes that a brighter pixel is more strongly heated. These observationally measured quantities may then be used to construct heating rates and study subsequent plasma evolution inside flare loops that are formed and heated sequentially during the flare. In constructing the heating functions, significant progress in the present study is inclusion of the heating term by non-thermal particles that are evident during the impulsive phase.

2.3 Modeling Plasma Evolution in Flare Loops

We have identified over 5000 brightened pixels of size $1''$ by $1''$ in *TRACE* 1600 Å images, and assume that a half loop (or flux tube) of constant cross-section ($1''$ by $1''$) is anchored at each of the pixels. These are half loops, because we do not identify connectivity between positive and negative foot-points. For each half loop, we compute the time-evolution of plasma density, temperature, and pressure averaged along the loop using the EBTEL model. The energy input term in the model, the heating rate, is constructed from observed UV count rates at the foot point. The time-dependent differential emission measure (DEM) is then derived from these 5000 half loops, which will be used to compute SXR flux and compare with observations by *RHESSI* and *GOES* in Section 2.4.

2.3.1 Loop Evolution via EBTEL

The 0D EBTEL model calculates mean properties of loop plasmas, which have been shown to reasonably agree with mean values from simulations using the 1D hydrodynamic code called Adaptively Refined Godunov Solver (ARGOS; Antiochos et al., 1999). The 0D model is highly efficient at computing plasma evolution for over 5000 half loops in our study of the M8.0 flare. The EBTEL model solves two equations. The energy (or pressure) equation takes into account the prescribed heating rates (H) as the energy input term and coronal radiative loss (R_c) as well as the total loss (R_{tr}) through the base of the loop (so called transition region) as energy loss terms. The mass equation is governed by mass flow between the transition region and the corona. In the EBTEL model, this flow is a result of the difference between the energy input, including the beam heating and conductive flux (F_0) from the corona, and the total loss (R_{tr}) at the base (transition region). During the heating phase, the energy input to the transition region dominates the loss term, driving upflows known as chromospheric evaporation. During the decay, the coronal plasma in the loop is cooling through thermal conduction and radiation; meanwhile, the loss through the transition region exceeds the conductive flux into it, which drives downflows, called coronal condensation.

The mean coronal electron density (n) and pressure (P) in each loop evolve according to the EBTEL equations,

$$\frac{dn}{dt} = -\frac{c_2}{5c_3k_\mathrm{B}T}\left(\frac{F_0}{L} + c_1n^2\Lambda(T) - \frac{\Gamma(t)}{L}\right) \tag{2.2}$$

$$\frac{dP}{dt} = \frac{2}{3}\left[Q(t) - (1+c_1)n^2\Lambda(T) + \frac{\Gamma(t)}{L}\right] \tag{2.3}$$

The mean temperature T is determined by the ideal gas law, $P = 2nk_\mathrm{B}T$ (including both electrons and ions). In the equations, k_B is Boltzmann's constant, c_1 is the ratio of the loss through the transition region to the coronal radiation (R_c/R_{tr}), c_2 is the ratio of the average coronal temperature to the apex temperature, and c_3 is the ratio of the coronal base temperature to the apex temperature. With the symmetry assumption, EBTEL only models heating of a half loop, with L being the length of the half-loop. We prescribe two heating terms in the equation: the *ad hoc* volumetric heating rate, $Q(t)$, and the energy flux carried by beam-driven upflows, $\Gamma(t)$. The coronal radiative loss is given by $R_c = n^2\Lambda(T)$, $\Lambda(T)$ being the empirically-determined radiative loss function for optically-thin plasmas (see equation (3) of Klimchuk et al., 2008, for details). F_0 is the conductive flux at the base of the corona, which is defined by Klimchuk et al. (2008) as the location where thermal conduction changes from being an energy loss above to an energy source below. The classical form of conductive flux is used (Spitzer, 1962),

$$F_0 = -\kappa_0 T^{5/2}\frac{\partial T}{\partial s} \approx -\frac{2}{7}\kappa_0\frac{(T/c_2)^{7/2}}{L} \tag{2.4}$$

where κ_0 is the thermal conductivity coefficient, taken to be 1.0×10^{-6} in cgs units. In the EBTEL model, F_0 is saturated for large temperature gradients; in the latest version of EBTEL (Cargill et al., 2012a,b), gravity is included in calculating c_1 for semi-circular loops, while the dependence of c_2 and c_3 on gravity is negligible.

There are three parameters in the EBTEL models, c_1, c_2, and c_3. In the latest version of EBTEL (Cargill et al., 2012a,b), which is used in the this study, c_1 is self-consistently determined by plasma properties inside the loop. Its value varies about the mean value 2.1 during flux tube evolution, which is not very sensitive to different heating rates in different flux tubes. Fixed values of $c_2 = 0.87$ and $c_3 = 0.5$ are used in the study. These are mean values determined from 1D simulations. In the simulations, c_2 and c_3 usually change during the loop evolution, but only within a small range. For simplicity, in this study, we use fixed mean values of c_2 and c_3 for 5000 loops throughout their evolution, considering that differences produced by using varying values of these parameters will become insignificant when we sum up contributions from 5000 loops.

The critical input to the EBTEL model, also a focus of our present study, is the heating rate. In general, it includes two parts. The first contribution, denoted by an *ad hoc* volumetric heating rate Q (in units of erg cm^{-3} s^{-1}), is by *in situ* heating in the corona. It may result from current dissipation, shocks (e.g., Longcope et al., 2010; Longcope & Guidoni, 2011), electrons trapped and scattering in the corona(e.g., Somov & Kosugi, 1997; Karlický & Kosugi, 2004; Caspi & Lin, 2010), or even return current (e.g., Knight & Sturrock, 1977; Emslie, 1980; Holman, 2012). In the present study, the exact mechanisms for this terms are not discussed. The second contribution, denoted as Γ (in units of erg cm^{-2} s^{-1}), is coronal heating *from the lower atmosphere* due to evaporation driven by non-thermal electrons that precipitate at the lower atmosphere during the impulsive phase. Of the total flux carried by a non-thermal beam, Γ is a fraction of that sent back upward into the corona. These two terms are distinguished as they heat the corona in different ways, Q by primarily raising the temperature of the coronal plasma, and Γ by primarily raising the density - therefore the Γ term also enters the density equation. Predictably, the different heating styles result in different evolutionary patterns. Furthermore, these two terms play different roles in different stages of the flare. Specifically, the Γ term as driven by beams is included only during the impulsive phase when thick-target HXR emission is evident.

We must note that thermal conduction alone is able to produce chromospheric evaporation, which, in the EBTEL model, is the consequence of coronal evolution when the conductive flux exceeds the loss through the lower atmosphere during the heating phase, and is therefore not treated as an additional coronal heating term. The Γ term, on the other hand, is considered in this study to be produced by particles that instantaneously heat the lower atmosphere, and drive upflow *independent of* the coronal situation. Therefore, this term contributes to both energy and density of coronal plasmas.

For the 2005 May 13 flare, *RHESSI* observations show that there is significant HXR emission with energy up to 300 keV during the first ten minutes of the flare. So both *in situ* heating in the corona and heating by beam driven upflow are considered in this chapter. Until now it has proven difficult in general to distinguish these two contributions, either theoretically or observationally. In this study, we use an empirical method to introduce these two terms as scaled with the UV and HXR light curves. Determination of these two heating terms and the effect of the partition between the two will be discussed in the following text.

2.3.2 Constructing Heating Functions in Flare Loops

Following Qiu et al. (2012), we assume that the heating rate in a flare loop (or a flux tube) is proportional to the rise of the UV light curve at its foot-point, given as:

$$H_i(t) \equiv Q_i(t)L_i + \Gamma_i(t) = \lambda I_i \exp\left[-\frac{(t-t_i)^2}{2\tau_i^2}\right] \text{ erg s}^{-1}\text{ cm}^{-2};\ (0 < t < \infty) \qquad (2.5)$$

H_i is the total heating flux in the loop anchored at ith pixel, which is composed of the *ad hoc* heating rate (Q_iL_i) and the beam-driven flux (Γ_i). Although we only fit the rise of the UV light curve to a half Gaussian, we consider the heating function to be symmetric, or a full Gaussian. Assuming semi-circular flare loops, we estimate the length of the ith half loop by $L_i = \frac{\pi}{2}D_i$, where D_i is the distance of the foot-point to the polarity inversion line. As observed, flare ribbons expand away from the polarity inversion line in a rather organized manner; therefore, L_i approximately grows linearly with the time of flare brightening (t_i). For the 5000 half loops, L_i ranges from 35 to 55 Mm. Although loops are in general not semi-circular, our experiments have shown that variations of the loop lengths within a factor of 1.5 do not significantly change the synthetic total emission.

To relate the total heating rate to UV emission, we employ a scalar λ that converts the count rate (DN s^{-1}) to a heating rate (erg s^{-1}). The value of this parameter depends critically on the lower atmospheric response to beam heating or conductive heating and on mechanisms of UV emission. As a rule of thumb, we consider that λ takes a larger value when conduction heating dominates than when beam heating dominates, for the simple reason that, with the same amount of energy, beam heating occurring in the lower atmosphere would generate stronger UV emission than conductive flux (e.g., Emslie & Nagai, 1985). In this study, λ takes the value of 1.9×10^5 ergs DN^{-1} for loops whose foot-point UV light curves peak before 16:48 UT, then linearly increases until 16:52 UT; afterwards, when HXR emission has finished, λ stays constant at 2.5×10^5 ergs DN^{-1}. Note that in this study, we do not model the lower atmospheric heating and dynamics, but instead use this simple empirical model to minimize the number of free parameters. The λ values quoted here are determined by best matching the model-computed time-dependent SXR emissions with those observed by *GOES*, as will be described in the next section. These λ values, combined with the peak count rates, correspond to the peak heating flux (H) of order 10^8 to 10^{10} ergs s^{-1} cm^{-2} for the few thousand half loops in our model.

In the heating term, the coronal *in situ* heating QL is present in all flare loops; Γ is present only for loops brightened during the impulsive phase (UV1 and UV2 pixels), and is gradually switched off after 16:52 UT (UV3 pixels). For one loop, the *ad hoc* heating rate and beam driven energy flux both have the same Gaussian time profile of $\exp{[-(t-t_i)^2/(2\tau_i^2)]}$, and the partition of the beam driven energy flux, i.e., Γ_i/H_i, is constant. For different loops heated at different times represented by t_i, the partition Γ_i/H_i is different; whereas the net heating flux H_i in a loop is proportional to the UV count rate at the foot-point, the beam driven flux Γ_i is assumed to be proportional to the $\geq$25 keV HXR light curve. This rather simplified treatment can be justified by the hydrodynamic simulations of chromospheric evaporation showing that the evaporation upflow roughly increases as the heating energy flux increases (Fisher et al., 1984, 1985b) in the range of 10^9–10^{10} erg s^{-1} cm^{-2}. The estimated heating flux of the majority of flux tubes in the impulsive phase in our study is within this range. During the impulsive phase, the HXR spectral index does not vary significantly (not shown in this chapter), so we can approximate the total beam energy flux, and subsequently the energy flux in the beam driven upflow, as proportional to the HXR count rate light curve. The partition Γ_i/H_i, therefore, is time-dependent, and is empirically given by $\Gamma_i/H_i = \gamma_m \eta(t_i)$, where $\eta(t_i)$ is a time-dependent function that tracks the HXR light curve, $\gamma_m = 0.4$ is the maximum partition of the non-thermal energy flux used in this study, and this maximum partition occurs when HXR emission peaks at about 16:42 UT.

In addition to the impulsive flare heating, a constant background heating rate of order 1×10^{-4} ergs s^{-1} cm^{-3}, which is a few thousandths of the maximum heating rate constructed from UV observations, is imposed on each loop to produce an initial equilibrium of an average coronal temperature of 1.8 MK and density of 6×10^8 cm^{-3}. Qiu et al. (2012) have shown that neither the initial state of the loop nor the background heating will affect the plasma evolution as soon as impulsive heating occurs, since the flare heating rate is a few orders of magnitude larger than the background heating rate.

The so devised heating function in a single flux tube is mostly constrained by foot-point UV and HXR observations, but also depends on two free parameters λ and γ_m. λ determines the total amount of energy used to heat the corona, and γ_m determines the non-thermal partition. Since heating via upflows or via direct heating leads to different plasma evolution patterns, the resultant coronal radiation spectrum will differ. Our recent experiments with another flare have shown that model-predicted coronal radiation by high temperature plasmas is very sensitive to parameters defining the heating function but rather insensitive to other model parameters like c_1 (Qiu et al., 2012). Therefore, these parameters will be eventually constrained by comparing model-predicted and observed X-ray emission. In this study, we start the model with an initial guess of the parameters, and gradually adjust them so that the synthetic SXR spectrum and light curves best match those observed by *RHESSI* and *GOES*.

2.3.3 Evolution of Flare Plasma in One Loop

With the methods described above, we compute plasma evolution in each flux tube anchored at the UV flaring pixel using the EBTEL model. Figure 2.3 shows, in the left panel, time profiles of the mean temperature (solid) and density (dashed) of a single flux tube rooted at its UV foot point with constant cross-sectional area $1''$ by $1''$. It is heated impulsively by a Gaussian-profile heating rate (red dot-dashed line in the right panel) constructed from the UV light curve (black solid line in the right panel) with $\tau = 50$ s, and $H_{max} = 9 \times 10^9$ ergs s^{-1} cm^{-2}, of which 40% is carried by the beam-driven upflow. The λ and γ_m values used here are determined from comparing synthetic SXR light curves and spectra with observations, which will be described in the following sections.

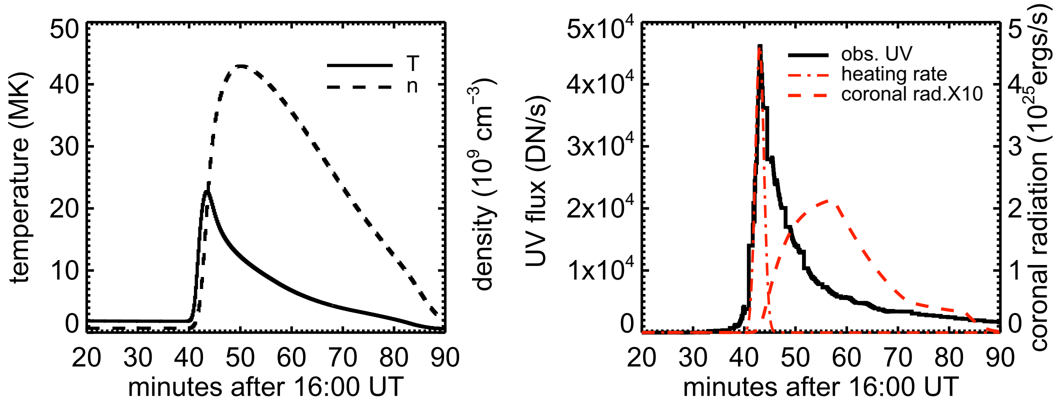

Figure 2.3: Evolution of plasma properties in a flare loop with cross section 1″ by 1″ rooted at one flaring pixel. Left: computed time profiles of coronal-averaged temperature (solid) and density (dashed) of the flare loop. Right: observed UV 1600 Å count rate light curve (solid black line), the constructed heating function (dot-dashed red line), and computed coronal radiation rate (dashed red line) of the loop.

Coronal temperature rises as the flux tube in the corona is heated by *ad hoc* heating. At the same time, the lower atmosphere is heated by non-thermal electron beams and conductive flux, giving rise to enhanced UV emission as observed by *TRACE*. Chromospheric evaporation is driven to fill the coronal loop. An increase in coronal density leads to enhancement of coronal radiation (red dashed line in the right panel), which then cools the plasma in the flux tube. The coronal temperature begins to decline immediately after the peak of the heating, but the density continues to grow until the energy loss in the transition region exceeds the conduction flux, causing a downward flux, or coronal condensation. The coronal density and radiation then decline, and the flux tube experiences a long decay. Notably, the observed UV

1600 Å emission decays on the same timescale of coronal evolution. This has been previously known as optically-thin transition region lines, such as the resonant C IV line that dominates the 1600 Å broadband UV emission, behave as a "coronal pressure gauge" (Fisher, 1987; Hawley & Fisher, 1992).

2.3.4 Effect of Beam Driven Flux on Plasma Evolution

To determine γ_m, we investigate the effect of beam driven flux in the EBTEL model. We examine the evolution of coronal plasma in the same flux tube shown in Figure 2.3 with the same impulsive heating rate $H_{max} = 9 \times 10^9$ ergs s^{-1} cm^{-2} but with varying partition, i.e., Γ/H values. The time profiles of coronal-averaged temperature, density, and pressure with different Γ/H values are plotted in Figure 2.4.

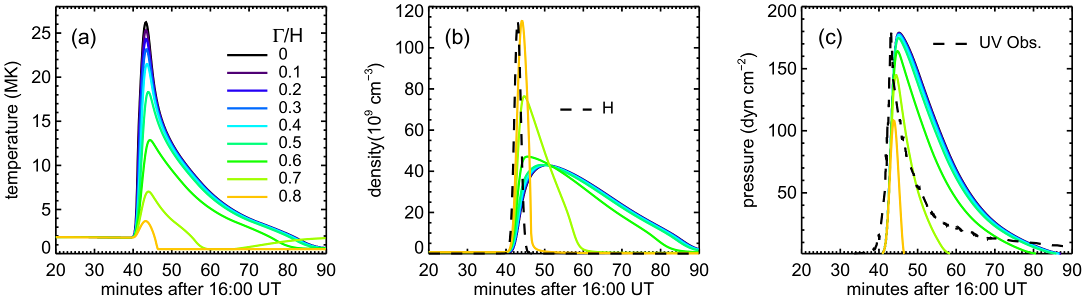

Figure 2.4: Evolution of coronal-averaged temperature (a), density (b), and pressure (c) of a flux tube with varying fraction of energy flux carried by beam driven upflows, $\Gamma/H = 0$–0.8. Also plotted in dashed lines are arbitrarily scaled total heating rate in panel (b) and observed UV light curve in panel (c).

It is shown that, in general, a greater amount of beam driven flux results in lower temperature and higher density. If the beam driven flux does not dominate, i.e., $\Gamma/H < 0.5$, the average temperature decays to 10 MK in a few minutes, and then continues to decay toward the pre-flare value. From about ten minutes after the heating, the decay of coronal temperature and density is nearly identical for different Γ/H values. The same evolution pattern of the apex density and temperature is also displayed in 1D hydrodynamic simulations by Winebarger & Warren (2004), who modeled loop heating with thermal conduction. Their study showed that a flare loop impulsively heated by the same amount of the total energy, but with varying magnitude and duration and at different locations along the loop, would reach the same equilibrium point when radiation and conduction are comparable, and the evolution of the apex density and temperature is identical thereafter.

On the other hand, when the beam driven flux dominates the energy budget with $\Gamma/H > 0.5$, the flux tube will attain much higher density in a short time due to strong upflow. Meanwhile, less direct heating Q results in a lower peak temperature. The two effects, high density and low temperature, lead to faster radiative cooling in the decay phase. Therefore, the flux tube evolves on much shorter timescales. A similar evolution pattern has also been produced in the 1D numerical simulation that takes into account beam heating with different pitch angles (Reeves et al., 2012).

The experiment above suggests that varying the partition parameter Γ/H will lead to different temperature and density in the heating phase, and for very large Γ/H values, evolution of the flux tube in the decay phase is also modified significantly. Therefore, the experiment provides us with two ways to estimate the optimal Γ/H value in this flare. First, we may compare the synthetic SXR spectrum using the DEM from modeling over 5000 flux tubes with the X-ray spectrum observed by *RHESSI* during the heating phase. Figure 2.5 shows the DEM constructed using different γ_m values for the 5000 tubes. It is seen that, given the same amount of total energy, the larger value of γ_m, i.e., the larger amount of energy carried by beam driven upflow, will lead to greater DEM increase at lower temperatures, whereas the DEM at the high temperature end would be reduced. Such variation will affect the synthetic SXR spectrum formed at the temperature range of a few to a few tens of MK. Therefore, the value of γ_m can be estimated by comparing the synthetic SXR spectra with *RHESSI* observations, as will be presented in Section 2.4.2.

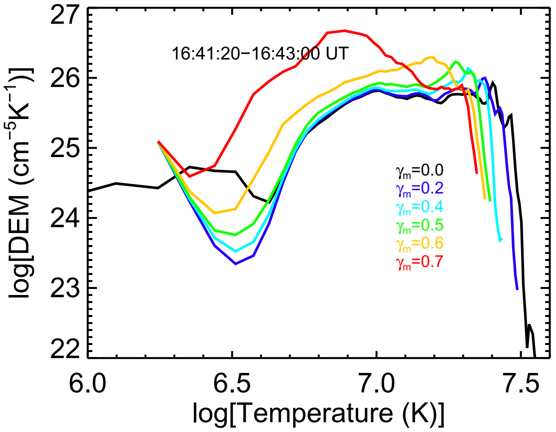

Figure 2.5: The differential emission measure (DEM) derived from multiple flare loops from 16:41 to 16:43 UT, with different γ_m but the same total heating rates.

Second, we will compare the observed and modeled timescales of the foot-point UV emission during the decay phase of the flare, based on the principle that UV line emission behaves as a coronal pressure gauge in the decay phase (Fisher et al., 1985a; Fisher, 1987; Hawley & Fisher, 1992). These will be elaborated on in Section 2.4.3.

As a quick look, the right panel of Figure 2.4 shows the observed UV light curve versus pressure; it appears that the UV emission decays on the same timescale as the coronal pressure for $\Gamma/H < 0.5$.

2.3.5 Properties of Coronal Plasmas in Multiple Flare Loops

Our methods yield the best estimate of λ and γ_m, with values given in Section 2.3.2, with which we can determine heating functions of over 5000 flux tubes. The left panel of Figure 2.6 shows the time profiles of the total *in situ* heating rate ($\sum Q_i L_i$) and total beam heating rate ($\sum \Gamma_i$) summed for all the flux tubes, in comparison with the observed UV total counts light curve and HXR 25-50 keV counts light curve. The total heating rate ($\sum H_i$) is shown nearly scaled with the total UV count rate light curve from the rise to the peak – note that the decay of the UV light curve is governed by coronal evolution, which is not part of the heating. The beam driven energy flux is proportional to the observed $\geq$25 keV HXR light curve. The time integral of the total heating rate and beam heating rate yields the estimate of the total energy used to heat the corona and the total energy carried by beam-driven upflows in this flare, which are 1.22×10^{31} ergs and 1.9×10^{30} ergs, respectively. The figure shows that the largest non-thermal partition amounts to about 40%, which occurs around the peak of HXR emission at 16:42 UT. Note that although the total heating flux H_i in a single flux tube is considered to be proportional to the UV light curve at the foot-point, the sum of the total heating fluxes in all flux tubes,

$\sum H_i = \sum(Q_i L_i + \Gamma_i)$, is scaled with the total UV light curve by different values of λ during different phases of the flare, as can be seen from the Figure. λ is time-dependent in our method; given the same amount of energy, beam heating produces greater UV emission compared with conduction heating (Emslie & Nagai, 1985).

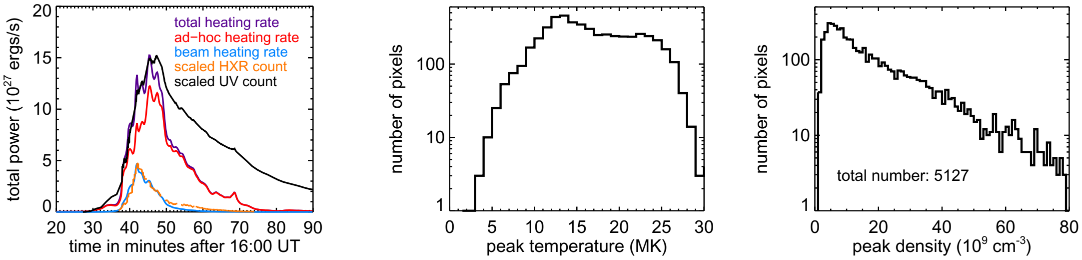

Figure 2.6: Left: the sum of the total heating rate (purple), ad hoc heating rate (red), and beam heating rate (blue) in all flare loops, in comparison with the observed total UV light curve (black) and HXR 25–50 keV light curve (orange), both arbitrarily scaled. Right: peak temperature and density distributions in over 5000 modeled flare loops with lengths in the range of 35–55 Mm and cross-sectional area of 1″ by 1″.

With these heating rates, we compute plasma evolution in over 5000 flare loops formed by reconnection and heated at different times and by different amounts of energy. The distribution of the peak temperatures and densities of these flux tubes is shown in the right panels of Figure 2.6. For this flare, the peak temperature of most flux tubes varies from 7 to 26 MK, and the peak temperature distribution appears bi-modal. The second peak in the distribution at around 22 MK is mostly contributed by flare loops formed around 16:45 UT, and is close to the effective temperature derived from the ratio of the two-channel (1–8 Å and 0.5–4 Å) emission measured by *GOES* with the isothermal assumption (White et al., 2005). The peak density of the flux tubes ranges from 5–30 × 10^9 cm^{-3}. The DEM of the coronal plasma is readily calculated from the temperatures and densities of these loops. Figure 2.7 shows the time evolution of the coronal plasma DEM averaged every 20 seconds for the M8.0 flare. Note that the higher DEM at about 2 MK at the beginning of the flare is due to background heating. It is seen that in the rise phase of the flare, the DEM increases toward higher temperature, suggesting that more flux tubes are heated to higher temperatures, while during the decay phase, the DEM rises at lower temperature, reflecting cooling of the flux tubes. The time evolution of the coronal DEM will be used to calculate time-dependent SXR emission to verify the model results, as discussed in the next Section.

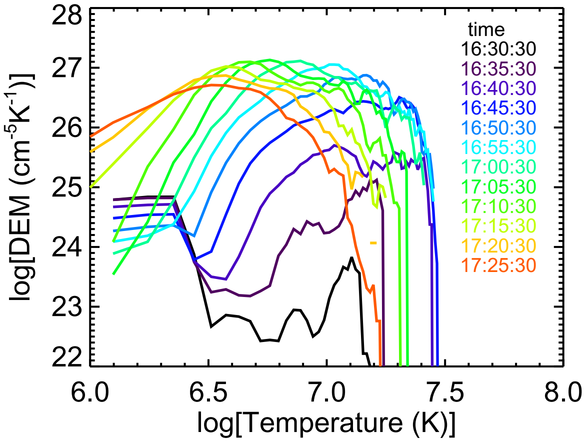

Figure 2.7: Time evolution of the coronal DEM from the model of the 2005 May 13 flare. The high emission measure at low temperature at the beginning of the flare is produced by background heating.

2.4 Comparison with Observations

The time-dependent coronal DEM computed from over 5000 flux tubes is convolved with instrument response functions to compute synthetic SXR light curves and spectra, which are compared with those observed by *GOES* and *RHESSI* (Sections 2.4.1 and 2.4.2, respectively). The transition region DEM during the decay phase is also derived from the coronal pressure (Fisher et al., 1985a; Fisher, 1987; Hawley & Fisher, 1992), with which we calculate the the C IV line emission using the CHIANTI atomic database (Dere et al., 1997; Landi et al., 2012), and compare it with UV 1600 Å observations (Section 2.4.3).

2.4.1 Comparison with *GOES* Light Curves

The two X-ray Sensor (XRS) photometers onboard *GOES* measure full-disk integrated SXR emissions in two energy bands, 1–8 Å and 0.5–4 Å, with 3-second cadence. The solar 1–8 Å flux, which is dominated by continuum emission (Mewe, 1972; Kato, 1976), is believed to originate from hot ($T > 10^6$ K) plasma in coronal loops in active regions. The full-disk SXR images observed by the Solar X-ray Imager (SXI; Hill et al., 2005; Pizzo et al., 2005) onboard *GOES* indicate that NOAA Active Region 10759, where the M8.0 flare occurred, is the dominant SXR source on 2005 May 13 from 16:00 UT to 20:00 UT (images not shown here). Therefore, the background-subtracted *GOES* light curves reflect SXR emissions by the M8.0 flare. The comparison of the synthetic SXR light curves from the modeled flare plasma with the observations by *GOES* XRS yields the best-fit model parameter λ.

Figure 2.8 shows the synthetic SXR emissions in two channels plotted against the observed light curves. In both band-passes, the synthetic light curves follow the observed ones very well from the rise until 16:50 UT. In the 0.5–4 Å channel,

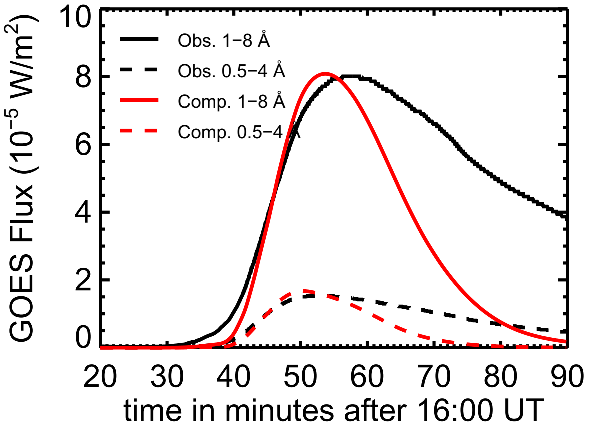

Figure 2.8: Comparison of the computed (red) and *GOES* observed (black) SXR fluxes at 0.5–4 Å (dotted) and 1–8 Å (solid).

the modeled and observed fluxes start to decline at around the same time, but the modeled flux decays more rapidly than the observed. In the 1–8 Å channel, the modeled radiation flux begins to drop while the observed radiation continues to rise for another 5 minutes. We also note that at the start of the flare before 16:40 UT, the observed *GOES* 1–8 Å flux starts to rise earlier than the modeled flux. As discussed by Qiu et al. (2012), simply changing model parameters cannot compensate for the flux deficiency; instead, these discrepancies are most likely caused by weak heating events in the very early and late phases of the flare, which might not be identified in the UV foot-point emission.

2.4.2 Comparison with *RHESSI* Soft X-ray Spectra and Light Curves

RHESSI is designed to observe solar high-energy emissions from SXRs to gamma-rays (3 keV up to 17 MeV) with an unprecedented combination of high time, spatial, and spectral resolutions (Lin et al., 2002). Whereas the thick-target HXR ($\gtrsim$20 keV) observations provide us with a guide for constructing heating functions, we will further compare the model computed SXR ($\lesssim$20 keV) spectrum with that observed by *RHESSI*. The 3 to $\lesssim$20 keV X-ray emission is usually thermal bremsstrahlung radiation produced by plasmas in the flare loops heated to temperatures of a few to a few tens of MK. *RHESSI* images confirm that this emission is generated in the corona.

We calculate the time-dependent SXR spectrum using the DEM distribution obtained from our model (see Figure 2.7). At each time (20 s cadence), we first calculate the X-ray spectrum observed at Earth (in units of photons cm^{-2} s^{-1} keV^{-1}) from the optically-thin thermal bremsstrahlung radiation using CHIANTI (Dere et al., 1997; Landi et al., 2012), including both the line and continuum contributions and assuming solar coronal abundances (Feldman et al., 1992) and ionization equilibrium (Mazzotta et al., 1998). The calculated spectrum is then convolved with the *RHESSI* detector response (Smith et al., 2002), obtained from pre-flight and in-flight instrument calibration and modeling, to convert the photon spectrum to the count spectrum that would be directly observed by *RHESSI*. The detector response accounts for instrumental effects due to pulse pileup, escape of K-shell fluorescence photons from the detectors, attenuation by the aluminum shutters, and the energy-dependent detector effective area, and includes the additional in-flight corrections from Caspi (2010). To get the best comparison of the spectra, only detector G4 is used since it had the best in-flight resolution at the time of the flare (Smith et al., 2002). By integrating the synthetic spectrum over different photon energy ranges, we also obtain synthetic SXR light curves in units of counts rate.

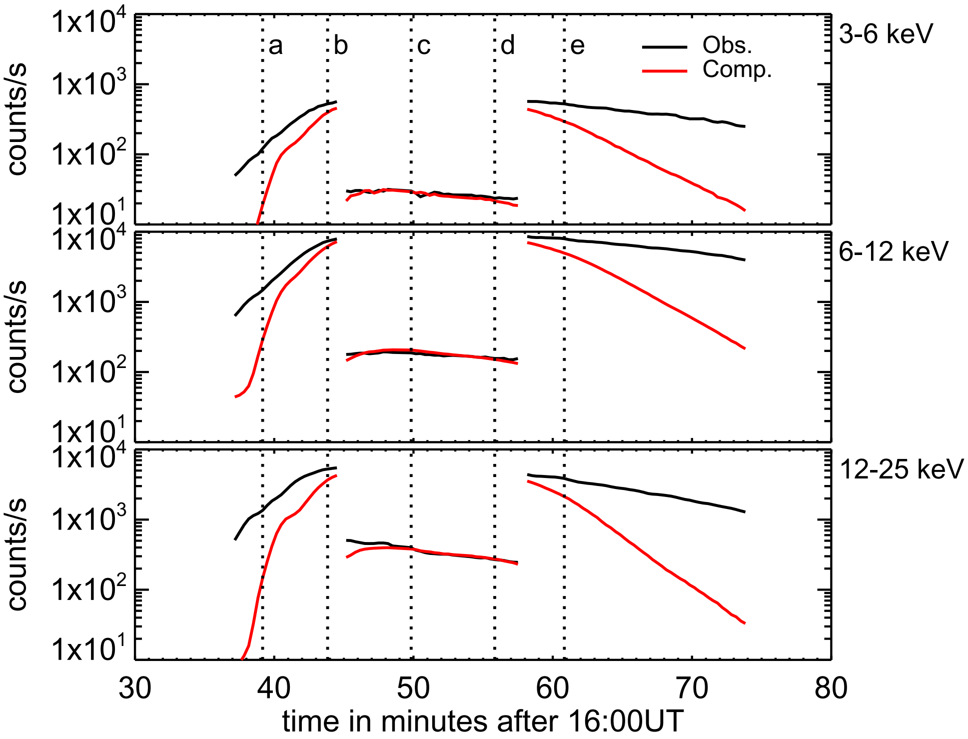

Figure 2.9: Comparison of the synthetic SXR light curves from the model (red) with *RHESSI* observations (black) in the 3–6 keV, 6–12 keV, and 12–25 keV bands. The vertical dotted lines and letters a–e indicate the times when the spectral comparison is plotted in Figure 2.10. The discontinuities in the light curves at 47 min and 57 min are due to changes of the *RHESSI* attenuator state, when the thick shutter is inserted and later removed.

Figure 2.9 shows the synthetic SXR light curves in the 3–6, 6–12, and 12–25 keV bands, respectively, in comparison with *RHESSI* observations. For most of the impulsive phase, the synthetic light curves agree very well with the observed ones. The synthetic fluxes are lower than observed at the start of the flare, for a few minutes after 16:37 UT, when *RHESSI* emerges from eclipse. They then rise rapidly to catch up with the observed fluxes as more flare loops formed and heated by reconnection are identified in the UV foot-point observation. The computed and observed fluxes overlap for 15 minutes from 16:44 UT until 16:59 UT, well after the impulsive phase. Afterwards, the computed fluxes start to drop faster than observed. This is consistent with the model-observation comparison of the *GOES* light curves, which usually yield slightly lower plasma temperatures than RHESSI light curves (e.g., Hannah et al., 2008; Caspi & Lin, 2010).

More details can be learned by comparing the SXR spectra. Figure 2.10 illustrates the synthetic and observed spectra at a few different times, indicated in the top panel of Figure 2.9, during the flare. (For a complete view, a movie comparing the modeled and observed SXR spectra, from 16:37 to 17:15 UT with 20 s cadence, is available online.) Figure 2.11 summarizes the comparison of the time-dependent spectra with two quantities, the ratio of the synthetic to the observed counts, $\rho(\epsilon) = C_m(\epsilon)/C_o(\epsilon)$, averaged over the photon energy range ϵ from 6 to 15 keV, and the slope α of this energy dependent ratio versus the photon energy, which is obtained by fitting the ratio to a linear function of the photon energy $\rho(\epsilon) = \alpha\epsilon + b$. If the synthetic spectrum is the same as the observations, $\rho = b = 1$ and $\alpha = 0$. ρ is a measure of magnitude comparison, and we regard empirically that the synthetic and observed spectra agree with each other when ρ ranges between 0.7 and 1.3. α is an indication of the plasma temperature distribution, since the thermal bremsstrahlung spectrum is temperature

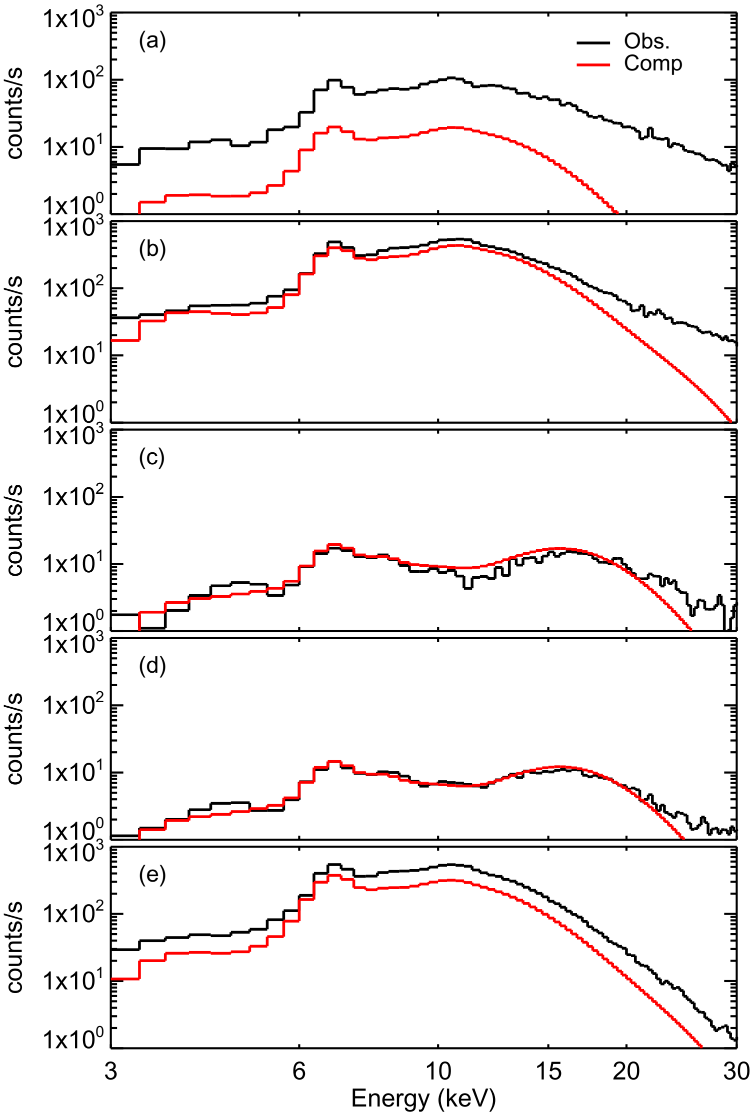

Figure 2.10: Comparison of synthetic SXR spectra from the model (red) with the *RHESSI* observation (black) at a few times during the flare. The time of each panel is indicated by vertical dotted lines in Figure 2.9. For a complete view, a movie is available online, which compares the observed (black) and computed (red) spectra from 16:37 to 17:15 UT, with 20 s cadence.

dependent. When $\alpha > 0$, the model has produced more high temperature plasma than observed, and when $\alpha < 0$, there is a lack of hot plasma in the modeled DEM.

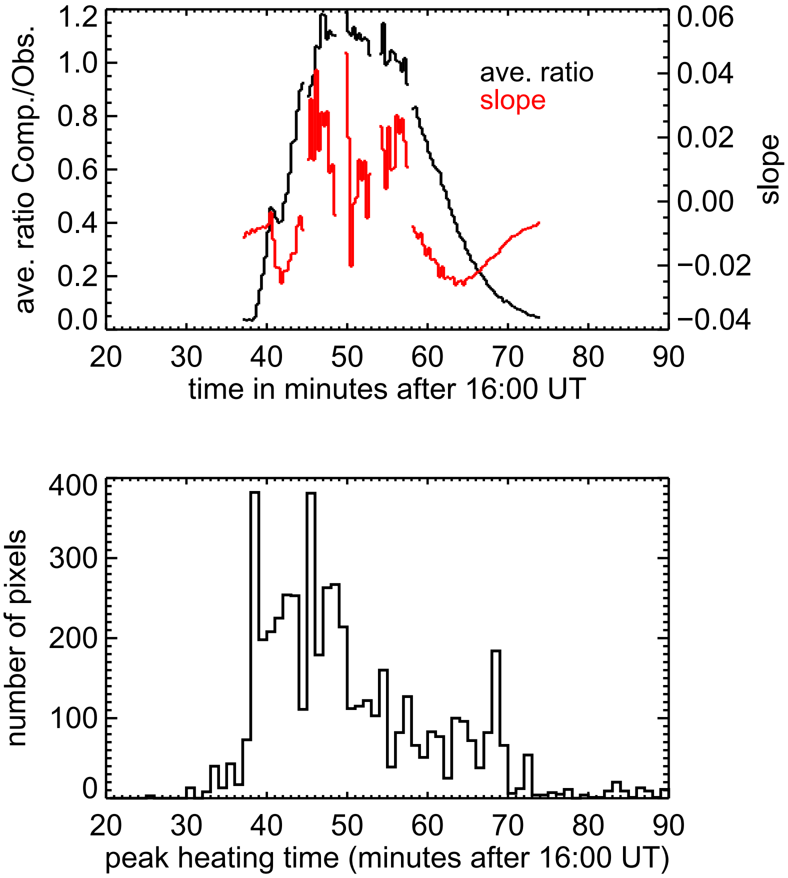

Figure 2.11: Top: time profiles of the ratio (black) of the modeled SXR spectrum to that observed by *RHESSI* averaged over the 6–15 keV band, and slope (red) of the ratio versus photon energy in the 6–15 keV band. Bottom: time histograms of the number of flaring pixels identified from the UV foot-point emission.

In these plots, we only compare the spectrum up to 20 keV, beyond which the spectrum is likely dominated by thick-target bremsstrahlung produced by non-thermal electrons colliding at the lower atmosphere. For most of the impulsive phase, from 16:44 UT to 16:59 UT, the synthetic spectra agree with the observations (see panels b, c, and d in Figure 2.10), with mean ρ value between 0.7 and 1.3 and α close to zero. From 16:50 to 16:55 UT, around the maxima of the *GOES* SXR light curves, the modeled thermal emission dominates up to 20 keV (see panels c and d), indicating strong heating in flare loops although the non-thermal HXR emission has become insignificant. These plots showing good agreement between the model and observations suggest that the model has rather accurately reproduced the DEM responsible for the thermal bremsstrahlung X-ray radiation in the observed range during this period.

From the start of the flare until 16:42 UT, the synthetic spectrum is lower than observed by nearly the same fraction across the energy range up to 15 keV (panel a in Figure 2.10). The synthetic flux at >15 keV is still smaller than observed, which may indicate a lack of high-temperature plasma in the model, but may also be due to predominant non-thermal bremsstrahlung radiation down to 15 keV. *RHESSI* images in the 15–20 keV energy range during this period (not shown) show that the X-ray source is rather extended, likely including emissions from both the foot-point and loop-top, which cannot be resolved with good photometric accuracy. Therefore, both scenarios are plausible. In the late phase of the flare after 17:00 UT, the modeled flux drops below the observed flux again. In this phase, thick-target HXR emission has ended, so the low flux above 15 keV is likely caused by a lack of high temperature plasma in the model. We also note that in the early and late phases of the flare, when the average ratio ρ is far below 1, the slope α becomes negative. These indicate that the model does not generate enough high temperature plasma during these periods, maybe due to a lack of heating events identified in our method. The bottom panel of the figure shows the number of heating events identified during the flare. It is seen that the number of heating events drops rather significantly both before

16:39 UT and after 16:55 UT. It appears that the shortage of heating events leads to insufficient X-ray flux in the calculation about 3 to 5 minutes later, which is roughly the timescale for temperature and density increases in newly formed flux tubes. The lack of heating events identified from lower atmospheric signatures (brightened UV or HXR foot-points) could be explained by the fact that there is neither strong conduction flux nor significant non-thermal beam to deposit enough energy at the lower atmosphere to generate observable signatures. In the rise phase, it is plausible despite the significant non-thermal HXR emission, if the non-thermal electrons are partially or largely trapped in the corona and do not reach the chromosphere to generate HXR foot points; the trapped electrons would then be a source of *in situ* heating in the corona. Such a mechanism has been proposed for the "pre-impulsive" phase of a few large flares (e.g., Lin et al., 2003; Caspi, 2010; Caspi & Lin, 2010) where non-thermal emission is observed in the corona with no identifiable HXR foot points, and may also contribute here.

Comparison between the observed and synthetic spectra, as characterized by ρ and α, provides us with observational constraints to the heating function parameters λ and γ_m, in addition to the observed UV and HXR signatures at the flare foot-points that constrain the time profiles of the heating rate.

2.4.3 UV Emission in the Decay Phase

The long decay of *TRACE* 1600 Å emission in individual flaring pixels is reported by Qiu et al. (2010) and Cheng et al. (2012). Flare emission in this broadband channel includes both the enhanced UV continuum and the C IV line emission. The C IV resonance doublet at 1548 Å and 1551 Å could only be emitted over a very narrow temperature range around 10^5 K, and therefore the C IV intensities rise when the transition region is heated with more plasma raised to 10^5 K during the flare. The C IV irradiance was observed to be enhanced by three to four orders of magnitude over the pre-flare emission during the impulsive phase of a large flare (Brekke et al., 1996). During the decay phase, the C IV emission is dominated by the evolution of coronal pressure (Fisher, 1987; Hawley & Fisher, 1992; Griffiths et al., 1998). The solar UV continuum radiation in the 1000–2000 Å wavelength range is also enhanced during the flare (e.g., Cook & Brueckner, 1979; Cheng et al., 1984, 1988). In particular, the continuum emission below 1682 Å is primarily contributed by bound-free transitions of Si I, which is primarily excited by the C IV doublet (Machado & Henoux, 1982; Machado & Mauas, 1986). Therefore, the continuum intensity at $\lambda < 1682$ Å is approximately proportional to the C IV line intensity (Phillips et al., 1992). Though there is no direct C IV measurement for the M8.0 flare studied in this chapter, observations of stellar flares show that the time profile of C IV is similar to the UV 1600 Å emission in solar flares observed by *TRACE*, both exhibiting a fast rise and a long decay (Vilhu et al., 1998).

In this study, we have used the rapid rise of UV emission to constrain the time, duration, and magnitude of the heating rate in individual flare loops. The gradual decay of UV emission from the same foot-points reflects the evolution of the overlying corona that has been heated impulsively and then cools down on a much longer timescale. Using the coronal plasma properties from the model, we further calculate the C IV line emission during the decay phase to compare with the *TRACE* UV observation.

To calculate the C IV line emission on the solar surface, it is important to know the opacity. Doschek et al. (1991) and Dere & Mason (1993) measured the intensity ratio of two C IV lines at $\lambda1548$ and $\lambda1550$ observed on the disk, and found the ratio very close to 2:1, which is expected for optically thin lines. Doschek (1997) also estimated the opacity of C IV to be 0.099 in the active-region spectrum. We therefore consider that the C IV line is optically thin. The C IV photon flux at the surface is then calculated through

$$I_{\mathrm{C\ IV}} = A_b \int_0^\infty C(T,n)\ \mathrm{DEM}(T)\ \mathrm{d}T \text{ photons cm}^{-2}\text{ s}^{-1}\text{ sr}^{-1} \tag{2.6}$$

where A_b is the abundance of Carbon relative to Hydrogen. In this chapter the solar coronal abundances of Feldman et al. (1992) are used; if photospheric abundances (i.e., Grevesse & Sauval, 1998) are used, the C IV line emission will be reduced by 15%. $C(T,n)$ is the contribution function for the C IV line and is obtained from CHIANTI (Dere et al., 1997; Landi et al., 2012) with the ionization equilibrium of Mazzotta et al. (1998). It does not change significantly when the electron density n varies from 10^9 cm^{-3} to 10^{12} cm^{-3}. $\mathrm{DEM}(T) \equiv n^2 \left(\frac{\partial T}{\partial s}\right)^{-1}$ is the transition region DEM, where s measures distance along the flux tube from the base of the transition region. For each flux tube, we assume that the transition region is nearly in static equilibrium in the decay phase when the heating has finished, which is roughly when the coronal density peaks. In this case, thermal conduction is balanced by radiation, and pressure is uniform from the corona through the transition region when gravity is ignored, and the transition region DEM can be calculated as (Fisher, 1987; Hawley & Fisher, 1992):

$$\mathrm{DEM}(T) = P\sqrt{\frac{\kappa_0}{8k_\mathrm{B}^2}}T^{1/2}\zeta^{-1/2}(T) \tag{2.7}$$

where $\zeta(T) = \int_{T_0}^{T} T'^{1/2}\Lambda(T')\,\mathrm{d}T'$, T_0 is the temperature at the base of the transition region, taken to be a nominal 10^4 K, and $\Lambda(T)$ is the optically-thin radiative loss function.

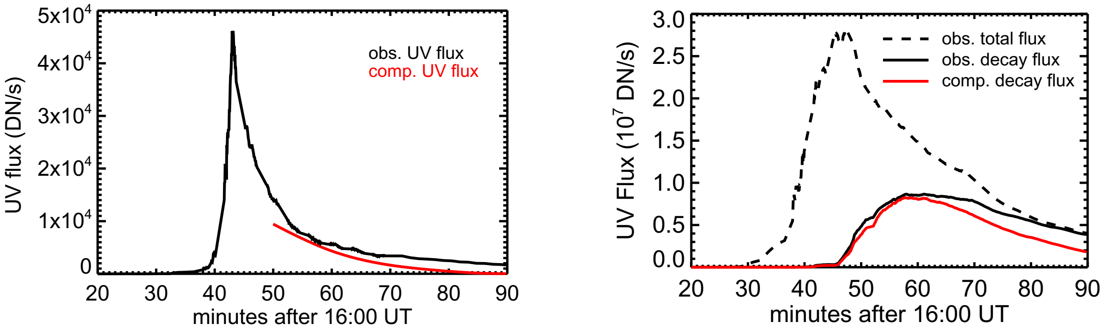

Figure 2.12: Comparison of the synthetic transition region C IV line emissions (red) in the decay phase with the UV flux observed in the *TRACE* 1600 Å band (black) for one flare loop (left) and for all flare loops (right). In the right panel, the observed decay flux is derived by subtracting from the observed light curve the full Gaussian profile that represents the UV rise.

The C IV line emission of one flux tube in its decay phase is calculated with equations (2.6) and (2.7) and convolved with the *TRACE* 1600 Å band response function to get synthetic UV flux in units of DN s^{-1}. The left panel of Figure 2.12

shows an example of the computed C IV line emission in one flux tube. The computed C IV flux appears to evolve along with the observed decay, though the synthetic flux is smaller than the observed by a factor of 2. The right panel of the figure shows the sum of the synthetic UV flux in all flaring pixels in comparison with the observed total UV emission in the decay phase. The observed UV decay in a pixel is obtained by subtracting from the UV light curve the full Gaussian derived by fitting the UV rise so that the transition region response to the heating is excluded. Similar to the single-pixel comparison, the computed total C IV emission decays on the same timescale as observed, and the computed flux is lower than observed by a factor of 2 to 3.

We find this comparison satisfactory for the following reasons. First, the transition region is not exactly in static equilibrium. During the decay phase, the transition region loss usually exceeds the conductive flux, which leads to downflows from the corona, and therefore the coronal density gradually decreases. The downflow is literally an energy input into the transition region and gives rise to a greater transition region DEM than in the case of static equilibrium. Second, the UV continuum in the decay phase may be also enhanced due to irradiation from the C IV line. The observed UV emission is the sum of both the line and continuum emissions, though the continuum intensity is considered to be proportional to the line intensity. All these reasons would explain the observed UV emission being larger than the computed C IV line emission with the static equilibrium assumption. It is, nevertheless, very encouraging to find that the computed line emission decays at the same rate as the observed UV emission. In contrast, the computed X-ray emission decays faster than observed, as shown in the previous Section. Since the UV decay is derived from the same pixels whose rise phase is used to construct the loop heating rate, such comparison indirectly confirms that the rapid decay of the computed SXR flux most likely indicates the presence of additional heating events in the decay phase, which are not found in foot-point UV radiation signatures. This is consistent with decades of observations which have shown that coronal plasma temperatures decrease more slowly than would be expected from simple calculations of radiative and conductive cooling (e.g., Moore et al., 1980; Veronig et al., 2002a,b), implying that additional heating must be taking place despite an apparent lack of accelerated particles. These additional heating events may thus result from continuous reconnection in the corona that provides direct heating without significantly accelerating non-thermal particles, or which accelerates particles sufficiently weakly such that they thermalize in the ambient plasma at the loop-top; both scenarios lead to increased SXR coronal emission without associated chromospheric emission that could be identified in *TRACE* broadband UV or *RHESSI* HXR observations. A similar mechanism has been proposed for the so-called "EUV late phase" emission from eruptive (and often CME-associated) flares (Woods et al., 2011), where reconnection high in the corona heats flare loops, resulting in increased EUV coronal emission without associated foot-point brightenings.

2.5 Discussion and Conclusions

We have analyzed and modeled an M8.0 flare on 2005 May 13 observed by *TRACE*, *RHESSI*, and *GOES*, in order to determine heating rates in a few thousand flare loops formed by reconnection and subsequently heated. The rapid rise of spatially resolved UV emission from the lower atmosphere is considered to be the instantaneous response to heating in the flare loops rooted at the foot points, and therefore is used to construct heating rates in individual flare loops to describe when, for how long, and by how much flare loops are heated (Qiu et al., 2012). With these heating rates, we compute the coronal plasma evolution in these loops using the 0D EBTEL model, and compare, for the first time, the computed time-dependent coronal radiation with observations by *RHESSI* and *GOES*, and as well the computed UV line emission with *TRACE* observations during the decay phase of flare loops. The comparison constrains parameters of the loop heating rates, which define the amount of total energy flux and the fraction of energy flux carried by chromospheric upflows driven by non-thermal beams.

The M8.0 flare studied in this chapter is observed to have significant thick-target HXR emission, suggesting that the lower atmosphere is also heated by electron beams during the impulsive phase. In this process, chromospheric evaporation is driven carrying mass and energy flux back to the corona. In this study, we experimentally scale the beam-driven energy flux with the observed HXR light curve, and examine how varying the fraction of beam heating changes the modeled coronal temperature and density evolution. In general, for a given total amount of heating flux, a larger fraction of energy carried by beam driven upflow leads to higher density, lower temperature, and more rapid evolution of the coronal plasma. These properties affect the computed SXR spectrum and its time evolution, and can be compared against the spectrum observed by *RHESSI*. Our experiment yields an optimal set of parameters, with which, the model computed SXR light curves and spectra agree very well with observations during the rise phase and peak of the flare for more than 10 minutes.

Apart from comparison with the SXR observations, we also compute the C IV line emission at the foot of the flare loop during the decay, whose rise phase is used to construct the heating rate in the same loop. Emission in this optically-thin line during the decay phase is governed by plasma evolution in the overlying coronal loop and contributes significantly to the UV emission observed in the *TRACE* 1600 Å bandpass. It is shown that the computed C IV flux is about one third of the observed UV flux, which also includes the continuum radiation, and decays on the same timescale as observed. This experiment shows an avenue to model heating and cooling of spatially resolved flare loops with self-consistent constraints by high-resolution UV observations from the input (UV rise) to the output (UV decay) in the same flare loop.

These results suggest that our method, which employs all available observations to constrain a flare loop heating model, is able to capture the distribution of impulsive heating rates in numerous flare loops formed and heated sequentially by magnetic reconnection. The optimal heating function parameters determined for this flare yield the peak heating flux in the range of 10^8–10^{10} ergs cm^{-2} s^{-1} for over 5000 flare loops of cross-sectional area 1″ by 1″. Notably, only $\lesssim$40% of this energy is carried by beam-driven upflows during the impulsive phase, with the remaining $\gtrsim$60% contributed by *in situ* heating in the corona. The beam heating occurs mostly during the first ten minutes, when the flare exhibits significant thick-target HXR emission; meanwhile, the *in situ* heating energy in the impulsive phase amounts to 6.2×10^{30} ergs, over 3 times greater than the beam-driven contribution. In the post-impulsive phase (after 16:50 UT), the continuously expanding UV ribbons and the observed Neupert effect between the SXR derivative and UV (rather than HXR) light curves indicate that new flare loops are formed by continuous reconnection, and *in situ* heating in the corona is predominant, amounting to 4.1×10^{30} ergs out of the total, with negligible beam heating. The total energy used in coronal heating in this flare amounts to 1.22×10^{31} ergs, of which the total energy carried by beam-driven upflows is estimated to be only 1.9×10^{30} ergs ($\sim$16%). Therefore, it appears that *in situ* coronal heating and thermal conduction play an important role in the energetics of this M8.0 flare, in contrast to commonly accepted models that consider the coronal thermal plasma to be largely a by-product of beam-driven heating of the lower atmosphere (chromosphere and transition region) (see also discussions by Longcope et al., 2010; Caspi & Lin, 2010; Longcope & Guidoni, 2011). A survey of 37 M- and X-class flares (Caspi et al., 2014a) suggests that *in situ* heating may be significant even down to mid-C class, and therefore this heating mechanism must be considered in future studies of flare energetics.

We note that these energies set lower limits for this M8.0 flare. First, despite the excellent agreement between the model and observation in the rise phase of the flare, the model computed X-ray flux decays more quickly than observed by both *GOES* and *RHESSI*. It is most likely that magnetic reconnection and energy release continue in the high corona during the decay of the flare. These heating events might not produce significant UV foot-point emission, and are therefore not identified in our method. For comparison, Kazachenko et al. (2009, 2012) analyzed the same flare, and estimated the total energy from *GOES* (including energy loss from radiation, conductive cooling and enthalpy flux) to be 3.1×10^{31} ergs. Second, in our experiment, we do not model heating and dynamics of the lower atmosphere, but use a simple scaling relationship to estimate the energy flux carried by non-thermal beam-driven upflows back to the corona. This amount of energy is a fraction of the total energy carried by non-thermal beams; the remainder is lost in the lower atmosphere. As a reference, we fit the HXR spectrum to a power-law distribution with the standard *RHESSI* software package (not shown in this chapter), and, with the low-energy cutoff and spectral index from the fit, estimate the total non-thermal energy to be 7.6×10^{30} ergs, about 4 times the energy carried in the upflow but, interestingly, still somewhat smaller than the energy required to heat the coronal plasma – though we note that the non-thermal energy estimate is only a loose lower bound since it depends critically on the fit low-energy cutoff, which is unbounded from below due to obscuration by the highly-dominant thermal emission.

Our experiment provides a novel method for investigating energy release in solar flares, which is governed by reconnection and substantiated in formation and heating of numerous flare loops. This approach has a few advantages. First, by analyzing the foot-point UV signatures combined with HXR observations, for the first time, we are able to identify and characterize the energy release process in a few thousand flare loops down to $1''$ by $1''$ scale, which is thought to be close to the basic scale of flux tubes formed in patchy reconnection. Using the *same* UV data, we also measure the rate of magnetic reconnection and hence are able to establish the relationship between reconnection and energy release in a temporally and spatially resolved manner. Second, using the 0D EBTEL model, we are able to efficiently compute plasma properties of this large number of flux tubes, and naturally generate a time-dependent differential emission measure (DEM) from these flare loops formed and heated at different times and evolving independent of one another. Subsequently, we can predict X-ray and UV radiation signatures directly comparable with observations, which provides further constraints to our determination of energy release rates.

The method utilizes emission signatures at all available wavelengths in both the foot-points and overlying coronal loops. The dynamics of the lower atmosphere and corona are strongly coupled; they are governed by different yet coherent physics, and hence should be studied coherently. In this study, based on the insight from previous theoretical and numerical research, we employ some empirical laws to prescribe the relation between heating rates and radiation signatures. The optimal parameters obtained from the analysis can provide a reference for further investigation based on physical models, such as models of lower atmosphere heating and dynamics. We also recognize that the 0D EBTEL model has limitations in accurately describing coronal plasma properties along the loop. Nevertheless, the model is highly efficient in dealing with a few thousand flare loops and yields the first-order heating rates as useful inputs for more sophisticated loop heating models such as those by Mariska (1987), Antiochos et al. (1999), or Winter et al. (2011). Our study of this event shows very good agreement between observed and modeled high temperature plasma radiations (e.g., by *RHESSI* and *GOES*), but lacks observations of and therefore comparison with low temperature plasma signatures, which are crucial in understanding the flare loop evolution beyond the conduction-dominant regime. The recently launched *SDO* has observed many flares with AIA, the high-resolution imaging telescope, in a number of UV and EUV bands (Lemen et al., 2012), and as well with the broad-band, high resolution spectrometers on the Extreme Ultraviolet Variability Experiment (EVE; Woods et al., 2012). These new observations, which cover coronal temperatures from $\lesssim$1 MK up to $\sim$20 MK, can be combined with RHESSI observations that provide information of hot ($\gtrsim$10–50 MK) plasmas, as well as information about the non-thermal emission, to fully observationally characterize the temperature distribution and its evolution Caspi et al. (2014b), which can be compared with – and used to constrain – our modeling. These new facilities will allow us to analyze and model flare plasmas following the entire process of heating and cooling, and also to study resolved individual flare loops in multiple wavelengths in more details, which will improve determination of the energy release rate during magnetic reconnection.

Finally, the poor comparison between model and observations during the decay phase of the flare reflects some limitations of the present method. These can be addressed by more sophisticated one-dimensional modeling that also includes the lower atmosphere, to help determine the amount of lower atmosphere radiation, such as the UV 1600 Å emission used in this study, as dependent on the heating mechanism and the amount of heating. Such effort will help clarify whether the shortage of computed flux is produced by the method missing weak heating events, or by other significant effects related to imperfect model assumptions.

We thank Drs. J. Klimchuk and G. Fisher for insightful discussion and the anonymous referee for thoughtful and valuable comments. The work is supported by NSF grant ATM-0748428. A. Caspi was supported by NASA contracts NAS5-98033 and NAS5-02140, and NASA grants NNX08AJ18G and NNX12AH48G. CHIANTI is a collaborative project involving the University of Cambridge (UK), George Mason University, and the University of Michigan (USA).

3. ANALYSES OF FLARE EUV EMISSIONS OBSERVED BY AIA AND EVE

Contribution of Authors and Co-Authors

Manuscript in Chapter 3

Author: Wen-Juan Liu

Contributions: All work except for the ones mentioned below.

Co-Author: Jiong Qiu

Contributions: Helped with study design. Provided scientific advice. Edited drafts of the manuscript.

Manuscript Information Page

Wen-Juan Liu, Jiong Qiu
The Astrophysical Journal
Status of Manuscript:
___Prepared for submission to a peer-reviewed journal
_x_Officially submitted to a peer-reviewed journal
___Accepted by a peer-reviewed journal
___Published in a peer-reviewed journal

Submitted to the Astrophysical Journal March, 2014

ABSTRACT

High resolution ultraviolet (UV) and extreme ultraviolet (EUV) observations have revealed that in a flare a multitude of loops are formed and heated by magnetic reconnection events taking place successively. Spatially resolved observations by AIA and spectrally resolved observations by EVE provide the opportunity to investigate plasma properties and their evolution in these flare loops. In this chapter, we analyze an M1.9 flare observed by AIA in a few bandpasses (AIA 131, 94, 335, and 211 bands) and by EVE in several spectral lines (Fe XXI, Fe XVIII, Fe XVI, Fe XIV). Comparison of AIA and EVE observed light curves of this flare suggests that emissions of these iron lines make significant contributions to the total emission observed by AIA in corresponding channels. EUV emissions from these iron lines reflect evolution of flare plasmas in coronal loops heated to over 10 MK and then cooling down to 2 MK. In addition, AIA images indicate that the flare EUV emissions are produced in both flare loops and their footpoints, and the broad temperature response of the AIA instruments allows detection of plasma emissions at temperatures different from the formation temperatures of the identified iron lines. To estimate the amounts of EUV emissions from flare loops and from flare footpoints, which are likely characterized by different temperatures, we use a recently developed method to model evolution of multiple flare loops and compute the synthetic AIA and EVE light curves. The observed and synthetic light curves reasonably agree with each other in most cases, suggesting that the model has captured the mean properties of flare plasmas. The comparison indicates the presence of the low-temperature component from the flare footpoints in the EUV emission observed by AIA. There is a discrepancy between the synthetic and EVE-observed light curves in the low-temperature iron Fe XIV line at 211.32 Å during the early phase of the flare. We discuss possible reasons and implications of the discrepancy.

3.1 Introduction

Solar flares are impulsive energy release events in the sun's atmosphere. The general picture of the flare is well understood by the standard flare model (the CSHKP model; Carmichael, 1964; Sturrock, 1966; Hirayama, 1974; Kopp & Pneuman, 1976), which states that flare loops are formed by magnetic reconnection in the corona and heated by energy released during reconnection. However, the details of the process are still not very clear. We do not know how much energy is released to heat flare plasmas in flare loops and their footpoints. One dimensional (1D) hydrodynamic simulations have been developed to understand the heating and cooling of a flare as a single magnetic flux tube (or loop) rooted in the chromosphere heated by an ad hoc heating source or non-thermal particle beams (e.g., Nagai, 1980; Somov et al., 1981; Peres et al., 1982; Cheng et al., 1983). These simulations have successfully reproduced the temperature and density enhancement during the flare and are used to predict several X-ray lines, and the ultraviolet (UV) line of Fe XXI at 1354 Å. However, high cadence and high resolution UV and extreme ultraviolet (EUV) observations in the past decade, such as by the *Transition Region and Coronal Explorer* (*TRACE*; Handy et al., 1999), have shown that both the flare arcades and ribbons contain numerous fine structures (e.g., Aschwanden & Alexander, 2001; Fletcher et al., 2004) indicative of hundreds of flare loops formed and heated sequentially. In response to these observations, effort has been made to model evolution of multiple flare loops and reproduce observed radiation signatures by these loops (e.g., Hori et al., 1998; Reeves & Warren, 2002; Warren & Doschek, 2005). For these models to be successful, a critical, yet hard to derive, physical parameter is the heating rate in the flare loop, which understandably varies for different flare loops formed and heated independently of each other.

Recently, Longcope et al. (2010) and Qiu et al. (2012) have proposed two methods to find the heating rates of flare loops using spatially resolved UV light curves in individual flaring pixels, assuming that anchored to these brightened pixels are flare loops that are subsequently brightened in soft X-ray (SXR) and EUV emissions when they are heated and then cool down. Longcope et al. (2010) has used the imaging UV observations combined with the magnetogram to construct the magnetic reconnection configuration and compute reconnection released energy in flare loops as the heating rates. Alternatively, Qiu et al. (2012) interpret the impulsive rise of the footpoint UV light curve as the instantaneous response to flare heating, and therefore infer the heating rate in the flare loop anchored at the footpoint as directly scaled to the rise of the UV light curve. These observationally determined heating rates are then used as energy input terms in a zero-dimensional (0D) Enthalpy-Based Thermal Evolution of Loops model (EBTEL: Klimchuk et al., 2008) to compute coronal plasma properties. The synthetic SXR and EUV light curves are compared with observations to verify the few remaining parameters (the scaling factor between the heating rates and UV count rates, and the ratio of energy loss through the transition region to the coronal radiation) entailed in these methods.

With the second method, Liu et al. (2013) analyzed and modeled an M8.0 flare on 2005 May 13 observed by *TRACE*, the *Reuven Ramaty High Energy Solar Spectroscopic Imager* (*RHESSI*; Lin et al., 2002) , and *GOES*. The UV and hard X-ray (HXR) footpoint emissions are used to construct the heating rates in five thousand loops, and the computed synthetic *RHESSI* SXR spectra and *GOES* SXR light curves agree well with observations for about 15 minutes during the main phase of the flare, suggesting that the model rather successfully produces the high-temperature component of the flare plasmas. Since there are only a few frames of images in EUV (171Å, 195Å and 284Å) for this flare, the entire process of flare plasma evolution from a few tens of million kelvin (MK) to a few MK cannot be verified. Furthermore, the model does not produce sufficient SXR emission as observed in the decay phase of the flare; this is likely due to weak reconnection/heating events taking place in the high corona during the decay phase (Hock et al., 2012), which did not produce strong UV emission at the footpoints. The recently launched *Solar Dynamics Observatory* (*SDO*; Pesnell et al., 2012) with the Atmospheric Imaging Assembly (AIA; Lemen et al., 2012) and Extreme Ultraviolet Variability Experiment (EVE; Woods et al., 2012) provides, for the first time, EUV observations of corona plasmas at temperatures from 1 MK to 10 MK. AIA provides full-disk images of the Sun in several UV and EUV band passes with a pixel size of 0.6 arcsec and 12-second temporal resolution. EVE measures the full-disk solar EUV and SXR spectral irradiance with modest spectral resolution (0.1 nm from 0.1 to 106 nm) and 10-second temporal resolution. The observations by EVE and AIA have been used to study UV/EUV characteristics during flares, for example, the EUV late phase, which is first studied by Woods et al. (2011). The spectra observed by EVE are also useful to study Doppler sensitivity (Hudson, 2011), to diagnose temperature (Del Zanna & Woods, 2013) and density (Milligan et al., 2012) of flares, and to calculate differential emission measure (DEM) of flaring plasma (Warren et al., 2013; Kennedy et al., 2013). The combination of data from

AIA and EVE will help us understand the entire process of heating and cooling of flare plasma in detail never available before.

In this chapter, we analyze an M1.9 flare which occurred on 2011 March 7, as observed by AIA and EVE. Apart from a direct comparison between AIA and EVE observations to infer different temperature components of EUV emissions detected by the broad-band AIA instruments, we also use the method of Qiu et al. (2012) and Liu et al. (2013) to model the flare as composed of numerous flare loops anchored at a few thousand UV brightened pixels. We compute EUV emissions from these loops and their footpoints, and compare the synthetic light curves in several AIA channels as well as a few iron lines observed by EVE characteristic of varying temperatures from 10 to 2 MK. The combined analysis and modeling effort leads to a better understanding of the plasma evolution and the nature of the observed EUV emissions in this flare. The chapter is organized as follows: observations of the flare are presented in Section 3.2, and analysis and modeling methods are described in Section 3.3, followed by results in Section 3.4 and discussion in the last section.

3.2 Observations

3.2.1 Overview of the Flare

In this chapter, we analyze an M1.9 class flare that occurred on 2011 March 7 in active region NOAA AR11166. The flare is associated with a coronal mass ejection (CME), which is studied in detail by Wood et al. (2012). The flare starts at 13:45 UT, when X-ray, EUV, and UV emissions begin to rise as observed by *GOES* and *SDO*/AIA, shown in the flare light curves in Figure 3.1. Light curves in all these bands exhibit a few emission peaks, indicating multiple stages of energy release in this flare. In general, light curves in the UV 1600 Å band tend to peak first, followed by X-ray (*GOES* 1-8 Å) and EUV (AIA 131 Å and 94 Å) emissions from relatively high temperature plasmas, and then by EUV emissions from lower-temperature plasmas (AIA 211Å, 193Å, and 171Å). This sequence of emissions is consistent with the traditional picture of flare evolution. The early-phase emission in the UV 1600 Å band is produced in the lower-atmosphere, the transition region and/or upper-chromosphere, which is heated by flare energy release along flare loops formed by reconnection. The flare loops are subsequently brightened when the loops are filled with hot plasmas evaporated from the chromosphere and then cool down to the temperatures of these AIA EUV channels.

This scenario is confirmed by morphology evolution of the flare shown in images in Figure 3.2. The figure shows that the flare footpoints (or ribbons) are brightened in UV 1600 Å band at the beginning of the flare, followed by EUV emissions in flare loops that appear to connect the footpoints. It is noted that, at the beginning of the flare, the flare footpoints also brightened in all AIA EUV channels simultaneously with the UV emission – see the example of 211 Å image as well as 131 Å image in the early phase of the flare in Figure 3.2. These footpoint EUV emissions account for the early rise in these bands shown in Figure 1. Since each of the AIA EUV channels has

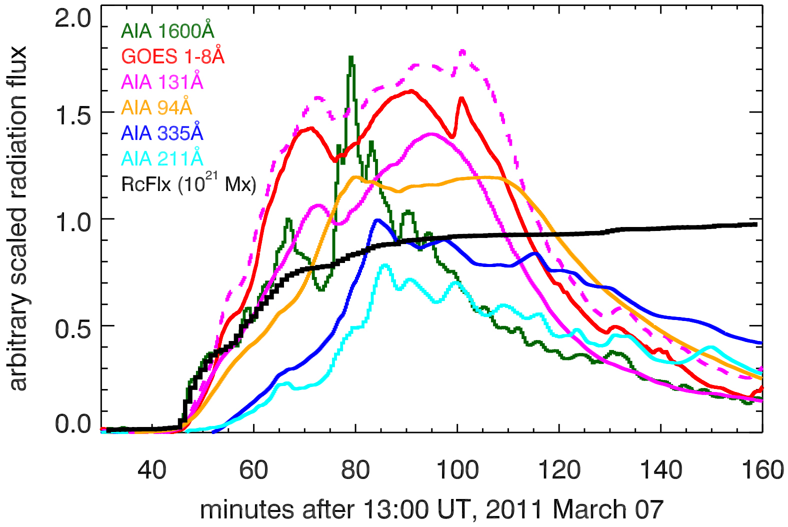

Figure 3.1: Background-subtracted and arbitrary scaled light curves of the 2011 March 07 flare in 1600 Å (dark green), 131 Å (magenta, solid line), 94 Å (orange), 335 Å (blue) and 211 Å(cyan) channels observed by *SDO*/AIA, full disk SXR (1–8 Å red) radiation observed by *GOES*, and reconnection fluxes (black) measured from *SDO*/HMI longitudinal magnetogram and UV 1600 Å images. The light curve in 131 Å from full-disk is also plotted in the figure in magenta dashed line with the same scalar as light curve in 131 Å from the flare.

a broad temperature response function that includes a substantial contribution from low-temperature plasmas (Boerner et al., 2012), these early phase EUV emissions are likely produced by the same mechanism that generates the UV emission: they are all emitted from the lower-atmosphere heated by impulsive energy deposit.

The images and light curves also indicate multiple stages of energy release in the flare. It is noted that the time between the second EUV peak and UV peak is much longer than that between the first peaks, suggesting a longer cooling time during the second stage of energy release. UV and EUV images show that these different emission peaks are produced in two different sets of loops. Footpoints of the first set of loops were brightened before 14:13:31 UT, and flare loops appear to

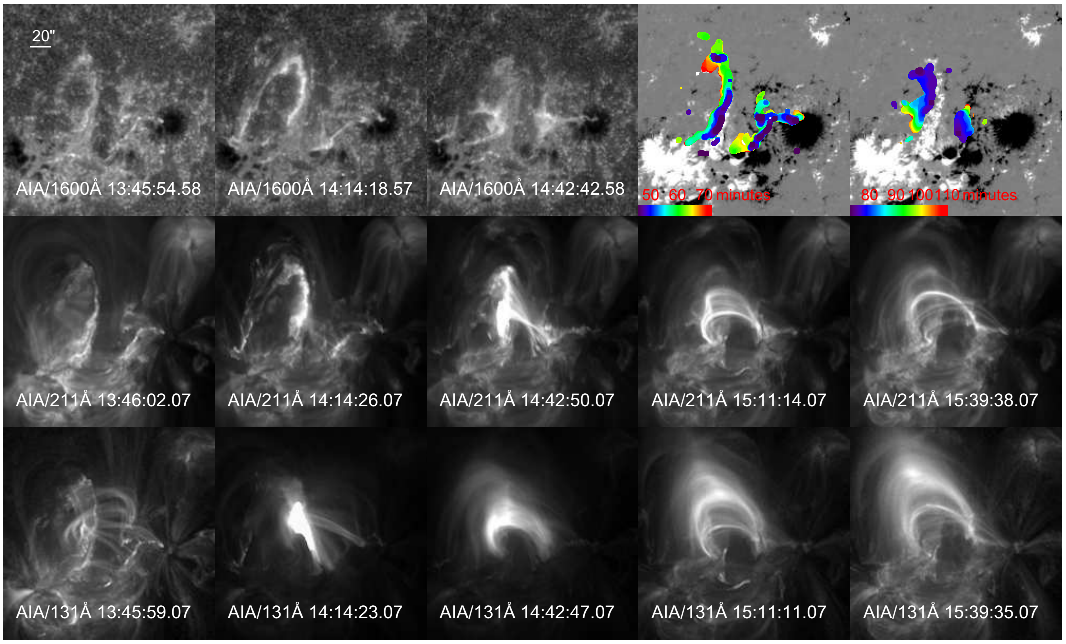

Figure 3.2: Snapshots of the 2011 March 07 flare in UV 1600 Å and spreading of footpoints overlaid on HMI line-of-sight magnetograms (upper panel), and snapshots in EUV 211 Å (middle panel) and 131 Å (lower panel) channels observed by *SDO*/AIA.

rotate along the polarity inversion line (PIL). The second set of loops were heated after 14:13:31 UT; their footpoints (ribbons) appear to move perpendicular to and away from the PIL, and the loops were subsequently formed at growing height with increasing loop length. Examples of these loops in AIA 131 Å are shown in the lower panel of Figure 3.2, and the spreading of footpoints where these two groups of loops are anchored are presented in the upper panel, with colors indicating the time when these footpoints begin to brighten. From evolution of these footpoints and the line-of-sight magnetogram obtained by Helioseismic and Magnetic Imager (HMI; Scherrer et al., 2012), we can measure magnetic reconnection flux (Qiu et al., 2002; Longcope et al., 2007), as plotted in Figure 3.1. The plot shows the two stages of magnetic reconnection forming two groups of flare loops in this active region.

3.2.2 AIA and EVE Observations

In this chapter, we study heating and evolution of flare plasmas in reconnection formed flare loops. Both imaging observations by AIA and spectroscopic observations by EVE will be analyzed to provide more detailed diagnostics of flare evolution. EUV emissions obtained by EVE in a few lines will be studied for more precise diagnostics of the flare plasma temperature. In particular, we focus on the AIA EUV channels of 131 Å, 94 Å 335 Å and 211 Å, and the EVE lines that dominate these AIA channels during the flare. It is well known that each of the AIA channel has a broad response function that includes contributions by multiple EUV lines formed at different temperatures. For the AIA-EVE cross comparison, it is important to identify EVE lines that dominantly contribute to an AIA channel during the flare evolution. The upper panel of Figure 3.3 displays the EVE-observed full-disk spectra in wavelength ranges of the four AIA channels, overplotted with the corresponding AIA response functions (effective areas) obtained from the *SolarSoftWare IDL* (Freeland & Handy, 1998). The EVE spectra plotted in different colors from black to red indicate evolution of the spectra during the flare. The figure illustrates spectral features that make dominant contributions to the AIA channels during the flare. According to O'Dwyer et al. (2010), the Fe XXI, Fe XVIII, Fe XVI and Fe XIV lines primarily contributes to the AIA channels of 131 Å, 94 Å, 335 Å, and 211 Å, respectively.

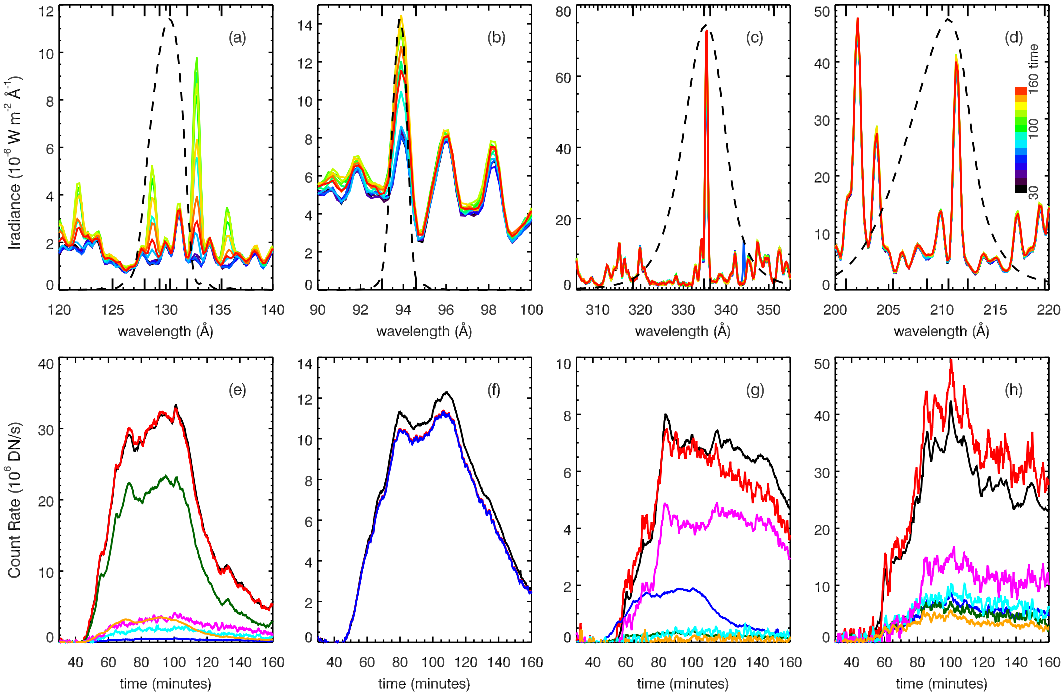

Figure 3.3: Upper: solar spectra observed by *SDO*/EVE for four *SDO*/AIA channels ((a) AIA/131 Å, (b) AIA/94 Å, (c) AIA/335 Å, and (d) AIA/211 Å) with colors indicating the time of observations. The arbitrarily scaled effective areas of these AIA EUV channels are overplotted in dashed lines. Lower: predicted light curves in four AIA channels (in units of DN/s) by convolving the EVE-observed irradiance spectrum in different wavelength ranges (different colors; the wavelength ranges are also indicated by tick marks in the upper panel) with AIA wavelength response functions in comparison with the total counts light curves observed by AIA (black). (e) AIA/131 Å, Red (EVE full spectra), blue ([125.0 Å, 128.0 Å]), dark green ([128.0 Å, 129.4 Å]), cyan([129.4 Å, 130.4 Å]), magenta([130.4 Å, 132.0 Å]), orange([132.0 Å, 135.2 Å]). (f) AIA/94 Å, Red (EVE full spectra), blue([93.0 Å, 94.6 Å]). (g) AIA/335 Å, Red (EVE full spectra), blue ([128.0 Å, 135.2 Å]), darkgreen ([135.2 Å, 318.0 Å]), cyan([318.0 Å, 334.8 Å]), magenta([334.8 Å, 336.2 Å]), orange([336.2 Å, 351.2 Å]). (h): AIA/211AA, Red (EVE full spectra), blue ([201.0 Å, 205.4 Å]), dark green ([205.4 Å, 208.6 Å]), cyan([208.6 Å, 210.6 Å]), magenta([210.6 Å, 212.4 Å]), orange([212.4 Å, 219.6 Å])

For example, the AIA/131 Å channel was designed to center on Fe XXI at 128.75 Å line and the Fe VIII pair at 130.94 Å and 131.24 Å (Lemen et al., 2012). O'Dwyer et al. (2010) calculated dominant contributions to each AIA channel by using a prescribed differential emission measure (DEM) reconstructed from the observations of the decay phase of an M2.0 flare (Dere & Cook, 1979) and the CHIANTI (Dere et al., 1997, 2009) atomic data. Their calculation predicted that the 131 Å channel is dominated by the Fe XXI at 128.75 Å for the flare spectrum. To assess the contributions of these lines to the AIA 131 Å channel observed in this flare, we convolve different parts of the EVE spectrum with the wavelength response function of AIA/131 Å channel (in units of cm^2 DN photon^{-1}) to make predicted AIA light curves from different parts of the EUV spectrum, as shown in different colors (dark green, cyan, magenta, and orange) in Figure 3.3(e). In comparison, the observed AIA 131 light curve and the predicted AIA 131 light curve from the entire EVE-observed EUV spectrum are also plotted in dark and red colors, respectively. The figure shows that the Fe XXI line emission (dark green) contributes more than 60% of the full-disk AIA/131 emissions, dominating the AIA 131 Å channel. Contributions from other lines to the AIA/131 channel are also plotted in Figure 3.3(e), which shows that the O VI (cyan), Fe VIII (magenta) and Fe XXIII (orange) lines each contributes about 10% of the total AIA/131 emission. The Fe XXIII line is formed at a high temperature of 10 MK, and the O VI and Fe VIII lines are formed at 300,000-400,000K. Therefore, emission in the AIA 131 Å channel is primarily emitted by 10 MK plasmas during the flare, with about 20% contribution by low-temperature plasmas of below 1 MK.

In the same way, we distinguish the spectral contributions to the other three AIA channels by plotting the light curves of different parts of the EVE spectrum convolved with the AIA response functions in Figure 3.3(f)–(h). The AIA/94 Å is dominated by the spectral feature at 93.0–94.6 Å (blue; Figure 3.3(f)), which makes over 90% of the total emission throughout the flare. The Fe XVIII at 93.93 Å formed at 6 MK is the major contributor in this spectral range (O'Dwyer et al., 2010), though this line could be blended with Fe XX and Fe X which cannot be distinguished from Fe XVIII line with the resolution of the EVE spectrometer. Warren et al. (2012) proposed that in solar active regions the contribution of warm emission to the AIA 94Å channel could be estimated empirically by a combination of AIA 171Å and 193Å images. For AIA/335 Å (Figure 3.3(g)), in the first 50 minutes of the flare, about 30% of total counts comes from the spectral range of 128.0–135.2 Å (blue), where there is a secondary peak in the response function of AIA/335 Å. Emission in this spectral range is also observed by the AIA/131 Å. Therefore, the early phase light curve of this component is quite similar to the AIA/131 Å light curve. The rest of the emission in this channel is mostly by the Fe XVI line (magenta) that contributes more than 50% during the early phase. Afterwards, the Fe XVI line dominates the AIA/335 Å channel contributing by 70–90%. For AIA/211 Å (Figure 3.3(h)), Fe XIV line (magenta) makes up about 30% of the total observed counts, and the rest is by the nearby spectra from 201 through 220 Å.

In comparison, predictions by O'Dwyer et al. (2010) show that the Fe XXI, Fe XVIII, Fe XVI and Fe XIV lines contribute to 83%, 85%, 81%, and 11% to the total emission in the AIA 131, 94, 335, and 211 bands, respectively. The prediction is comparable with the observed fractional contributions by these lines during the late phase of the flare, which amounts to >60%, >90%, >70%, and ∼30% respectively. During the early phase of the flare, other spectral features also make significant contributions to the AIA 335 and 211 bands.

Table 3.1: AIA channels studied in this chapter and the corresponding EVE lines which contribute most to the AIA channels during the flare.

AIA channel	Ion	λ(Å)	$\log(T_{max})$
131	Fe XXI	128.75	7.1
94	Fe XVIII	93.93	6.9
335	Fe XVI	335.41	6.5
211	Fe XIV	211.32	6.3

Notes. T_{max} (in logarithm) is the approximate temperature of formation of the ion in equilibrium.

The analysis confirms that the Fe XXI, Fe XVIII, Fe XVI and Fe XIV lines observed by EVE contribute significantly to AIA 131 Å, AIA 94 Å, 335 Å, and 211 Å channels, respectively. The details of these lines are given in Table 3.1. Figure 3.4 further shows the instrument response functions of these AIA channels and the corresponding EVE spectral line contribution functions. The temperature response functions of the AIA channels are obtained by using the aia_get_response function distributed in *SolarSoftWare IDL*. The contribution functions are calculated by using CHIANTI v7.1.3 atomic data (Dere et al., 1997; Landi et al., 2013) with the ionization equation equilibrium of Mazzotta et al. (1998), the coronal abundance of Feldman et al. (1992)

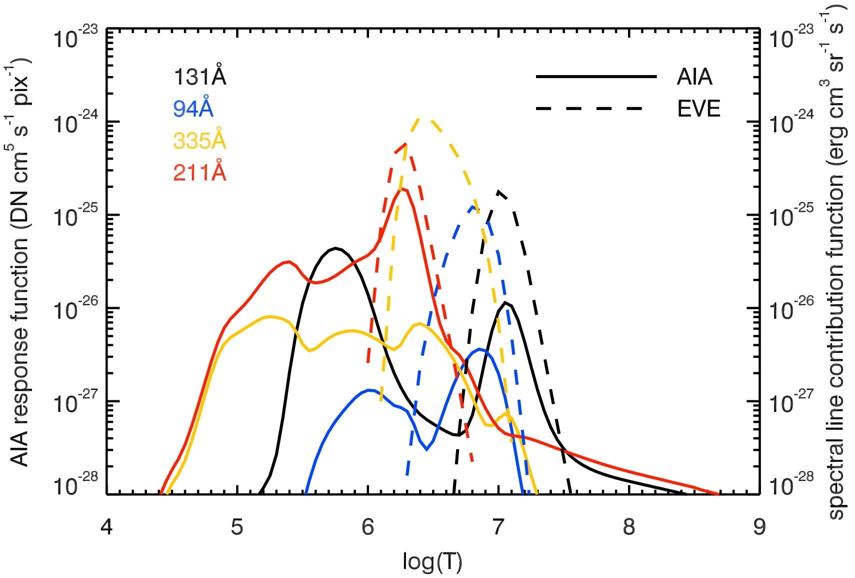

Figure 3.4: Temperature response functions of four AIA channels (solid lines) and spectral contribution functions for four EVE lines (dashed lines) that dominate these AIA channels during the flare.

and electron density of 10^{10} cm^{-3}. The quoted peak temperature of these lines/channels is 10 MK, 6 MK, 3 MK, and 2 MK, respectively; therefore, these lines/channels allow us to follow evolution of flare plasmas that are heated to over 10 MK and then cool down to a few MK.

We also find that the observed full-disk total counts rate light curves in AIA EUV channels are nearly identical to those predicted by convolving EVE spectra with AIA wavelength response functions. The ratio between the two light curves is 0.97, 0.81, 0.91, and 0.80 for 131, 94, 335, and 211, respectively.

3.2.3 Effect of Flares in Other Active Regions

Like *GOES*, EVE obtains EUV spectra and light curves from the entire solar disk, and contributions from other flares that possibly occur on the disk during this

M1.9 flare should be excluded. The full-disk UV and EUV images (not shown in this chapter) indicate that, in the early phase of the M1.9 flare studied in this chapter, a small and very short-lived flare in active region AR11164 about $1000''$ west of the M1.9 flare occurred at 13:52 UT and lasted for about 25 minutes in 171 Å; in the late phase of the M1.9 flare, another short-lived flare in active region AR11165 about $1200''$ in the west of the M1.9 flare occurred at 14:38 UT and lasted for about 35 minutes in 171 Å. These other flares at different locations may account for the early enhancement and the significant third peak in the full-disk *GOES* SXR light curve plotted in Figure 3.1.

The contributions to SXR and EUV emissions by these other flares may be estimated by comparing the full-disk AIA 131 Å light curve with the 131 Å light curve obtained for only the active region hosting the M1.9 flare studied in this chapter. Shown in Figure 3.1, the full-disk AIA 131 Å light curve exhibits more enhanced emission in the early phase of the target flare as well as a significant third emission peak at 14:41 UT, which is not present in the M1.9 flare light curve. These additional features reflect the contributions by the other two flares. In fact, the full-disk 131 Å light curve matches very well the *GOES* SXR light curve, as also reported in a recent study showing that the normalized AIA 131 Å light curve tracks the normalized *GOES* 1–8 Å light curve very closely during the flare rise phase (Fletcher et al., 2013). Therefore, the early enhancement and the significant third peak in the full-disk *GOES* SXR light curve must come from hot plasmas by the other flares in the other active regions. Since it is not easy to remove these additional contributions to the SXR emission, in this study, we do not analyze *GOES* light curves. We also note that *RHESSI* observation is available for a short period in the early phase of the flare from 13:51 UT–14:13 UT as well as in the late decay phase from 14:40 UT–15:15 UT. However, in the early phase, *RHESSI* images (not shown in the chapter) indicate that most of the soft X-ray emission (3–25 keV) and possibly all hard X-ray emission (> 25 keV) come from the flare in the active region NOAA AR11164 in the west; and in the late phase, soft X-ray emission observed by *RHESSI* comes from yet another flare in the active region near the western limb. Therefore, we do not analyze *RHESSI* observations in this chapter.

Although EVE also observes the entire disk like *GOES* does, we attempt to estimate EUV emission from the target flare by comparing EVE light curves in a few lines that primarily contribute to relevant AIA channels. To remove the contamination from the other two flares, we use the ratio of the AIA light curve from the target active region to that from the full-disk to roughly derive the EVE-observed iron line emissions by the studied M1.9 flare. This simple method of scaling the EVE and AIA light curves depends on the assumptions that emissions from different flares contribute to the AIA and EVE total emission in a similar manner, and that emissions observed in the AIA channels are dominantly from the lines identified above. However, AIA is a broadband imager that may include contributions of other unidentified spectral features in various stages of the flare. To further discuss these effects, in the following analysis, we will use a simple loop heating model to compute plasma properties in flare loops, with which we synthesize the light curves of iron lines observed by EVE as well as light curves observed by AIA.

3.3 Modeling Evolution of Multiple Flare Loops

It is evident in the AIA images that the flare is comprised of numerous flare loops that are formed, heated, and then evolve independently of one another. The total emission in EUV wavelengths at any given time is the sum of emissions by these individual loops with different temperatures and densities during different evolution stages. To understand how this process results in EUV emissions observed by AIA and EVE, we apply a recently developed method to model evolution of multiple loops and then compute EUV emissions by these loops to compare with observations.

The details of the method are given in Qiu et al. (2012) and Liu et al. (2013). In short, this method assumes that the heating rate of a flare loop is proportional to the impulsive rise of the UV 1600 Å light curve observed at the footpoint of the loop. Therefore, analyzing spatially resolved UV light curves provides heating rates (time, duration, and magnitude) of many flare loops anchored at the UV footpoints brightened during the flare. With these heating rates, the time evolution of the mean temperature and density of each of these flare loops can be computed with a zero-dimensional EBTEL model (Klimchuk et al., 2008). The model solves two time-dependent equations. The energy equation is governed by heating rate and coronal radiative loss as well as the loss through the transition region. The mass equation addresses relationship between thermal conduction, transition-region loss, and enthalpy flow between corona and the lower-atmosphere through the transition region. In modeling this flare, we assume that heating primarily takes place in the corona. Non-thermal particle effects are neglected for lacking evidence of thick-target non-thermal emission in this event. *RHESSI* light curves exhibit an impulsive rise in the early phase of the flare in photon energies greater than 25 keV; however, in *RHESSI* images, the source of this possible non-thermal component occurs in a different active region. Therefore, we consider the M1.9 flare primarily a thermal flare with negligible non-thermal effects. Only two free parameters are used in modeling all flare loops, which will be further discussed in the following text.

3.3.1 Evolution of One Loop

An example of the computed evolution of one flare loop is shown in Figure 3.5. The loop with half length of 51 Mm and cross sectional area of $1''$ by $1''$ is heated by a Gaussian shaped impulsive heating function with the maximum heating rate of 1.5×10^9 ergs s^{-1} cm^{-2} and heating duration of 6 minutes (see the UV light curve and scaled heating rate in panel (b) of Figure 3.5). A continuous constant background heating rate of 10^6 ergs s^{-1} cm^{-2} is also included, which maintains the pre-flare plasma temperature at 1.9 MK before the impulsive flare heating is switched on. The evolution of the mean temperature (solid line) and density (dash line) calculated by EBTEL are plotted in panel (a). The temperature rises immediately when the loop

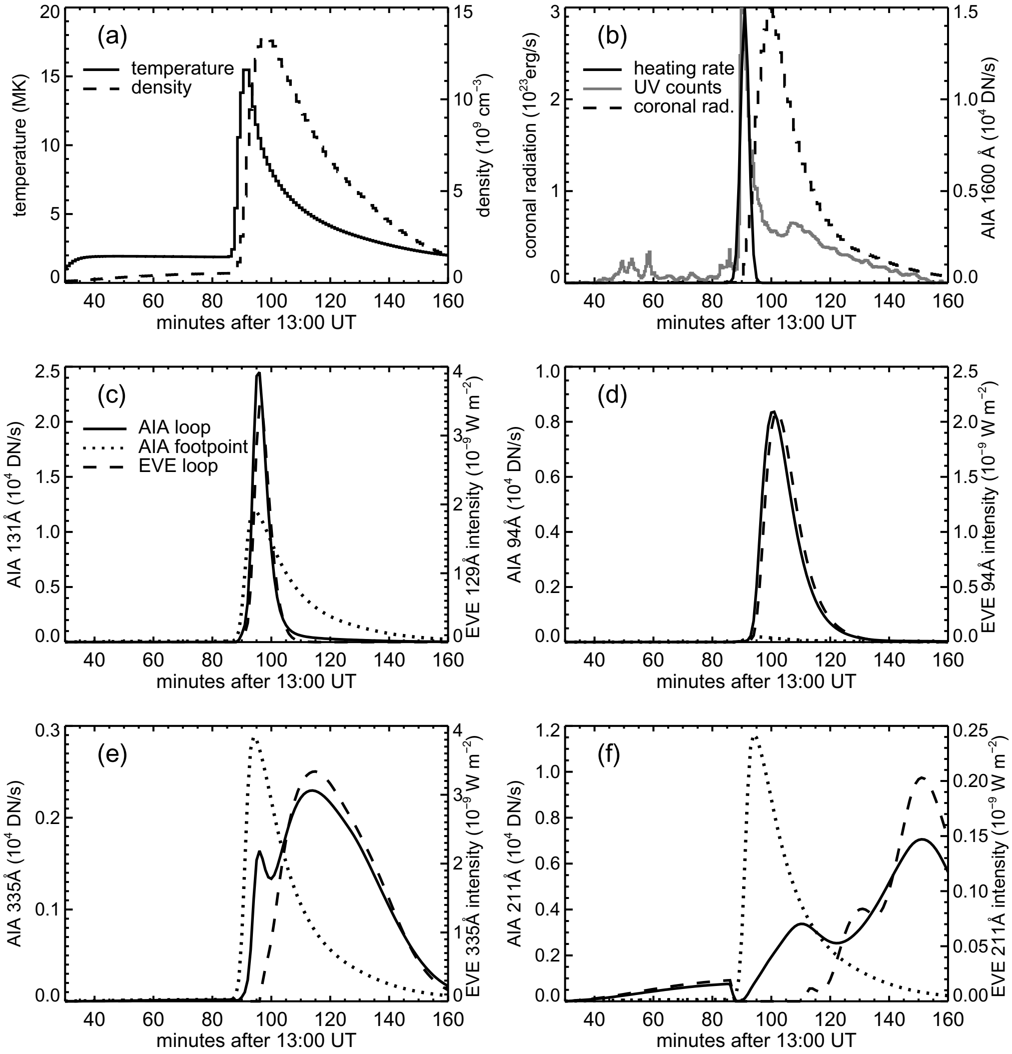

Figure 3.5: Computed evolution of one flare loop with cross-section 1 ″ × 1 ″ and the synthetic light curves of the loop observed by AIA and EVE. (a) Time profile of averaged coronal density (dashed line) and temperature (solid line) of the loop. (b) Observed UV 1600 Å count rate (grey line), scaled heating rate (solid black line) and the computed coronal radiation of the loop. (c)-(f) Synthetic light curves of the loop in AIA 131 Å, 94 Å, 335 Å and 211 Å (solid lines), the intensities of EUV lines contributed most to these channels (long dashed lines) and synthetic light curves of the footpoint where the loop anchored (dotted lines).

in the corona is heated, and peaks at the time when the heating rate is maximum. The density rises later when the energy is transported to the base of the loop by conduction flux from the corona, which increases the local pressure to drive plasmas up into the coronal loop. As the loop cools down, the coronal plasma density starts to decrease, when at the base of the loop the energy loss is greater than the energy gain from thermal conduction, and coronal loop is drained by downward enthalpy flux.

Coronal radiative losses increase when the temperature and density increase, and peak at the density peak (see the dashed line in panel (b)). In order to compare the model results with observations, we also plot the predicted synthetic AIA light curves (solid lines) and synthetic EUV line intensities (long dashed lines) by a single loop in panel (c)–(f) of Figure 3.5. The AIA synthetic light curves of a single loop are computed using the average temperature and density of the loop and the instrument response functions. The synthetic EUV line intensities are calculated using the contribution function of the line obtained from the CHIANTI atomic data. Note that for a single loop computed with EBTEL, at any given time, the loop is assumed to be isothermal.

Figure 3.5 shows that the light curve in Fe XXI line rises and peaks first, followed by Fe XVIII, Fe XVI and Fe XIV. The sequence of the rise and peak in these light curves displays the cooling of plasma in the loop from 10 MK to 2 MK. Figure 3.5 shows that the synthetic light curves of the loop in AIA 131 Å and 94 Å channels are quite similar to the intensities of the iron lines, indicating that these high temperature AIA channels are mostly dominated by the identified iron lines during the flare. Light curves of AIA/335 Å and AIA/211 Å are also similar to the corresponding iron lines, but both exhibit enhanced emission in the early phase of heating not present in the EVE lines, indicative of the contribution to the AIA channels by other sources due to the broad temperature response functions of the AIA bands. For example, the early impulsive peak at 14:35 UT in the AIA/335 Å channel coincident with the 131 emission is due to contribution by 10 MK plasmas, and the enhanced emission in AIA 211 channel is likely produced by plasmas at temperatures higher than 2 MK.

Apart from emission by plasmas in coronal loops that cool from 10 MK to 2 MK, it is also recognized that AIA response functions include substantial contribution by plasmas at much lower temperatures, typically below 1 MK. The EUV images shows that all AIA EUV channels observed footpoint emission in the early phase of the flare. These footpoint emissions are very likely produced in the transition region heated during the flare. The amount of the emission may be estimated by assuming that, as soon as the impulsive heating stops, the transition region quickly reaches equilibrium with the corona, so that the differential emission measure ($n^2 ds/dT$) of the optically thin transition region is calculated to be directly proportional to the coronal pressure (Fisher, 1987; Griffiths et al., 1998; Hawley et al., 2003). With the calculated transition region DEM, the synthetic EUV light curves at the footpoint can be derived. Studying a different flare, Qiu et al. (2013) have shown that such an approximation agrees with AIA observed footpoint EUV emissions by within half an order of magnitude. In this study, we also calculate the footpoint EUV light curves, and plot them in dotted lines in panel (c)–(f) of Figure 3.5. In the calculation, we convolve the DEM from 0.1–1 MK with the AIA temperature response functions to estimate footpoint emission observed by AIA. Figure 3.5 shows that the light curves from the footpoint in all AIA channels are similar, which is not a surprise, because by pressure-gauge assumption they are all proportional to the coronal pressure. The footpoint emission, if integrated to 1 MK, appears to contribute significantly to many AIA channels, except the AIA/94 Å channel because its quoted response function at temperature below 1 MK is not prominent compared with its peak response at $\log_{10} T = 6.85$.

The EUV emission by lower-temperature plasmas at the footpoint is not shown for the EVE lines, because contribution by <1 MK plasmas to the narrow bandpass of these iron lines is rather trivial (see spectral contribution functions of these lines plotted in Figure 3.4).

In summary, the experiment with a single loop suggests that the synthetic coronal radiation should appear very similar in the few AIA bands and their corresponding EVE lines. On the other hand, AIA instruments have broad temperature responses, and are therefore expected to capture more features, such as the footpoint emission by lower temperature plasmas, than EVE lines. It is also noted that the above experiment only provides a qualitative reference because of the limitation of the underlying isothermal assumption in the 0D EBTEL model. Nevertheless, the advantage of using EBTEL lies in its capability to efficiently model evolution of a few thousand flare loops, which yields a distribution of flare plasma properties in these loops and therefore allows us to synthesize the spatially integrated total emissions in given bands or lines observed by AIA and EVE. This is demonstrated in the following section. We expect that the along-the-loop distribution of plasma properties may become much less significant when we take into account gross properties of many loops.

3.3.2 Mean Properties of All Flare Loops

In this study, we use EBTEL code to model a few thousand flare loops. To be precise, we do not identify each of these loops one by one in EUV images; instead, we assume that each of the UV-brightened pixels is the footpoint of a half loop. A full loop has two conjugate footpoints in magnetic field of opposite polarities. Since it is difficult to identify connectivities between UV pixels, we consider that each UV pixel is connected to a half loop. In this flare, we have identified more than 3000 UV-brightened pixels and therefore modeled more than 3000 half loops. The length of the half loop L is obtained by measuring the distance from the UV footpoint to the polarity inversion line (PIL), with the assumption that a flare loop is a half circle. In general, a loop with a greater length will evolve more slowly after the heating phase; our experiments show that, increasing the loop length by up to 20% does not significantly modify the synthetic light curves by all loops. For the first group of loops brightened before 14:13:31 UT, the L is a constant 44Mm as judged from evolution of flare morphology; and for the second group of loops, L grows linearly from 44Mm to 78Mm with the increasing footpoint distance from the PIL. A free parameter is used to scale the heating rate (erg s^{-1}) to the rise of UV light curve

(DN s^{-1}). It is determined by comparing the amounts of synthetic and observed EUV emission by relatively high temperature plasmas (Qiu et al., 2012). The other parameter that scales the transition region loss to the coronal radiative loss is best determined by comparing observed and synthetic EUV emissions at low-temperatures (Qiu et al., 2012). For this flare, the heating rates in flare loops range from 4.2×10^8 to 5.1×10^{10} ergs s^{-1} cm^{-2}, and the mean energy loss rate through the transition region is found be about 3.5 times the coronal radiative loss.

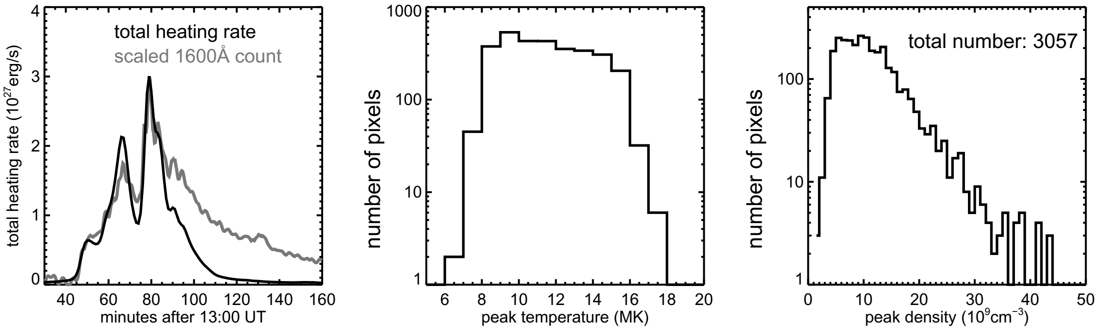

Figure 3.6: Left: the sum of the total heating rate (black line) in comparison with the observed total UV light curves (gray line). Middle and right: peak temperature and density distributions in over 3000 modeled flare loops with lengths in the range of 40–78 Mm and cross-sectional area of 1″ by 1″.

The total heating rate in all the loops is plotted in the left panel of Figure 3.6. It resembles the rise and peaks of the observed UV light curve, while the decay of the UV light curve is considered to reflect cooling of the loops, which we will study in Section 3.4. The total amount of heating energy is 4.5×10^{30} ergs, which is about a third of the heating energy in the M8.0 flare on 2005 May 13 studied by Liu et al. (2013). Also plotted in Figure 3.6 are the histograms of peak temperature and density of all the loops. The peak temperature ranges between 8–16 MK, and the peak density between 5–15 × 10^9 cm^{-3}.

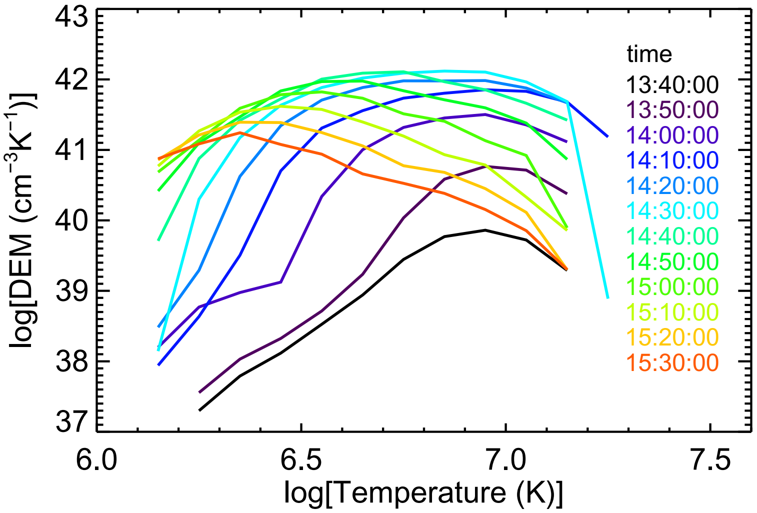

Figure 3.7: Time evolution of the coronal DEM from the model for the M1.9 flare on 2011 March 11 from 13:40 UT to 15:30 UT.

The differential emission measure (n^2dV/dT) of the flare plasmas is calculated with the temperatures and densities of over 3000 half loops. Figure 3.7 shows the evolution of the flare DEM averaged over every 1 minute. The DEM starts to rise at high temperature when a few loops are heated at the beginning of the flare. And the DEM continues to increase at high temperature when more and more loops are heated. After the flare peak time, the DEM at low temperature rises and at high temperature decreases showing the cooling of plasma in the loops. The DEM is then convolved with AIA instrument response functions or spectral line contribution functions to yield synthetic light curves of the flare in different EUV channels to compare with observations in the next section.

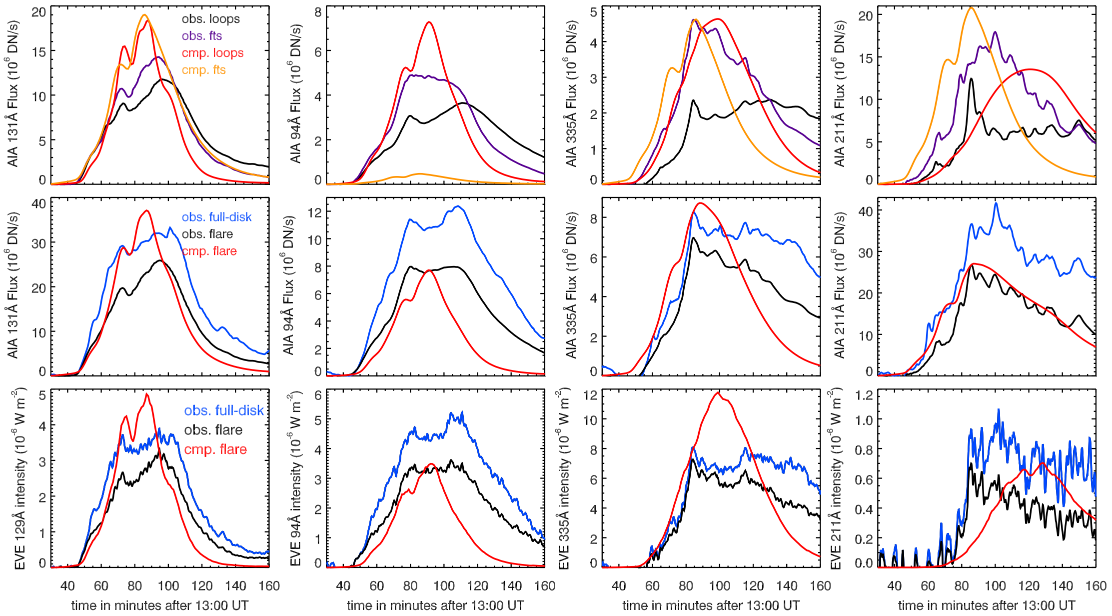

Figure 3.8: Top Panel: comparison of the synthetic light curves from loops (red) and footpoints (orange) in four AIA EUV channels (131 Å, 94 Å, 335 Å, and 211 Å) with observed light curves from loops (black) and footpoints (purple). Middle panel: comparison of the synthetic light curves from the flare (red) in these four AIA EUV channels with observations (black). Bottom panel: comparison of the synthetic line intensities in four iron lines Fe XXI line at 128.75 Å Fe XVIII line at 93.93 Å, Fe XVI line at 335.41 Å, and Fe XIV line at 211.32 Å (red) with EVE-observed line emissions from the flare (black) which are estimated by scaling EVE light curves with AIA light curves. For reference, the pre-flare subtracted full-disk light curves observed AIA and iron line emissions observed by EVE are overplotted in blue in the middle and bottom panels, respectively.

3.4 Comparison of Synthetic EUV and UV Emissions with Observations

In Figure 3.8, we compare the synthetic EUV light curves of the flare with observed light curves by AIA (top and middle panels) and EVE (bottom panels). For the synthetic AIA light curves, emissions from both flare loops and footpoints are considered, as suggested by the AIA images. The synthetic light curves from the loops are calculated by convolving the DEM (n^2dV/dT, where $V = \Sigma_{i=1,N}L_iA_i$, with

L being the half-loop length, and A the cross-sectional area) derived from all loops with the AIA temperature response functions. The synthetic light curve from one footpoint is estimated by convolving the transition region DEM ($n^2 ds/dT$) of the footpoint with the AIA response function up to a nominal maximum temperature of $\log_{10} T = 6.0$, and light curves from all the footpoints are summed up. The so calculated emissions from the loops and from the footpoints are displayed in red and orange, respectively, in the top panel. In this same panel, the AIA observed footpoint light curves are also displayed in violet. The observed footpoint emission is estimated by summing the counts *only* from the pixels that are brightened in the UV 1600 Å images, and the loop emission shown in black is estimated by subtracting this footpoint emission from the total emission in the active region. We observe that, during the flare, footpoints brighten first in most AIA channels. Soon afterwards, later formed coronal loops are brightened and overlap the footpoint pixels that have brightened earlier, so emission from the footpoint pixels during the later phase is a mixture of emissions from both the footpoints and overlying coronal loops. For this reason, the observed "footpoint" emission displayed in the top panel represents an upper-limit of real footpoint emissions, and the observed "loop" emission displayed in the top panel is hence the lower-limit of the emission from coronal loops. In the middle panel, the calculated total emission, which is the sum of the footpoint and loop emissions, is plotted in red in comparison with the observed total flare emission plotted in black.

The bottom panels show, in red, synthetic light curves of the four iron lines observed by EVE. The synthetic EUV line intensities are calculated by convolving the DEM (n^2dV/dT) of all loops with the spectral contribution function of these iron lines provided by the CHIANTI atomic data. Since there is no contribution to these lines from temperatures below 1 MK, the footpoint emission is neglected. We compare the synthetic line emissions with the EVE observations. The observed line intensity is obtained by integrating the spectrum over the wavelength range between the two closest local minima on both sides of the line center. Then we subtract the continuum intensity which is assumed to be the lowest intensity in a wavelength range of 10 Å around the line center (Warren et al., 2013). An averaged pre-flare intensity is also subtracted to retain the flare emission. This method yields the width of the Fe XXI line to be 1.4 Å during the main phase and 1.0 Å after 15:10 UT. Uncertainty of the line intensity obtained from this integral is mainly caused by the blending of nearby spectral lines, which is estimated to be up to 20% during the flare. In the bottom panels, the blue curves show the EVE observed line emission of the entire disk, and the black curves show the roughly estimated line emissions by the M1.9 flare by scaling the EVE light curves to the AIA light curves as described earlier.

The overall similarity between observed AIA light curves (middle panels) and EVE light curves (bottom panels) tends to suggest that the identified EUV lines may dominantly contribute to the AIA channels. The nominal formation temperature of these lines is 10, 6, 3, and 2 MK, respectively, therefore plasmas emitting at these temperatures likely dominate the AIA 131, 94, 335, and 211 channels, respectively. On the other hand, comparison of the synthetic and observed EUV light curves shows some difference for AIA and EVE, suggesting the possibility of different contributions to the emissions observed by the two instruments, particularly in low-temperature channels in the early phase of the flare.

For the AIA 131 Å channel, the synthetic light curve evolves along with the observed light curve, both exhibiting the two stages of heating and similar rise and decay timescales. The comparison between synthetic and observed EVE light curves at the Fe XXI 128.75 Å line is also agreeable, both exhibiting very similar time evolution. The Fe XXI line is formed at around 10 MK, which gives the most reliable observations of hot plasmas in this flare. We note that, at the emission maximum, the model has over-estimated the amount of Fe XXI 128.75 Å line emission by about 50% if compared with the estimated line emission from the flare, or about 20% if compared with the line emission from the entire disk. These hot plasmas at 10 MK, however, only generate 80% emission in AIA 131 Å channel, indicating that a significant amount of AIA 131 Å emission may be produced by some other components, such as a low temperature component at the footpoints. Both the calculated and observed emission from the footpoint pixels appears to be comparable with the emission by 10 MK plasmas, which amounts to about 50% of the total emission. Note that the model estimated footpoint emission has an uncertainty by a factor of a few (see discussions in Qiu et al., 2013), and the observed footpoint emission provides an upper limit of the real footpoint emission for reasons discussed above. On the other hand, analysis conducted earlier (Figure 3.3e) shows that low-temperature lines (such as O VI and Fe VIII formed at $T_{max} = 300,000 - 400,000K$) in EVE spectra contributes 20% of the total emission seen in the AIA, though the estimate is made from full-disk observations which include emissions by the other two flares. Summarizing all these results, it may be stated that 10 MK plasmas in flare loops contribute 50% - 80% to the total flare emission seen in the AIA 131 Å channel, and the rest of the emission is by low-temperature plasmas at the flare footpoints, and these two components have very similar time profiles.

We then compare synthetic and observed emissions in the 94 Å band, presumably by plasmas cooled down to 6 MK. The model produces the time profile and amount of emission comparable with observations by both AIA and EVE. Model results further show that almost all emission in both the AIA channel and EVE Fe XVIII line is produced by 6 MK plasmas in flare loops, and the low-temperature footpoint emission is negligible, indicating predominant contribution to AIA 94 Å channel by the Fe XVIII line. This result is consistent with the analysis shown in Figure 3.3(f). The observed "footpoint" emission in the AIA 94 Å appears significant, but cannot be reproduced by the model. This should be largely due to over-estimate of footpoint emission by overlapping loop emissions in this band, though it is also likely that the low-temperature response in the present AIA 94 Å response function is underestimated due to missing lines in the CHIANTI database (Schmelz et al., 2013; Aschwanden et al., 2013).

At a lower temperature of around 3 MK, the synthetic light curves of flare loop emission in AIA/335 Å and the Fe XVI line are also very similar. Like in the 131 channel, the model produces more Fe XVI line emission formed at 3 MK, but does not produce enough emission in the AIA/335 Å, particularly in the early phase before 100 minutes. By adding the low-temperature (<1 MK) emission from the footpoints, the model can produce enough emission in the early phase as observed in AIA; it is also shown that the model calculated footpoint emission is rather comparable with AIA observed "footpoint" emission in the early phase. At the peak emission at around 80 min, the estimated footpoint low-temperature emission amounts to 60% of the total emission, which should be taken as an upper-limit. The analysis in Figure 3.3(g) suggests that, in this early phase, about 30% emission is from the spectral range 128-135 Å, part of which could be due to low-temperature O VI and Fe VIII lines, as in the case of the 131 Å channel. These results, though bearing large uncertainties, all indicate the presence of significant low-temperature component at the flare footpoints in the AIA/335 Å band during the early phase of the flare. After 100 minutes, emission of the Fe XVI line by 3 MK plasmas dominates the AIA/335 Å channel, as also indicated in Figure 3.3(g).

At a still lower temperature of 2 MK reflected in the AIA 211 channel and EVE Fe XIV line, the calculated light curves by coronal loop emission are very similar.

Both rise gradually and peak around the same time at 120 minutes. These calculated emissions are comparable with the observed emission in the late phase (after 110 minutes) of the flare, indicating that Fe XIV line makes significant contribution to flare emission detected in AIA/211 Å channel during the decay phase. The comparison of the early phase of the light curves is quite different. The observed light curves by both AIA and EVE show strong emission early in the flare that peaks at 85 minutes. By taking into account the footpoint emission of up to 1 MK, the model can reproduce the early phase of the AIA-observed light curve. The calculated footpoint emission agrees with the AIA observed "footpoint" light curve in the early phase, confirming the presence of this emission component by low-temperature footpoint sources by perhaps more than 50% of the total emission. However, < 1 MK emission makes little contribution to the EVE Fe XIV line. It is therefore puzzling what leads to the enhanced early-phase emission in this line observed by EVE. This issue will be discussed in the next section.

Finally, we calculate the UV emission from the flare footpoints to compare with observations. The AIA UV channel at 1600 Å records emissions mostly from Si I continuum formed in the upper photosphere and the C IV doublet at 1548 Å and 1551 Å formed in the transition region at the temperature of 10^5 K. Furthermore, the solar Si I continuum emission below 1682 Å is primarily excited by the C IV doublet (Machado & Henoux, 1982; Machado & Mauas, 1986). Therefore, the continuum intensity at $\lambda < 1682$ Å is approximately proportional to the intensity of C IV doublet

(Phillips et al., 1992). With the calculated transition region DEM under the equilibrium assumption, we can calculate the C IV doublet flux (in units of data counts) to compare with the observed flux by the AIA/1600 Å. The calculation is made for each UV brightened pixel only during the decay phase, when impulsive heating has finished and the equilibrium conditions can be reasonably assumed. Figure 3.9 shows the computed decay-phase C IV emission in comparison with the UV 1600 Å emission observed by AIA. The synthetic count rate in C IV line is calculated in each individual footpoint by convolving the transition region DEM with the contribution function of C IV from CHIANTI atomic data with ionization equilibrium (Mazzotta et al., 1998) and solar coronal abundance (Feldman et al., 1992). The total C IV flux is the sum of the flux in all footpoints. The observed total UV count rate in the decay phase is derived by summing the decay phase emission from each footpoint, which is obtained by subtracting the full Gaussian indicative of impulsive heating from the observed UV light curve. Figure 3.9 shows that the time profile of the model computed C IV count rate agrees well with that observed UV count rate, and the amount of observed UV flux is 2.7 times the synthetic C IV flux. The same proportionality was also found in another flare observed by TRACE and analyzed by Liu et al. (2013). These results confirm that the UV continuum flux is proportional to the C IV flux. The excellent agreement between computed and observed UV time profiles suggests that the equilibrium transition region DEM is reasonable, and therefore, the simple loop heating model used in this study manages to produce the correct evolution timescale.

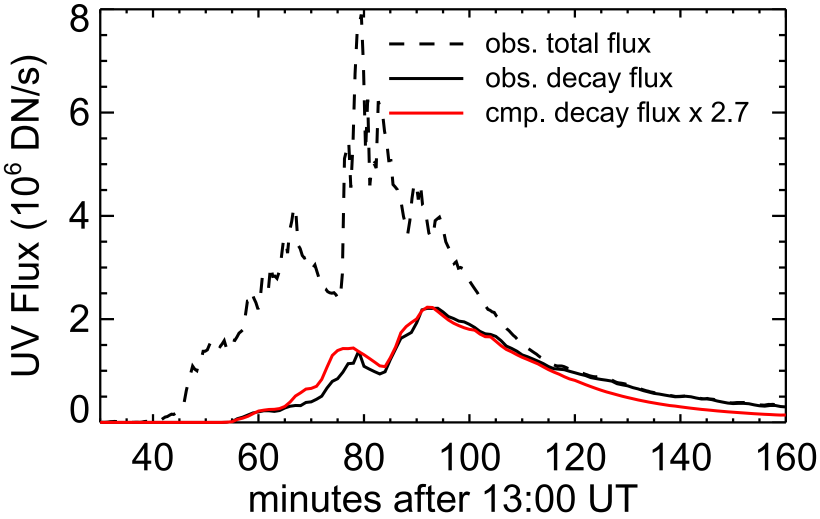

Figure 3.9: Comparison of the synthetic transition region C IV line emissions (red) in the decay phase with the UV flux observed by AIA/1600 Å channel (black) for all flare loops. The observed decay flux is derived by subtracting the full Gaussian profile that represents the rise of UV light curve from the observed light curve for each footpoint and summing over all footpoints.

In summary, the above comparisons show reasonable agreement between model predicted and observed light curves in AIA-131/EVE-128 and AIA-94/EVE-94 pairs. Analyses from all aspects rather consistently indicate predominant contributions by 10 MK and 6 MK plasmas to the AIA 131 and 94 channels, respectively, with a small fraction of low-temperature component from the flare footpoints contributing to the AIA 131 emission. It is also shown that model calculation taking into account significant footpoint emission agrees with broad-band AIA observations in 335, 211, and UV 1600 Å bands. However, the model calculation does not agree with EVE-observed iron lines at low temperatures in the early phase. Both EVE and AIA observe a prominent emission peak at around 85 min in 211 channel/line. Spatially resolved observations by AIA show that this emission component most likely comes from the flare footpoint, and the calculation suggests that the footpoint emission is by low-temperature plasmas in the transition region. However, this low-temperature emission cannot be produced in the EVE observed iron lines that are formed at temperatures higher than 1 MK. In the next section, we further discuss what may cause these discrepancies, and the implication on our understanding of plasma properties in flare loops.

3.5 Discussions and Conclusions

In this chapter, we have studied flare emissions observed by SDO/AIA and SDO/EVE. We compared the light curves in four EUV channels (131 Å, 94 Å, 335 Å, and 211 Å) onboard AIA and intensity of four iron lines (Fe XXI at 128.75 Å, Fe XVIII at 93.93 Å, Fe XVI at 335.41 Å, Fe XIV at 211.32 Å) observed by EVE. The comparison shows that the AIA observed light curves are very similar to the line intensity light curves observed by EVE. When we convolve these lines observed by EVE with the AIA response functions, we find the contribution of these lines to the AIA channels to be 60%, 100%, 70%, and 30%, respectively, of the AIA observed total emission. These results are in general comparable with the prediction by O'Dwyer et al. (2010). Our analysis also shows that the line contributions to the AIA 335 and 211 channels vary from the early phase to the late phase of the flare.

Comparison of spectrally resolved EVE observations with spatially resolved AIA observations provides us with better diagnostics of properties of flare plasmas, as well as information of where, from flare loops or footpoints, flare EUV emissions are generated. To aid with the diagnostics, we use a recently developed method to model evolution of flare plasmas in a few thousand flare loops with observationally constrained heating rates. With a few idealized assumptions, the model provides temperature and density distribution of flare plasmas in the corona as well as in the transition region of flare footpoints, and allows us to calculate synthetic AIA and EVE light curves to compare with observations. The results show that, in general, the synthetic light curves taking into account emissions by both coronal plasmas in flare loops and transition region plasmas at the flare footpoints are in reasonable agreement with broad-band AIA observations in the four EUV channels as well as the UV 1600 Å channel. Light curves of EVE-observed iron lines at relatively high temperatures (10 MK for Fe XXI at 128.75 Å, 6 MK for Fe XVIII at 93.93 Å, 3 MK for Fe XVI at 335.41 Å) can also be reproduced by the computed flare DEM. The model also produces emissions in the other iron line Fe XIV at the lower temperature (2 MK) in the late (cooling) phase of the flare comparable with observations. These results indicate that the method is able to describe the mean flare plasma properties in the corona as the result of heating and cooling of numerous individual flare loops. The comparison yields estimates of the heating rates in these loops that range from 1.3×10^{26} ergs to 1.5×10^{28}, and the total heating energy in the flare amounts to 4.5×10^{30} ergs.

However, the model does not reproduce the enhanced emission in the early phase in the ∼2 MK iron lines observed by EVE. Such early-phase enhancement is also observed by AIA as primarily originating from the flare footpoint. Whereas the model computed footpoint emission by low-temperature plasmas (< 1 MK) well fits the broad-band AIA observation of this early-phase emission component, the model cannot generate the enhanced line emission observed by EVE. Such discrepancy leads to the question about the nature of the early-phase emission component seen by both AIA and EVE: does nearby line-blending or continuum emission account for this early phase enhancement? Or is the model computed DEM appropriate for this temperature range?

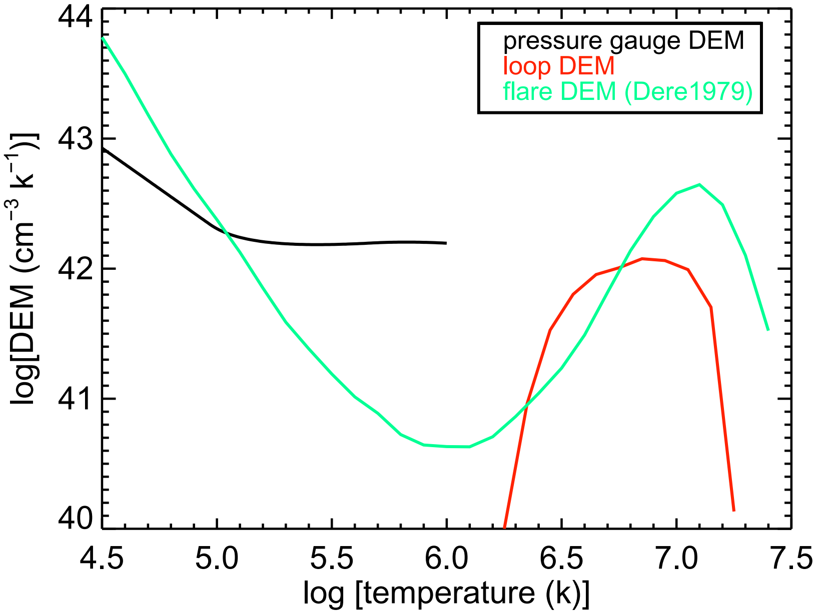

Figure 3.10: Flare DEM at 14:25 UT. The DEM of footpoints estimated from pressure gauge is plotted in black, DEM of all loops is plotted in red, in comparison with decay phase flare DEM ($n^2 ds/dT$) derived from X-ray and UV line intensities observed by *Skylab* (Dere & Cook, 1979) multiplied by an assumed area of $10'' \times 20''$.

To various degrees, all above factors are likely, but our available observations cannot disentangle these factors unambiguously. In terms of the continuum emission, O'Dwyer et al. (2010) and Milligan & McElroy (2013) have shown that the free-free continuum and He II continuum contribute significantly to the AIA/211 Å channel during the flare, by up to 40%. Both the AIA images and model calculation show that the early-phase emission component is from flare footpoints, likely by transition region plasmas heated to 1-2 MK. The synthetic light curves using the broad-band AIA temperature response function may have taken into account the continuum emission or line blending effects if any; however, the continuum emission or line-blending effect is not considered in calculating the iron Fe XIV 211.32 Å line. We consider it most likely that the model estimated DEM is inappropriate in the temperature range between 1 - 3 MK, due to the limitation of the 0D approach. The zero-dimensional approach produces the mean temperature of a flare loop above 2 MK. Meanwhile, we estimate a one-dimensional temperature distribution in the transition region, up to an arbitrary temperature cutoff of 1 MK, at the flare footpoint with an equilibrium assumption. Counting all flare loops, the flare DEM from 0.1 to 10 MK at 85 min is given in Figure 3.10, in comparison with the flare DEM ($n^2 ds/dt$) derived from X-ray and UV spectral observations of a large flare on 1973 August 9 obtained by *Skylab* (Dere & Cook, 1979) multiplied by an assumed area of $10'' \times 20''$. The DEM used in this chapter, though being able to successfully reproduce observed emission at both high (5-12 MK) and very low (0.1 MK) temperatures, exhibits an evident artificial gap between 1-3 MK. In reality, there should not be a discontinuity when the 1d approach is taken, in which case, it is expected that the DEM between 1-3 MK be smooth and continuous. As the consequence, one might expect little change in the synthetic AIA light curves because of the broad temperature response of AIA instruments; on the other hand, filling-up of the DEM gap between 1-3 MK would significantly enhance the Fe XIV 211.32 Å line formed at 2 MK to make up for the early-phase emission as observed by EVE. Further investigation into these issues requires un-ambiguous flare spectral observations by EVE as well as improvement of 1d loop heating model that treats evolution of multiple loops that contribute to emissions seen in AIA and EVE.

The work is supported by NSF grant ATM-0748428. CHIANTI is a collaborative project involving the University of Cambridge (UK), George Mason University, and the University of Michigan (USA). *SDO* is a mission of NASA's Living With a Star Program.

4. SUMMARY OF THREE FLARES

4.1 Introduction

In the previous two chapters, we have analyzed and modeled two flares that have different characteristics and were observed by different instruments. The first flare, the M8.0 flare on 2005 May 13, is a standard long-duration two-ribbon flare associated with a fast coronal mass ejection (CME). It is evident, from the high-resolution and high-cadence UV observations by *TRACE*, that magnetic reconnection, formation of flare loops, and energy release into these loops continue well into the decay phase defined by the *GOES* SXR light curve. Non-thermal emission up to 100 keV is observed by *RHESSI* during the impulsive phase. For this flare, we are able to infer heating rates in flare loops that also include the heating term by upflows driven by precipitating non-thermal electrons, and therefore can also estimate the fraction of non-thermal energy out of the total heating energy. Our method has produced thermal bremsstrahlung spectrum by very hot plasmas from 10 - 20 MK in excellent agreement with *RHESSI* observations during the main phase. However, the method does not yield sufficient SXR emission during both the rise and decay phase. The question is, has the method failed to identify weak heating events during these periods, or is the 0D mean property approach not appropriate to model plasma evolution in these phases? Since the flare was not observed in other wavelengths, we cannot verify model-computed plasma evolution from heating to cooling phase against observations in this event.

The second flare, the M1.9 flare occurring on 2011 March 7, is comprised of multiple flare loop systems in more complex magnetic fields than the standard two-dimensional bipolar configuration. The flare is a relatively short-duration event although it is also associated with a CME. The flare was observed by AIA and EVE onboard *SDO*, allowing us to study flare plasma evolution between 2 MK and 10 MK. We apply the same method to analyze and model this flare, and find reasonable agreement between synthetic and observed EUV emissions observed by both AIA and EVE, with EUV emissions from high to low temperatures mostly reproduced throughout the flare evolution from the rise to the decay phase. Furthermore, the combined spatially resolved AIA and spectrally resolved EVE observations allow us to distinguish EUV emissions by high-temperature plasma in flare loops and by low-temperature (< 1MK) plasma from the foot-points. In particular, we verify that, during the cooling phase of each loop, EUV and UV emissions at the foot-point are governed by the enhanced coronal pressure as a result of quasi-equilibrium between conductive heating and radiative loss in the transition region. These results indicate that the model appropriately describes mean properties of flare plasmas in multiple loops shortly after heating, and in this event, the method appears to be able to identify enough heating events throughout the flare. The remaining question is still about the early phase of the flare, when the impulsive EUV and UV emissions in the transition region cannot be reproduced (also see Qiu et al., 2013), whereas the synthetic EUV emission at 131Å by 10 MK plasma tends to overshoot.

Combining results of these two flares, it is reasonable to believe that the mean-property approach of the 0D EBTEL model may not properly describe the physics of the impulsive heating phase, when the physical system is far from equilibrium regime. In addition, these two flares are both associated with CMEs; there are likely weak reconnection events occurring high in the corona during the decay phase when the CME is developing and propagating, leading to weak heating events that do not produce strong footpoints signatures. On 2012 June 17, a compact short-lived C3.9 flare took place and was very well observed throughout its duration by a cluster of instruments including *RHESSI*, AIA, EVE, and the New Solar Telescope at Big Bear Solar Observatory (NST/BBSO; Goode et al., 2010; Cao et al., 2010) in optical and infrared wavelengths. The nearly complete coverage of the flare from infrared to SXR wavelengths from its rise through decay provides an optimal opportunity to study heating and cooling of flare loops from high temperature (>10 MK) to low temperature (below 1 MK). EBTEL modeling and analysis of the flare observations by AIA and NST has been conducted (Zeng et al., 2014). In this chapter, we analyze the spectra of this compact flare observed by *RHESSI* and EVE, in comparison with the other two eruptive flares reported in the previous two chapters. This Chapter is organized as follows: observations and analysis of the C3.9 flare are presented in Section 4.2, and comparison and summary of the results for the three flares are presented in Section 4.3, followed by conclusions and discussions in Section 4.4.

4.2 Observations and Analysis of a Compact C3.9 Flare

The C3.9 flare is a compact flare that occurred in active region AR11504 on June 17, 2012. The flare is observed by *SDO* and NST/BBSO. Using the same method as Liu et al. (2013), observations of the flare are analyzed, and EBTEL model is applied to derive plasma properties in multiple loops identified from UV light curves and compute the synthetic EUV emission observed by AIA as well as the infrared He I 10830Å emission observed by NST (see Zeng et al., 2014, for details of the flare analysis and modeling). In this chapter, we focus on the flare thermal bremsstrahlung spectrum observed by *RHESSI* as well as EUV lines observed by EVE.

The full-disk spectra in wavelength ranges of the four AIA channels observed by EVE are plotted in the upper panel of Figure 4.1 with colors from black to red indicating evolution of the spectra during the flare. The corresponding AIA response functions (effective areas) obtained from the *SolarSoftWare* (Freeland & Handy, 1998) are overplotted in the upper panel. We convolve different parts of the EVE spectrum with the wavelength response function of each AIA channel (in units of cm^2 DN photon^{-1}) to make predicted AIA light curves, which are plotted in different colors (dark green, cyan, magenta, and orange) in the bottom panel of Figure 4.1. Same as the M1.9 flare on March 7th 2011, the AIA 131Å channel is dominated by Fe XXI

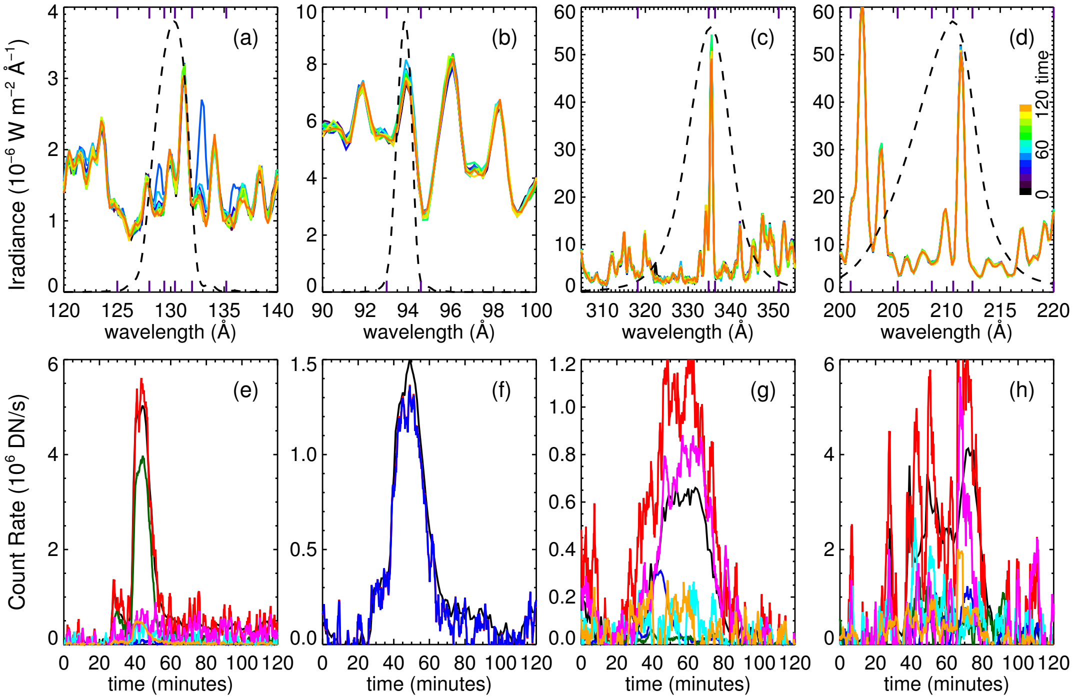

Figure 4.1: Upper: solar spectra observed by *SDO*/EVE for four *SDO*/AIA channels ((a) AIA/131 Å, (b) AIA/94 Å, (c) AIA/335 Å, and (d) AIA/211 Å) with colors indicating the time of observations. The arbitrarily scaled effective areas of these AIA EUV channels are overplotted in dashed lines. Lower: predicted light curves in four AIA channels (in units of DN/s) by convolving the EVE-observed irradiance spectrum in different wavelength ranges (different colors; the wavelength ranges are also indicated by tick marks in the upper panel) with AIA wavelength response functions in comparison with the total counts light curves observed by AIA (black). (e) AIA/131 Å, Red (EVE full spectra), blue ([125.0 Å, 128.0 Å]), dark green ([128.0 Å, 129.4 Å]), cyan([129.4 Å, 130.4 Å]), magenta([130.4 Å, 132.0 Å]), orange([132.0 Å, 135.2 Å]). (f) AIA/94 Å, Red (EVE full spectra), blue([93.0 Å, 94.6 Å]). (g) AIA/335 Å, Red (EVE full spectra), blue ([128.0 Å, 135.2 Å]), dark green ([135.2 Å, 318.0 Å]), cyan([318.0 Å, 334.8 Å]), magenta([334.8 Å, 336.2 Å]), orange([336.2 Å, 351.2 Å]). (h): AIA/211Å, Red (EVE full spectra), blue ([201.0 Å, 205.4 Å]), dark green ([205.4 Å, 208.6 Å]), cyan([208.6 Å, 210.6 Å]), magenta([210.6 Å, 212.4 Å]), orange([212.4 Å, 219.6 Å])

line at 128.75Å contributing up to 70% of total emission in this channel, emission in the AIA 94Å channel mostly comes from Fe XVIII line at 93.43Å (more than 90%), the AIA 335Å channel is dominated by Fe XVI line, and the AIA 211Å channel is complicated with contributions from lots of iron lines centered around 211Å.

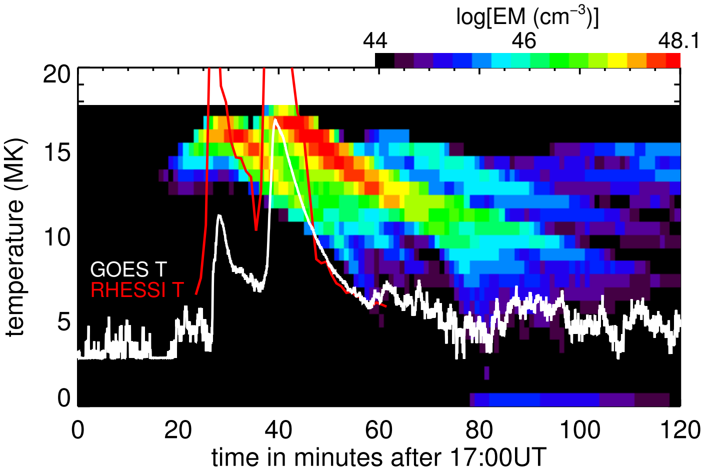

Figure 4.2: The coronal DEM from modeling of the C3.9 flare on 2012 June 17. Also plotted in the figure are the temperatures of the plasmas estimated from GOES (white) and RHESSI (red) observations with isothermal assumption.

Figure 4.2 shows the evolution of coronal differential emission measure (DEM) from all plasma in flare loops, which is calculated with temperatures and densities of over 800 half loops adopted from Zeng et al. (2014). Also plotted in Figure 4.2 are the flare temperature estimated from *GOES* and *RHESSI* observations with the assumption that the flare is isothermal. Figure 4.2 shows that the modeled DEM rises toward high temperature together with the *GOES* and *RHESSI* temperatures as flare loops are being heated. The peak DEM then evolves toward low temperature on timescales consistent with the decrease of *GOES* and *RHESSI* temperatures. The figure also shows that the temperature of hottest plasma from the model is lower than the *RHESSI* temperature but higher than *GOES* temperature. We then calculate emissions of the flare in SXR and several EUV lines using CHIANTI (Dere et al., 1997; Landi et al., 2012) atomic data and the DEM. The synthetic SXR light curves (in units of photons s^{-1}) in the 3–6, 6–12, and 12–25 keV bands are plotted in Figure 4.3 to compare with photon flux observed by *RHESSI* detector G1. For this flare, the spectra from detectors other than G2 and G4 all look very similar with real solar flux extending from about 3 keV to about 30 keV, therefore, we analyze photon observations by detector G1. Figure 4.3 shows that time scales of the rise and decay of these synthetic light curves agree with observation. The figure also shows that before 17:45 UT model produced emission is greater than observed at low energies.

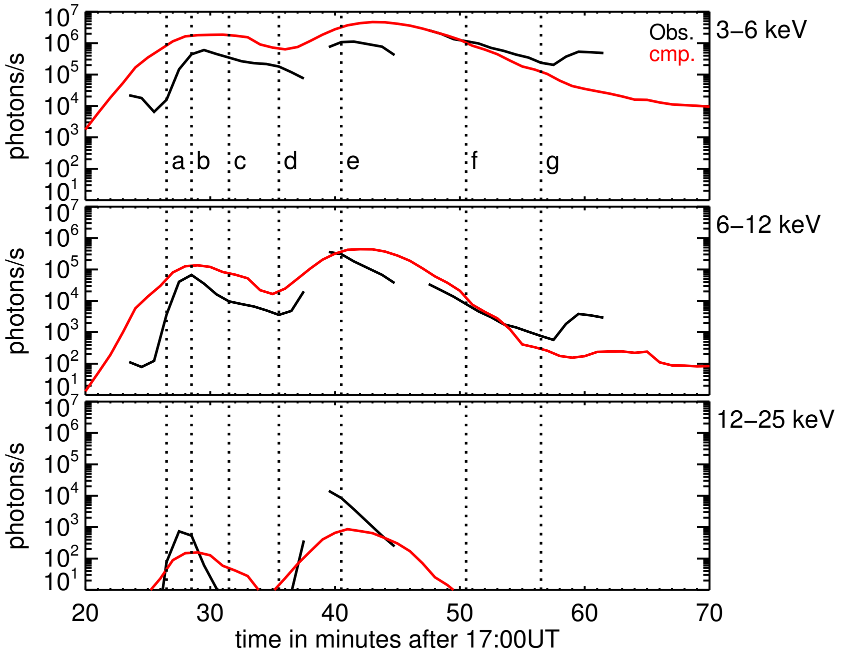

Figure 4.3: Comparison of the synthetic SXR light curves (in units of photons/s) from the model (red) with that from fitting of *RHESSI* SXR spectra (black) in the 3–6 keV, 6–12 keV, and 12–25 keV bands. The vertical dotted lines and letters a–g indicate the times when the spectral comparison is plotted in Figure 4.4.

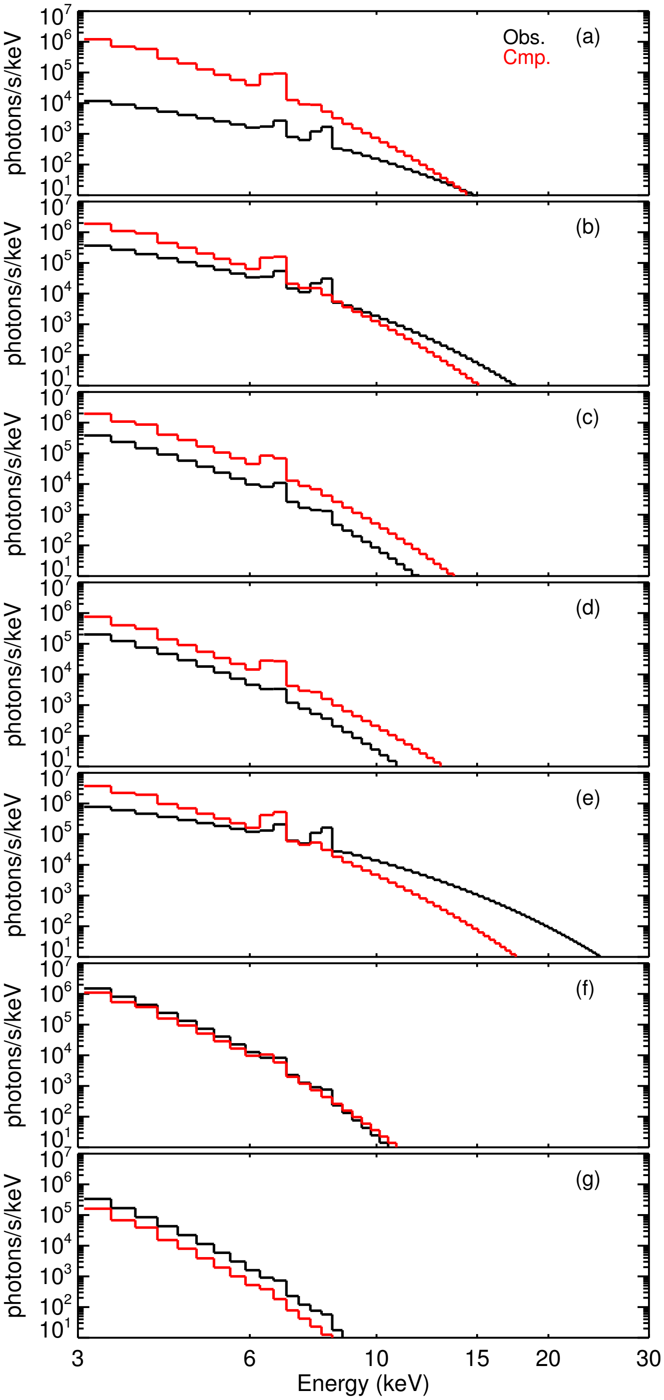

Figure 4.4: Comparison of synthetic SXR spectra (in the unites of photons/s/keV) from the model (red) with that from the *RHESSI* observation (black) at a few times during the flare. The time of each panel is indicated by vertical dotted lines in Figure 4.3.

To explore more details of the SXR emission, we plot the synthetic and observed thermal bremsstrahlung spectrum (in units of photons s^{-1} keV^{-1}) at seven different times shown in Figure 4.4. The comparison of SXR spectra shows that, during the rise phase of the flare, the synthetic spectrum is softer than observed, indicating that the model produces insufficient high-temperature plasmas and over-abundant plasmas at relatively lower temperature. During the decay phase, the model agrees with observations (for example at around 17:51 UT). The lack of high temperature plasma in the model-computed DEM in the flare rising phase is also found for the M8.0 flare studied in Chapter 2 by comparing of SXR spectra with *RHESSI* observation, which may be explained by the fact that the 0D model only yields the mean temperature and density in the loop. We also note that, as shown in the following analysis, the synthetic emission at around 10 MK overshoots the emission observed by AIA and EVE by a factor of 3 from 25 - 45 min, which is likely the result of over-abundant plasmas produced at this temperature at the price of insufficient higher temperature plasmas, as reflected in the comparison of the *RHESSI* SXR spectrum at energy >10 keV.

To study cooling of plasma in flare loops from 10 MK to 2 MK, we plot the synthetic EUV light curves in four EUV lines and corresponding AIA channels in Figure 4.5, and compare them with that observed by EVE and AIA. The figure shows that the synthetic EUV light curves agree with observations within a factor of 3. This agreement omits the first sharp peak in AIA 211 Å channel which comes from

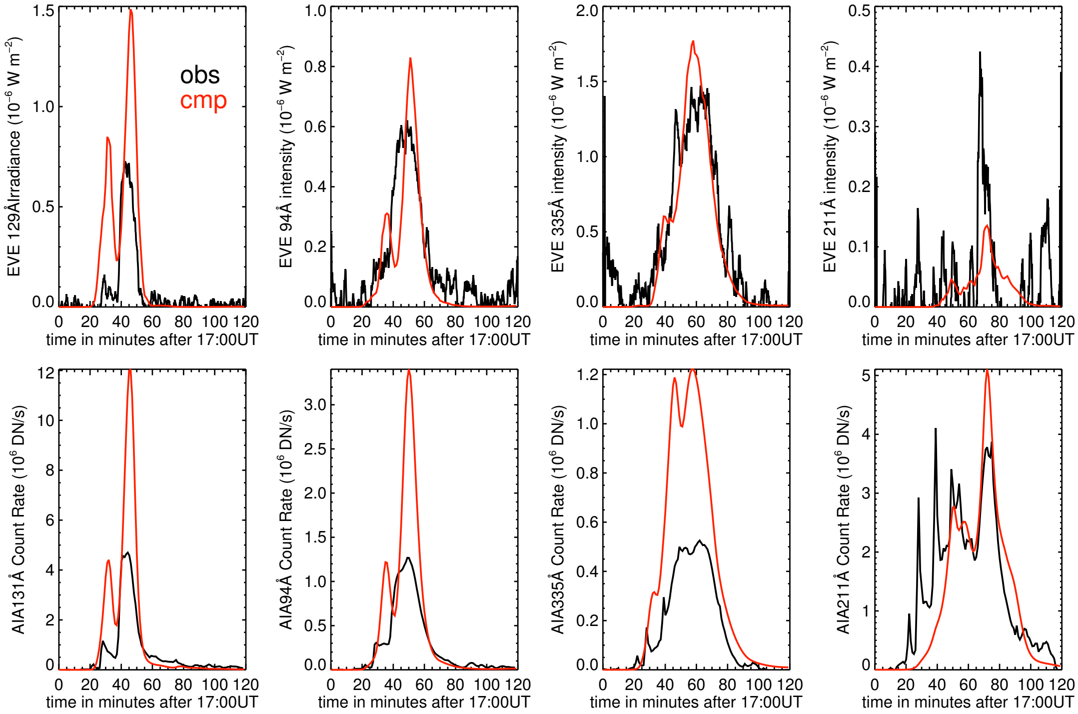

Figure 4.5: Top Panel: comparison of the synthetic line intensities in four irons lines Fe XXII line at 128.75 Å, Fe XVIII line at 93.93 Å, Fe XVI line at 335.41 Å, and Fe XIV line at 211.32 Å(red) with EVE-observed line emissions from the flare (black). Bottom panel: comparison of the synthetic light curves (red) with that observed (black) in four AIA EUV channels (131 Å 94 Å, 335 Å, and 211 Å).

impulsively heated plasma at the footpoint and therefore could not be reproduced by the model when only coronal plasma is used to calculate synthetic light curve in 211 Å channel. Compared with the M1.9 flare studied in Chapter 3, better agreement has been found in this flare between synthetic and observed EUV light curves at all different temperatures in both the rise and decay phases. The reproduction of decay phase light curves in these EUV channels of this compact C3.9 flare indicate that formation and heating of flare loops take place in a confined space in a short duration, and these heating events are identified from foot-point UV signatures; in comparison, in flares associated with CMEs, it is very likely that a good number of weak reconnection events continue to occur high in the corona in the decay phase without producing significant footpoint signatures.

4.3 Summary of the Three Flares

The characteristics of the three flares and heating rates in these three flares are summarized in Table 4.1. It is evident that the larger flare is heated more. For the three flares we studied, the total heating energy is roughly proportional to the magnitude of the flare, i.e., the peak SXR emission in 1–8Å of the flare. The correlation between the heating energy and peak SXR emission is explained by the fact the more energy used to heat plasmas in flare loops, more plasmas will be heated to a higher energy and therefore more EM at higher temperature is produced. Table 4.1 also shows that the biggest flare has the largest amount of magnetic flux reconnected. Since the process of flare loops formed by reconnection and heated by energy released from reconnection is complicated, the relation between the total heating energy and reconnection flux is not linear. Furthermore, the first two flares are both associated with CMEs, with significant amount of reconnection-released energy carried away by the CME.

Among the three flare, the M8.0 flare has significant HXR emissions observed by *RHESSI*. The HXR light curve is used to estimate the energy carried by beam-driven

Table 4.1: Summary of three flares

date	class	total energy (10^{30} ergs)	reconnection flux (10^{20} Mx)	nth emission	CME
2005/05/15	M8.0	12.3	58.9	Yes	Yes
2011/03/11	M1.9	4.64	9.74	No	Yes
2012/06/17	C3.9	0.787	0.208	No	No

upflows during the flare, which is 1.9 $\times 10^{30}$ ergs, or ~16% of the heating energy of the flare (1.22×10^{31} ergs).

We note that for the compact C3.9 flare without CME the synthetic light curves from coronal plasmas in the decay phase are in excellent agreement with observations, and for the other two flares, the synthetic light curves decay faster than observations. This may be explained by the picture that CME associated flares might have continuous reconnection in the decay phase which provides direct heating in the corona, and the heating is so weak that neither non-thermal particles nor thermal conduction would provide significant heating of the lower-atmosphere to produce much enhanced foot-point emission (e.g., Moore et al., 1980; Veronig et al., 2002a,b; Woods et al., 2011).

4.4 Conclusion, Discussion, and Future Work

In this dissertation, we have analyzed and modeled three flares of different magnitudes and different morphology. We use UV observations at footpoints to identify flare loops formed by magnetic reconnection and to infer the heating rate. When, for how long, and by how much each individual loop is heated are all determined from observed UV light curves at the foot-points where the loops are anchored. Only **two** free parameters, one used in constructing the heating rate, and the other specifying the energy loss through the transition region, are left to be determined by comparison of synthetic radiation (both light curves and spectra) from flaring plasmas calculated using EBTEL model and CHIANTI atomic data with observations by *RHESSI*, *GOES*, AIA, and EVE. These observations allow us to study evolution of flare plasmas in the corona from tens of MK to 1 MK as well as transition region emission of a few thousand K. For flares with non-thermal emissions, a third free parameter prescribing the fraction of beam driven upflows in the total heating energy can be also determined using hard X-ray observations. In our work, we use all observable data to constrain the heating rate from input to output. This is a major improvement in calculating energy release and heating of flare loops. For comparison, previous studies of flare loop heating have all used mostly arbitrarily prescribed heating rates.

The agreement of total emission from the model with observations (both spectra and light curves) indicates that the 0D EBTEL model is adequate for studying cooling phase of individual loops and mean properties of a large number of loops. The method of combining identification of heating events from foot-point signatures and EBTEL modeling is valuable and efficient to provide a good estimate of total heating energy in flares. Importantly, we also derive magnetic reconnection rates using foot-point UV emission signatures and magnetic field measurements that can be made only in the lower-atmosphere. Therefore, the study provides the connection between magnetic reconnection and flare energy that is released by reconnection. To further extend this work, we can apply this method to analyzing a larger number of flares, to explore and establish the scaling law between loop heating rate, reconnection rate, and plasma properties.

The study of the three flares also reveals places for further improvement. As evident in all three flares, the 0D model of the mean-property approach and empirical treatment of the lower atmosphere cannot properly address the physics during the impulsive heating phase. As a result, the model does not produce enough SXR emission at the high(est) temperature nor the low-temperature UV and EUV emission from the transition region during the rise phase of the flare. Like most of the existing loop heating models, our work also does not deal with heating mechanisms. The heating rate is treated merely as an energy input in the energy conservation equation. We have investigated the effect of particle beam heating, which is done in an empirical way assuming that energy carried in the beam-driven upflow is directly proportional to observed HXR counts. These limitations would be improved by extending our work to more advanced 1D hydrodynamic loop model with the heating rates derived from this work, and using non-LTE radiative transfer to study the lower-atmosphere response. More advanced 1D hydrodynamic model could resolve plasma properties (density, temperature, pressure) and energies along the loop. With the transition region and chromosphere more precisely modeled by solving non-LTE radiative transfer equations, it would help diagnose impulsive phase dynamics, and in turn provide a quantitative basis of inferring heating rates from the impulsive UV and HXR light curves.

REFERENCES CITED

Abbett, W. P., & Hawley, S. L. 1999, ApJ, 521, 906

Allred, J. C., Hawley, S. L., Abbett, W. P., & Carlsson, M. 2005, ApJ, 630, 573

Antiochos, S. K. 1980, ApJ, 241, 385

Antiochos, S. K., MacNeice, P. J., Spicer, D. S., & Klimchuk, J. A. 1999, ApJ, 512, 985

Antonucci, E. 1989, Sol. Phys., 121, 31

Aschwanden, M. J. 2002, Space Sci. Rev., 101, 1

Aschwanden, M. J., & Alexander, D. 2001, Sol. Phys., 204, 91

Aschwanden, M. J., Boerner, P., Schrijver, C. J., & Malanushenko, A. 2013, Sol. Phys., 283, 5

Benka, S. G., & Holman, G. D. 1994, ApJ, 435, 469

Benz, A. O. 2008, Living Reviews in Solar Physics, 5, 1

Boerner, P., Edwards, C., Lemen, J., et al. 2012, Sol. Phys., 275, 41

Boteler, D. H. 2006, Advances in Space Research, 38, 159

Brekke, P., Rottman, G. J., Fontenla, J., & Judge, P. G. 1996, ApJ, 468, 418

Brown, J. C. 1973, Sol. Phys., 31, 143

Canfield, R. C., & Gayley, K. G. 1987, ApJ, 322, 999

Cao, W., Gorceix, N., Coulter, R., et al. 2010, Astronomische Nachrichten, 331, 636

Cargill, P. J., Bradshaw, S. J., & Klimchuk, J. A. 2012a, ApJ, 752, 161

—. 2012b, ApJ, 758, 5

Cargill, P. J., Mariska, J. T., & Antiochos, S. K. 1995, ApJ, 439, 1034

Carmichael, H. 1964, NASA Special Publication, 50, 451

Carrington, R. C. 1859, MNRAS, 20, 13

Caspi, A. 2010, PhD thesis, Department of Physics, University of California, Berkeley, CA 94720-7450, USA

Caspi, A., Krucker, S., & Lin, R. P. 2014a, ApJ, 781, 43

Caspi, A., & Lin, R. P. 2010, ApJ, 725, L161

Caspi, A., McTiernan, J. M., & Warren, H. P. 2014b, ApJ, 788, L31

Cheng, C.-C., Oran, E. S., Doschek, G. A., Boris, J. P., & Mariska, J. T. 1983, ApJ, 265, 1090

Cheng, C.-C., Tandberg-Hanssen, E., Bruner, E. C., et al. 1981, ApJ, 248, L39

Cheng, C.-C., Tandberg-Hanssen, E., & Orwig, L. E. 1984, ApJ, 278, 853

Cheng, C.-C., Vanderveen, K., Orwig, L. E., & Tandberg-Hanssen, E. 1988, ApJ, 330, 480

Cheng, J. X., Kerr, G., & Qiu, J. 2012, ApJ, 744, 48

Cliver, E. W., & Dietrich, W. F. 2013, Journal of Space Weather and Space Climate, 3, A260000

Cook, J. W., & Brueckner, G. E. 1979, ApJ, 227, 645

Cox, D. P., & Tucker, W. H. 1969, ApJ, 157, 1157

Coyner, A. J., & Alexander, D. 2009, ApJ, 705, 554

Del Zanna, G., & Woods, T. N. 2013, A&A, 555, A59

Dennis, B. R., & Schwartz, R. A. 1989, Sol. Phys., 121, 75

Dennis, B. R., & Zarro, D. M. 1993, Sol. Phys., 146, 177

Dere, K. P., & Cook, J. W. 1979, ApJ, 229, 772

Dere, K. P., Landi, E., Mason, H. E., Monsignori Fossi, B. C., & Young, P. R. 1997, A&AS, 125, 149

Dere, K. P., Landi, E., Young, P. R., et al. 2009, A&A, 498, 915

Dere, K. P., & Mason, H. E. 1993, Sol. Phys., 144, 217

Doschek, G. A. 1997, ApJ, 476, 903

Doschek, G. A., Boris, J. P., Cheng, C. C., Mariska, J. T., & Oran, E. S. 1982, ApJ, 258, 373

Doschek, G. A., Dere, K. P., & Lund, P. A. 1991, ApJ, 381, 583

Doschek, G. A., Feldman, U., Kreplin, R. W., & Cohen, L. 1980, ApJ, 239, 725

Doschek, G. A., Warren, H. P., & Young, P. R. 2013, ApJ, 767, 55

Emslie, A. G. 1978, ApJ, 224, 241

—. 1980, ApJ, 235, 1055

Emslie, A. G., Li, P., & Mariska, J. T. 1992, ApJ, 399, 714

Emslie, A. G., & Nagai, F. 1985, ApJ, 288, 779

Feldman, U., Doschek, G. A., Kreplin, R. W., & Mariska, J. T. 1980, ApJ, 241, 1175

Feldman, U., Mandelbaum, P., Seely, J. F., Doschek, G. A., & Gursky, H. 1992, ApJS, 81, 387

Fisher, G. H. 1987, ApJ, 317, 502

Fisher, G. H., Canfield, R. C., & McClymont, A. N. 1984, ApJ, 281, L79

—. 1985a, ApJ, 289, 425

—. 1985b, ApJ, 289, 414

Fletcher, L., Hannah, I. G., Hudson, H. S., & Innes, D. E. 2013, ApJ, 771, 104

Fletcher, L., Pollock, J. A., & Potts, H. E. 2004, Sol. Phys., 222, 279

Fletcher, L., Dennis, B. R., Hudson, H. S., et al. 2011, Space Sci. Rev., 159, 19

Forbes, T. G., & Acton, L. W. 1996, ApJ, 459, 330

Freeland, S. L., & Handy, B. N. 1998, Sol. Phys., 182, 497

Goode, P. R., Coulter, R., Gorceix, N., Yurchyshyn, V., & Cao, W. 2010, Astronomische Nachrichten, 331, 620

Grechnev, V. V., Kurt, V. G., Chertok, I. M., et al. 2008, Sol. Phys., 252, 149

Grevesse, N., & Sauval, A. J. 1998, ßr, 85, 161

Griffiths, N. W., Fisher, G. H., & Siegmund, O. H. W. 1998, in Astronomical Society of the Pacific Conference Series, Vol. 154, Cool Stars, Stellar Systems, and the Sun, ed. R. A. Donahue & J. A. Bookbinder, 621

Guarrasi, M., Reale, F., Orlando, S., Mignone, A., & Klimchuk, J. A. 2014, A&A, 564, A48

Hamilton, R. J., & Petrosian, V. 1992, ApJ, 398, 350

Handy, B. N., Acton, L. W., Kankelborg, C. C., et al. 1999, Sol. Phys., 187, 229

Hannah, I. G., Christe, S., Krucker, S., et al. 2008, ApJ, 677, 704

Hawley, S. L., & Fisher, G. H. 1992, ApJS, 78, 565

—. 1994, ApJ, 426, 387

Hawley, S. L., Allred, J. C., Johns-Krull, C. M., et al. 2003, ApJ, 597, 535

Hill, S. M., Pizzo, V. J., Balch, C. C., et al. 2005, Sol. Phys., 226, 255

Hirayama, T. 1974, Sol. Phys., 34, 323

Hock, R. A., Woods, T. N., Klimchuk, J. A., Eparvier, F. G., & Jones, A. R. 2012, ArXiv e-prints

Hodgson, R. 1859, MNRAS, 20, 15

Holman, G. D. 1985, ApJ, 293, 584

—. 2012, ApJ, 745, 52

Hori, K., Yokoyama, T., Kosugi, T., & Shibata, K. 1997, ApJ, 489, 426

—. 1998, ApJ, 500, 492

Hudson, H. S. 2011, Space Sci. Rev., 158, 5

Inglis, A. R., & Gilbert, H. R. 2013, ApJ, 777, 30

Karlický, M., & Kosugi, T. 2004, A&A, 419, 1159

Kato, T. 1976, ApJS, 30, 397

Kašparová, J., Varady, M., Heinzel, P., Karlický, M., & Moravec, Z. 2009, A&A, 499, 923

Kazachenko, M. D., Canfield, R. C., Longcope, D. W., & Qiu, J. 2012, Sol. Phys., 277, 165

Kazachenko, M. D., Canfield, R. C., Longcope, D. W., et al. 2009, ApJ, 704, 1146

Kennedy, M. B., Milligan, R. O., Mathioudakis, M., & Keenan, F. P. 2013, ApJ, 779, 84

Klimchuk, J. A., Patsourakos, S., & Cargill, P. J. 2008, ApJ, 682, 1351

Knight, J. W., & Sturrock, P. A. 1977, ApJ, 218, 306

Kopp, R. A., & Pneuman, G. W. 1976, Sol. Phys., 50, 85

Landi, E., Del Zanna, G., Young, P. R., Dere, K. P., & Mason, H. E. 2012, ApJ, 744, 99

Landi, E., Young, P. R., Dere, K. P., Del Zanna, G., & Mason, H. E. 2013, ApJ, 763, 86

Lemen, J. R., Title, A. M., Akin, D. J., et al. 2012, Sol. Phys., 275, 17

Lin, J. 2004, Sol. Phys., 219, 169

Lin, J., & Forbes, T. G. 2000, J. Geophys. Res., 105, 2375

Lin, R. P., Dennis, B. R., Hurford, G. J., et al. 2002, Sol. Phys., 210, 3

Lin, R. P., Krucker, S., Hurford, G. J., et al. 2003, ApJ, 595, L69

Liu, C., Lee, J., Gary, D. E., & Wang, H. 2007, ApJ, 658, L127

Liu, W.-J., Qiu, J., Longcope, D. W., & Caspi, A. 2013, ApJ, 770, 111

Longcope, D., Beveridge, C., Qiu, J., et al. 2007, Sol. Phys., 244, 45

Longcope, D. W., Des Jardins, A. C., Carranza-Fulmer, T., & Qiu, J. 2010, Sol. Phys., 267, 107

Longcope, D. W., & Guidoni, S. E. 2011, ApJ, 740, 73

Machado, M. E., & Henoux, J.-C. 1982, A&A, 108, 61

Machado, M. E., & Mauas, P. J. 1986, in NASA Conference Publication, Vol. 2449, NASA Conference Publication, ed. B. R. Dennis, L. E. Orwig, & A. L. Kiplinger, 271–275

Mariska, J. T. 1987, ApJ, 319, 465

Mariska, J. T., Emslie, A. G., & Li, P. 1989, ApJ, 341, 1067

Mazzotta, P., Mazzitelli, G., Colafrancesco, S., & Vittorio, N. 1998, A&AS, 133, 403

Mewe, R. 1972, Sol. Phys., 22, 459

Miller, J. A., Larosa, T. N., & Moore, R. L. 1996, ApJ, 461, 445

Milligan, R. O., Kennedy, M. B., Mathioudakis, M., & Keenan, F. P. 2012, ApJ, 755, L16

Milligan, R. O., & McElroy, S. A. 2013, ApJ, 777, 12

Moore, R., McKenzie, D. L., Svestka, Z., et al. 1980, in Skylab Solar Workshop II, ed. P. A. Sturrock, 341–409

Nagai, F. 1980, Sol. Phys., 68, 351

Nagai, F., & Emslie, A. G. 1984, ApJ, 279, 896

Neupert, W. M. 1968, ApJ, 153, L59

Nishizuka, N., & Shibata, K. 2013, Physical Review Letters, 110, 051101

O'Dwyer, B., Del Zanna, G., Mason, H. E., Weber, M. A., & Tripathi, D. 2010, A&A, 521, A21

Oster, L., & Sofia, S. 1966, ApJ, 143, 944

Parker, E. N. 1957, J. Geophys. Res., 62, 509

Peres, G., Serio, S., Vaiana, G. S., & Rosner, R. 1982, ApJ, 252, 791

Pesnell, W. D., Thompson, B. J., & Chamberlin, P. C. 2012, Sol. Phys., 275, 3

Phillips, K. J. H., Bromage, G. E., & Doyle, J. G. 1992, ApJ, 385, 731

Pizzo, V. J., Hill, S. M., Balch, C. C., et al. 2005, Sol. Phys., 226, 283

Priest, E. R., & Forbes, T. G. 2002, A&A Rev., 10, 313

Qiu, J., Lee, J., Gary, D. E., & Wang, H. 2002, ApJ, 565, 1335

Qiu, J., Liu, W. J., Hill, N., & Kazachenko, M. 2010, ApJ, 725, 319

Qiu, J., Liu, W.-J., & Longcope, D. W. 2012, ApJ, 752, 124

Qiu, J., Sturrock, Z., Longcope, D. W., Klimchuk, J. A., & Liu, W.-J. 2013, ApJ, 774, 14

Raymond, J. C., Cox, D. P., & Smith, B. W. 1976, ApJ, 204, 290

Reeves, K. K., & Moats, S. J. 2010, ApJ, 712, 429

Reeves, K. K., & Warren, H. P. 2002, ApJ, 578, 590

Reeves, K. K., Warren, H. P., & Forbes, T. G. 2007, ApJ, 668, 1210

Reeves, K. K., Winter, H. D., & Larson, N. L. 2012, in Astronomical Society of the Pacific Conference Series, Vol. 455, 4th Hinode Science Meeting: Unsolved Problems and Recent Insights, ed. L. Bellot Rubio, F. Reale, & M. Carlsson, 199

Reznikova, V. E., Melnikov, V. F., Shibasaki, K., et al. 2009, ApJ, 697, 735

Ricchiazzi, P. J., & Canfield, R. C. 1983, ApJ, 272, 739

Scherrer, P. H., Schou, J., Bush, R. I., et al. 2012, Sol. Phys., 275, 207

Schmelz, J. T., Jenkins, B. S., & Kimble, J. A. 2013, Sol. Phys., 283, 325

Shibata, K., & Magara, T. 2011, Living Reviews in Solar Physics, 8, 6

Smith, D. M., Lin, R. P., Turin, P., et al. 2002, Sol. Phys., 210, 33

Somov, B. V., & Kosugi, T. 1997, ApJ, 485, 859

Somov, B. V., Sermulina, B. J., & Spektor, A. R. 1982, Sol. Phys., 81, 281

Somov, B. V., Spektor, A. R., & Syrovatskii, S. I. 1981, Sol. Phys., 73, 145

Spitzer, L. 1962, Physics of Fully Ionized Gases, ed. Spitzer, L.

Sterling, A. C., Shibata, K., & Mariska, J. T. 1993, ApJ, 407, 778

Stewart, B. 1861, Royal Society of London Philosophical Transactions Series I, 151, 423

Sturrock, P. A. 1966, Nature, 211, 695

Sweet, P. A. 1958, in IAU Symposium, Vol. 6, Electromagnetic Phenomena in Cosmical Physics, ed. B. Lehnert, 123

Tsuneta, S., & Naito, T. 1998, ApJ, 495, L67

Tucker, W. H., & Koren, M. 1971, ApJ, 168, 283

Veronig, A., Vršnak, B., Dennis, B. R., et al. 2002a, A&A, 392, 699

Veronig, A., Vršnak, B., Temmer, M., & Hanslmeier, A. 2002b, Sol. Phys., 208, 297

Vilhu, O., Muhli, P., Huovelin, J., et al. 1998, AJ, 115, 1610

Wang, H., Goode, P. R., Denker, C., et al. 2000, ApJ, 536, 971

Warren, H. P. 2006, ApJ, 637, 522

Warren, H. P., & Doschek, G. A. 2005, ApJ, 618, L157

Warren, H. P., Mariska, J. T., & Doschek, G. A. 2013, ApJ, 770, 116

Warren, H. P., & Warshall, A. D. 2001, ApJ, 560, L87

Warren, H. P., Winebarger, A. R., & Brooks, D. H. 2012, ApJ, 759, 141

White, S. M., Thomas, R. J., & Schwartz, R. A. 2005, Sol. Phys., 227, 231

Winebarger, A. R., & Warren, H. P. 2004, ApJ, 610, L129

Winter, H. D., Martens, P., & Reeves, K. K. 2011, ApJ, 735, 103

Wood, B. E., Wu, C.-C., Rouillard, A. P., Howard, R. A., & Socker, D. G. 2012, ApJ, 755, 43

Woods, T. N., Hock, R., Eparvier, F., et al. 2011, ApJ, 739, 59

Woods, T. N., Eparvier, F. G., Hock, R., et al. 2012, Sol. Phys., 275, 115

Wu, S. T., Kan, L. C., Nakagawa, Y., & Tandberg-Hanssen, E. 1981, Sol. Phys., 70, 137

Zeng, Z., Qiu, J., & Judge, P. G. 2014, ApJ, submitted

Zharkova, V. V., Arzner, K., Benz, A. O., et al. 2011, Space Sci. Rev., 159, 357